

---

## ELECTRICAL PRECISION TREATMENT OF MATERIALS

---

# Control of the Discharge Plasma Effective Volume at the Contact Electrospark Process in Liquid

S. V. Petrichenko

*Institute of Pulse Processes and Technologies, National Academy of Sciences of Ukraine,  
pr. Oktyabr'skii 43-a, Nikolaev, 54018 Ukraine*

*iipt@iipt.com.ua*

Received November 27, 2007

**Abstract**—New experimental results that allow executing stabilized critical discharges between metallic granules in a liquid by a combination of electrotechnical parameters of the discharge contour are obtained. The form of the channel and the law of its extension, taking into consideration the momentary electrical power, were determined. This has allowed offering dependences for the regulation of an effective volume of discharged plasma. The influence of different-diameter gas inclusions on the processes of formation and development of the discharge was estimated.

**DOI:** 10.3103/S1068375508030010

## INTRODUCTION

In recent years, pulse technologies for obtaining new submicron and nanostructure materials based on electrospark discharge application in inhomogeneous condensed media have been intensively studied. These technologies are most widely applied in modern electrotechnical systems with a reactor containing a layer of current-conducting grains in liquid (volume electrospark dispersion). In the course of the design of these systems, it is of prime importance to decrease the instability of their operation modes and to increase their efficiency. This is explained by the unique structure and properties of spark-erosion micro- and nanoparticles that make the specific power consumption and maintenance charges not so important. For the solution of the mentioned problems, there exists a complex of effective measures for parametric stabilization of the voltage or current, the control of the pulse frequency and the mean electric power in one pulse, etc. Further development of the method of volume electrospark dispersion (VESD) requires studying the interactive relation of the technological and electric parameters of the corresponding installations and is attributed to the necessity of the development of specialized physical models for the analysis of electrospark processes in the grain layer [1].

One of the most significant dynamic characteristics of the contact electrospark process is the discharge plasma volume (at determinacy of the structure and form of the discharge channel), since it is known that an increase in the melted metal volume leads to an increase of the VESD efficiency. In order to decrease the mean dimension of the obtained spark-erosion particles, it is necessary to determine the conditions under which the vaporous metal volume is maximal [2]. Thus, both the VESD efficiency and the treatment product

dispersion degree on the level of primary sparking are characterized by the mean effective volume of the plasma formation  $q_{EF}$ . In this case, by  $q_{EF}$  is meant the volume occupied by the plasma by the moment of the pulse power maximum achievement. At the same time,  $q_{EF}$  determines the surface area of the spark-discharge plasma and characterizes the radiation losses. The value of  $q_{EF}$  is determined by the dynamic parameter—the plasma channel expansion rate. The analysis and development of methods for control of the effective volume of the discharge plasma of a local spark-erosion channel are impossible without the application of means of high-speed on-bit photorecording in combination with synchronous oscillography of the discharge current and the voltage in the interelectrode space. Realization of these measurements and creation of adequate models of primary sparking in the layer is a complex scientific-applied problem. The determination of the form, the structure, the expansion law of the plasma channel interrelated with the process pulse power, and the  $q_{EF}$  dependence on the electrotechnical parameters of the discharge circuit will contribute to the development of new methods and means for the control of the modes of electropulse treatment of current-conducting media in grain form. The development of methods of  $q_{EF}$  control based on influences of nonelectric nature is a separate problem. For the moment, gas bubble influence on the spark channel formation in the contact spacing and, in the first place, on the spark-erosion process in the active stage remains a challenging open problem. The available data on these influences are contradictory and, for the most part, they are related to the bubble model of liquid breakdown [3].

Earlier, we developed and evaluated a physical model of primary sparking for the processes of VESD

of an aluminum grain layer in water. The principles of the development and embodiment and the parameters of the model, as well as the argumentation of the selection of the experiment conditions, are described in detail in paper [4]. The basic advantages of the model based on a three-electrode system are the following: the possibility to simulate the contact conditions between the grains, the specified load level on the contact units, the providing of spontaneous motion of the grains, the possibility of sparking surveying against highlighting and in the self-glow mode, the introduction of gas bubbles, etc.

A stabilized matched spark discharge for this model as applied to the solution of the set problems is the subject of the present research.

### EXPERIMENT CONDITIONS

The experiments were carried out at values of the charge voltages  $U_0$  from 50 to 350 V; in conversion for a real technological unit at treatment of a layer with low grain content (according to the technique of [5]), this corresponds to the voltage applied to the electrode plates being approximately from 300 V to 2.8 kV. The radii of the model electrode grains was 3 mm. The storage capacity was varied from 10 to 100  $\mu\text{F}$ . The discharge circuit inductance  $L_{Ts}$  was about 2  $\mu\text{H}$ . The discharge was realized with all the other conditions being equal in a degassed liquid with gas bubble introduction into the near-contact zone.

The experiment's diagnostic system allowed the following: (i) frame-by-frame photography with a frequency up to  $2 \times 10^6$  frames per second (the camera was an SFR); (ii) registration of the current pulses and the voltage by virtue of a coaxial shunt, an ohmic divider, and a two-beam memory oscilloscope.

Various techniques of gas bubble introduction into the interelectrode space are known: through a needle, through a hole in the electrode, and by pressure release. For the control and reproducibility of the experimental conditions with respect to the parameters of the bubbles—their location, dimension, form, and amount—there was applied the method proposed in [3] of bubble formation by virtue of a capillary, which was temporarily introduced into the near-contact zone, and by virtue of an injection syringe. The absence of other bubbles was controlled by observation.

### DISCHARGE STABILIZATION AND MATCHING

The possibility of the existence of unstable spark discharges between grains was described in paper [4]. The spread of the instability was shown in values of the amplitude and duration, in a sharp decrease of the discharge current, and in repeated space breakdown in the course of single commutation (Fig. 1a). For the moment, a more full classification of the discharge modes has been made and the diapasons of their realization conditions have been found (Fig. 1b). Thus, the

dependence  $U_0/C$  determines the boundary between the regions of existence of stable discharges (Fig. 1b, pos. 2, 3, and 4) and unstable ones (Fig. 1b, pos. 1). For the experimental conditions, the region of existence of stable discharges is numerically expressed by the relation

$$\frac{U_0 - 44}{0.56C} \geq 1. \quad (1)$$

The electromagnetic processes in the discharge circuit proceed so that, by the moment of time corresponding to the duration of the discharge current half-period for stable modes, the following situations are probable:

- a) Residual voltage is available in the IES; the current breaks at the zero level (Fig. 1b, pos. 2).
- b) The voltage in the IES reaches the zero level, and the current breaks at the zero level as well (Fig. 1b, pos. 3).
- c) The mode becomes of a pronounced oscillatory character (Fig. 1b, pos. 4), and the current breaks at the negative level (up to 1/6 the amplitude of the positive half-wave) with this being due to the finite duration of the thyristor turnoff.

The dependence of the ratio  $W/W_0$  (of the released energy to the stored one) on the discharge current has its maximum on the assumption of the equality of the integral equivalent resistance of the discharge channel  $R_{EKV}$  [5] and the wave resistance of the discharge circuit  $\rho_w$ . As one can see from Fig. 1d, for lower capacitances of the diapason, the  $W/W_0$  maximum is shifted towards lower values of  $U_0$ , and, at  $C = 10 \mu\text{F}$ , it is not pronounced. Since  $R_{EKV}$  monotonously decreases as the discharge voltage grows (Fig. 1c), this maximum is the optimum mode at the given  $L_{Ts}$  and  $C$ . Further increase of the discharge voltage leads to worse redistribution of energy between the load and the feeding line. Thus, the extreme situation (Fig. 1d) for stable discharge modes is determined by the wave resistance of the discharge circuit, and the analytic dependences of  $R_{EKV}$  for the grain layer obtained in work [5] may be applied for SCG matching with the load, thus providing maximal energy efficiency in the discharge circuits.

Further consideration of the discharge plasma dynamics was realized for stabilized and matched modes of contact spark discharges.

### FORM, UNIFORMITY DEGREE, AND DYNAMICS OF THE CHANNEL

As was shown earlier [6], at longer lasting discharge and at higher injected energy, at the specified length of the interelectrode space, the final channel form is closer to a sphere, even if the initial channel form was close to cylindrical. The more so, if the initial channel form had spherical symmetry, the final form would retain this symmetry.

As our experiments have shown, the sparking contact channel may be compound, exhibiting spatial discreteness. Starting with a certain moment of time  $t_1$ ,

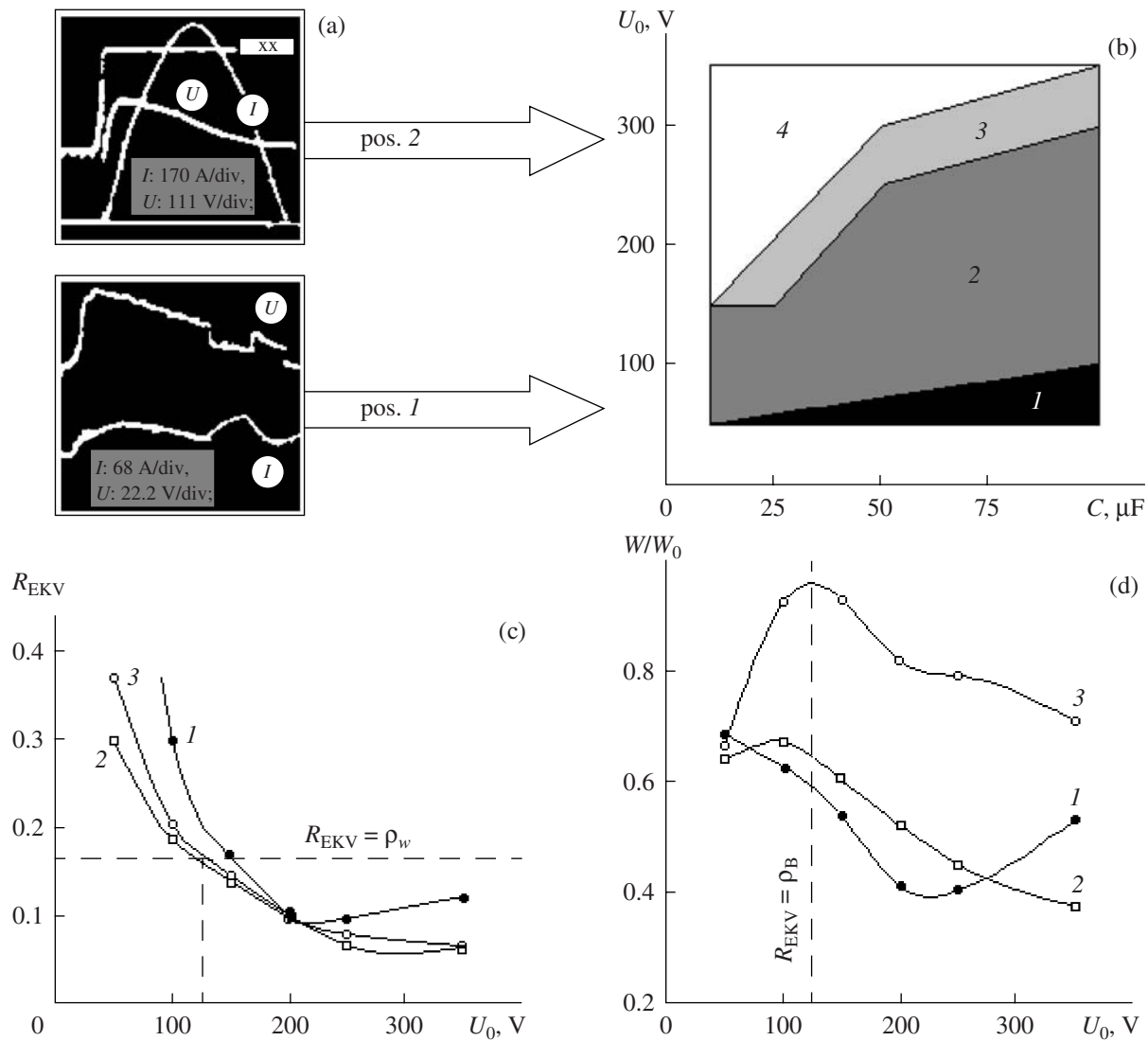


**Fig. 1.** Characteristic modes of electrospark discharges (a) and conditions of stabilization (b) and matching (c, d): 10 (1); 25 (2); 100 (3)  $\mu\text{F}$ .

already in the first microseconds after formation, due to intense expansion, the discharge channel in degassed liquid assumes the form of ellipse (Fig. 2). For the experiment conditions, the registered value of  $t_1$  did not exceed  $8 \mu\text{s}$  at a total duration of the stable discharge current stage of  $\tau = \pi \sqrt{L_{\text{TS}} C}$  (about  $50 \mu\text{s}$ ). Emphasis is put on the current stage duration, since, in some cases, exothermal reactions of activated aluminum and the environment were observed.

Judging by the discharge glow, in the process of expansion, plasma fills the channel uniformly (up to the power surge). A similar interpretation of discharge photograms in the survey mode "slow motion camera" is proposed in such an expert work as [6], where analogous means of photorecording were applied. At the same time, the authors of [6], on the basis of continuous

strip photoscanning results, have shown that plasma separation from the channel walls takes place in the discharge end only, thus confirming the given interpretation.

Up to the power maximum, the channel expands uniformly (Fig. 3a); the mean rate of its expansion in this interval is  $v = 2(r_{\text{EF}} - r_0)/\tau$ . Then, the expansion law may be presented by the simple linear dependence

$$r = r_0 + vt, \quad (2)$$

where  $r_0$  is the channel radius at the initial moment of time, m; and  $v$  is from 50 to 70 m/s for the matched discharge modes.

In the drop-down section of the power  $N$ ,  $v$  sharply decreases: by a factor of two for the first  $8 \mu\text{s}$  from the moment of the maximum. At the expansion front—near the surface of the plasma contact with the liquid—the

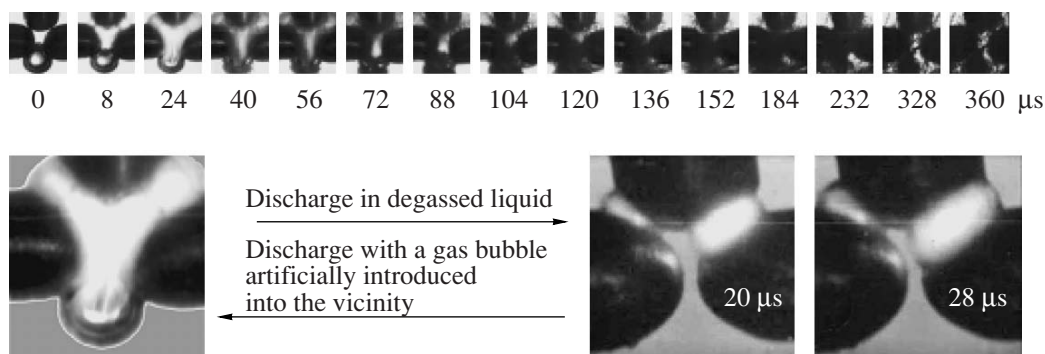


**Fig. 2.** Dynamics of discharge plasma and the gas bubble influence on it.

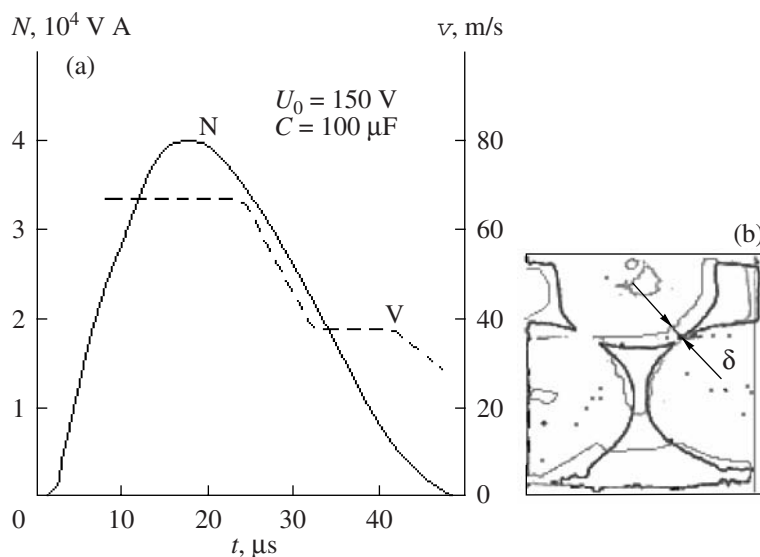


**Fig. 3.** Interrelation of the electric and kinematic characteristics of the discharge (a) and the displacement of electrode grains in the course of the process (b).

substance starts cooling down, since  $N$  is already insufficient for maintenance of the plasma homogeneity at the periphery. This leads to darkening of the plasma region boundary. Such an explanation is applicable for the interpretation of photograms of end-to-end channels of current flow.

An important dynamic parameter applicable for the introduction of a new control channel is the effective volume  $q_{EF}$  of the plasma formation. It is calculated at the moment of time corresponding to the amplitude of the energy injection rate. Then, for estimation of the effective volume, the following approximate expression can be applied:

$$q_{EF} \approx \frac{4}{3}\pi \left( r_0 + v \frac{1}{2} \pi \sqrt{L_{TS} C} \right)^3 - V_{GR}, \quad (3)$$

where  $V_{GR}$  is a certain correction factor having volume dimension and taking into account the presence of moving grain surfaces inside the plasma cloud

(Fig. 3b). The  $V_{GR}$  value is affected, first of all, by the layer height, i.e., the level of the contact load, and the grain dimensions.

As the level of the contact load decreases, in all probability, the grain motion  $\delta$  increases and the elliptic discharge channel form tends to spherical. The displacement of the mobile electrode–grain ( $\delta$  in Fig. 3b) for the time interval of 100  $\mu$ s from the process beginning was from 0.7 to 0.9 mm, its weight being 7.5 g. The mobile electrode weight reflected the load of the real grain layer. On the basis of this result, the dynamic force created by the microplasma channel at points of its binding to the surface of the electrode–grains is determined.

Important results were obtained in the experiments when a gas bubble of 5 mm diameter was introduced under the intermediate electrode at a distance of 5 mm from it (Fig. 2). Within 16  $\mu$ s after the formation of the plasma channels, their boundaries achieved the bubble, and, in 8  $\mu$ s more, the bubble was filled with the dis-



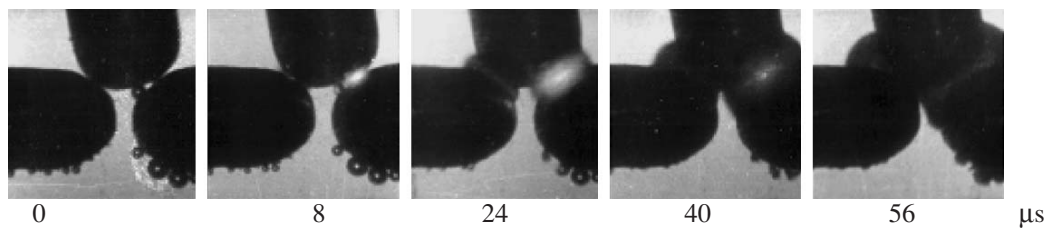


Fig. 4. Gas bubble influence on the process of spark channel formation.

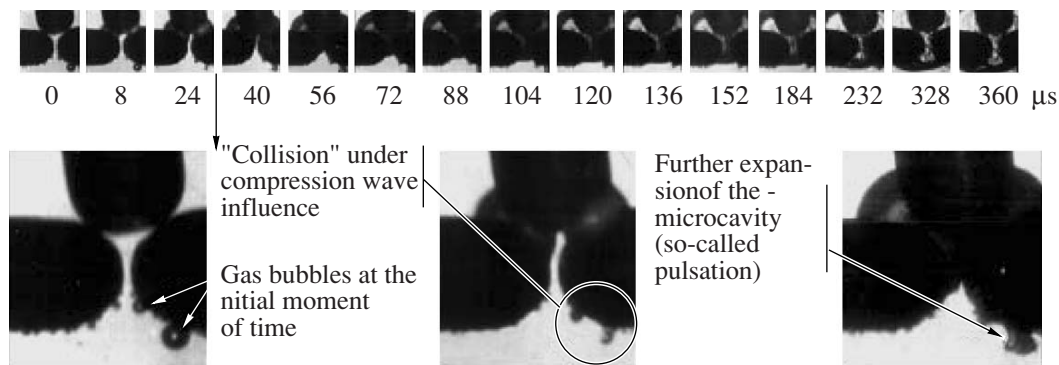


Fig. 5. Gas and hydrodynamic processes in the near-discharge zone at the presence of gas inclusions in it.

charge plasma (Fig. 2). The total volume of the plasma formation was increased by 30%. During the next 8  $\mu$ s, the plasma glow ceased, while, under regular conditions (without the bubble), it proceeded from 8 to 16  $\mu$ s. A forced increase in the volume of the plasma leads to its faster cooling. The introduction of the gas phase into the reactor as a factor of the energy conversion process control is of high priority, since it changes the behavior of the electrothermal, gas, and hydrodynamic processes in the discharge zone and weakly influences the formation of spark channels in the layer, as will be shown below.

#### INFLUENCE OF GAS INCLUSIONS ON THE SPARK CHANNEL FORMATION

The initial electric field intensity in the microspace between contacting grains at a known charge voltage of the storage is determined mainly by the state of their surfaces: by the availability of microasperities, craters, oxide film defects, and other factors. Its estimation by calculation and experiment methods and, much less, control are practically impossible. In the course of the selection of the diameter  $d_p$  of the air bubbles introduced into the vicinity of the contact spacing, for the determination of their influence on the formation of the discharge channels, we proceeded from their correspondence to the diameter of visible bubbles that are naturally formed in the environment due to a series of discharges. At the same time, the probability of the complete coverage of the contact spacing by the arti-

cial bubble was eliminated. Values of  $d_p$  from 0.5 to 1.5 mm met the requirements. Air bubbles were used.

The experiment has shown that the introduction of a gas bubble with a diameter of 0.5 mm at a distance of 0.5 mm from the contact axis (Fig. 4), so that it is in contact with the surfaces of neighboring grains, does not appreciably influence the process of plasma channel formation.

Introduction of such bubbles at a distance of 5 and 6.5 mm (in successive order in one line) from the zone of the spark channel formation (Fig. 5) allowed estimation, by the moment of time for which deformation (collapse) of the first and second bubbles occurs, of the mean rate of propagation of the compression front  $\dot{r}_{VSZh}$  in the spaces to these points. It was approximately 310 and 270 m/s, respectively. If we take into account the error due to the finite duration of the exposure and the time interval between the frames, the second value is more reliable. The distance that the compression wave covers in the direction radial to the contact axis up to the moment of time corresponding to the current amplitude may be estimated from the following expression:

$$r_{VSZh} = r_0 + \frac{1}{2} \pi \dot{r}_{VSZh} \sqrt{L_{Ts} C}. \quad (4)$$

The values are obtained for  $U_0 = 125$  V,  $C = 100$   $\mu$ F with the mode being optimum for the energy criterion  $W/W_0$ .

## CONCLUSIONS

Thus, for stable (Fig. 2b, pos. 2–4) matched (Fig. 2c,  $R_E = \rho_B$ ) modes of contact spark discharge, the volume  $q_{EF}$  is determined by the set of parameters  $U_0$ ,  $C$ ,  $L_{Ts}$ ,  $r_0$ , and  $v$  and by the factor  $V_{GR}$ . The control of the  $q_{EF}$  value and, therefore, the creation of new channels of control of the technological processes must be carried out according to empirical expression (3) and may be realized by the following:

—Combination of the electrotechnical parameters of the discharge circuit  $U_0$ ,  $C$ , and  $L_{Ts}$  in the range of variation of the dynamic parameter  $v$  from 50 to 70 m/s for matched modes of spark discharge.

—Variation of the factor  $V_{GR}$  due to variation of the grain diameter  $O_0$  and the level of the contact load that influences the grain motion. The functional dependence  $V_{GR} = f[d_0, 2\delta/(\pi\sqrt{L_{Ts}C})]$  is determined by simple geometrical ratios.

—Introduction of gas bubbles of diameters comparable to  $d_0$  (for decreasing probability of complete coverage of the contact spacing by the bubble); this allows control of  $q_{EF}$  and is a new independent channel of the technological process control. If gas inclusions do not cover the whole contact spacing, they weakly influence the process of sparking formation; however, their introduction into IES allows an increase by 30% of  $q_{EF}$  and the substance cooling rate.

—Variation of the effective distance  $r_{VSZh}$  covered by the compression wave in the direction radial to the contact axis. Control of  $r_{VSZh}$  is realized by the tech-

niques described in part 1–2; the correction factor  $V_{GR}$  must be introduced into expression (4). The ratio  $r_{VSZh}/d_0$  characterizes the degree of interaction of neighboring contact units. This interaction can be considered a favorable factor contributing to sparking migration and substance removal from discharge zones.

## REFERENCES

1. Shidlovskii, A.K. and Lipkivskii, K.O., Rozvitok doslidgen' po peretvorenniyu ta stabilizatsii parametriv elektromagnitnoi energii v Institute elektrodinamiki NAN Ukraini, *Tekh. Elektrodin.*, 2007, no. 3, pp. 11–26.
2. Shcherba, A.A., Podoltsev, A.D., and Kucherjavaja, I.N., Spark Erosion of Conducting Granules in a Liquid: Analysis of Electromagnetic, Thermal, and Hydrodynamic Processes, *Tekh. Elektrodin.*, 2004, no. 6, pp. 4–18.
3. Skorykh, V.V., Influence of Gas Bubbles on Discharge Ignition in Water, *Zh. Tekh. Fiz.*, 1986, vol. 56, issue 8, pp. 1569–1572.
4. Shcherba, A.A. and Petrichenko, S.V., Physical Simulation and Analysis of Dynamics of Spark–Plasma Processes at Electroerosion Dispersion of Current–Conducting Grains in Liquid, *Tekh. Elektrodin.*, 2004, no. 3, pp. 27–32.
5. Shcherba, A.A., Podoltsev, A.D., and Zakharchenko, S.N., Control of Dynamic Parameters of Technological Systems of Volume Electrosark Treatment of Heterogeneous Current–Conducting Media, in *Pratsi IED NANU*. Kiev: *Elektrotehnika*, 2001, pp. 3–17.
6. Naugol'nykh, K.A. and Roi, N.A., *Elektricheskie razryady v vode* (Electric Discharges in Water), Moscow, 1971.

---

## ELECTRICAL SURFACE TREATMENT METHODS

---

# Hardening and Softening Processes in Iron Electrodeposits at Friction Wear

T. V. Bortsoi

*Institute of Applied Physics, Academy of Sciences of Moldova, ul. Academiei 5, Chisinau, MD-2028 Republic of Moldova*  
*e-mail: bortzoi\_tudor@yahoo.com*

Received October 22, 2007

**Abstract**—A method of revealing and estimation of hardening and softening processes in iron electrodeposits at wear process by their sliding friction is proposed. The contribution of hardening and softening processes to wear resistance values can be estimated by the law of variation in values of relative deviations of neighboring units of a statistical ensemble of wear resistance values. It is established that, at the wear process of alloys of iron electrodeposits, the contribution of hardening and softening processes to the wear resistance depends on the alloy composition and test load. At the wear process of composites based on iron with particles of aluminum oxide and with a concentration close to the optimum composition, the contribution of hardening and softening processes is characterized by cyclic recurrence and depends on the load at the interface.

**DOI:** 10.3103/S1068375508030022

One of the most important functional properties of iron electrodeposits (as well as iron alloys and composites) is their wear resistance. Therefore, for selection of optimum compositions of iron deposits that can function to the best advantage in specified operating conditions, it is necessary to study the characteristic peculiarities of the mechanism of their wear.

As a result of wear, surface layers of a material undergo various changes that determine its wear resistance. Therefore, for investigation of metallic material wear, indirect methods are applied most often: estimation of the microhardness, microstructure, and fine structure in the near-surface layers; the surface roughness; and other physicomachanical characteristics [1–4, etc.].

Let us note that the processes taking place in the near-surface layers, according to their influence on the wear resistance of materials, are divided into two groups: hardening processes that increase wear resistance and softening ones that decrease it [3, 4, etc.]. However, hardening and softening processes are diverse in their nature; in real conditions, they can proceed simultaneously [3].

Hardening and softening processes proceeding at friction in the near-surface layers in iron electrodeposits have been studied in works [1, 2, etc.]. It has been found in [1] that, at friction of iron electrodeposits in the near-surface layers, the proceeding processes cause variations of the microhardness, roughness, and fine structure. At the same time, the coatings that acquired significant strain hardening in the test process were characterized by higher wear.

The study of the fine structure of iron composite matrixes with high-strength disperse phase particles,

such as aluminum oxide and boron carbide, tested under various conditions has shown that, in the process of friction, the dimensions of the matrix mosaic blocks practically did not change [2]. Thus, despite numerous studies in the given field, no direct relationship between the wear resistance of iron deposits and the processes of hardening and softening in near-surface layers has been found. Therefore, the study of the iron deposit wear mechanism is a problem of high priority and is of great theoretical and applied importance.

Research aimed at more intensive study of the wear mechanism will allow reasonable selection of the optimum composition of iron deposits and the optimum technological parameters of the processes of hardening or recovery of wearing surfaces of machine pieces.

It has been found in some works on tribology [3–5, etc.] that, in the absence of structural or other variations in friction near-surface layers, their wear resistance is proportional to the load. For example, at the steady-state behavior of abrasive wear of materials, no property variation is observed in the near-surface layers; the wear is characterized by a uniform linear dependence on the load [5, etc.].

It is obvious that manifestation of nonuniformity of variation in the metallic material wear resistance may show which processes—hardening or softening—prevail in the friction near-surface layers.

Nonuniformity of the wear resistance variation can be revealed by a material wear test with specified friction conditions that are determined by a series of standard loads with an identical range of values, steady-state behavior, and measured wear. In this case, the degree and direction of the nonuniform variation of the material wear resistance may be found and estimated

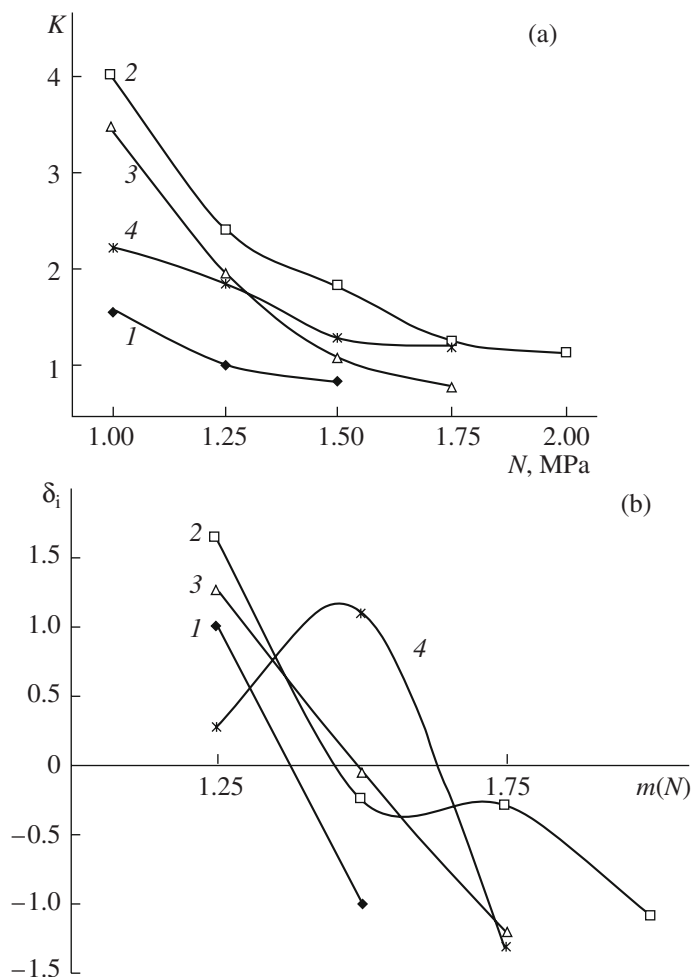


**Fig. 1.** Dependence of the wear resistance  $K$  on the load  $N$  (a) and the relative deviations  $\delta_j$  (b) on the load range  $m$  for steel 45 (1), Fe–Co alloy (2), Fe–Ni alloy (3), and Fe (4).

on the basis of an analysis of the values of the relative deviations of neighboring units  $\delta_j$  of the statistical ensemble of wear process experimental results [6, 7].

For statistical series of values of the ensemble,  $X$   $\delta_j$  will be determined from the expression

$$\delta_j = \frac{(h_j - \bar{h})}{\epsilon_x}, \quad (1)$$

where  $h_j = x_i - x_{i+1}$  is the difference between the deviations of the statistical unit  $x_i$  from the neighboring (adjoining)  $x_{i+1}$ ,  $\bar{h} = \sum_{j=1}^m [x_i - x_{i+1}] / m$  is the mean value for  $m = n - 1$  deviations of neighboring units in the ensemble  $X$ , and  $\epsilon_x = \sqrt{\sum_{j=1}^m [x_i - x_{i+1}]^2 / m}$  is the mean square deviation of neighboring (adjoining) units of the ensemble  $X$  composed of  $m = n - 1$  neighboring (adjoining) deviations.

Let us note that the relative deviations of neighboring units  $\delta_j$  are multipurpose, since they may be used for the comparison of the level of variation in values of the units of different ensembles of one parameter (for example, wear resistance) or ensembles of different parameters (microhardness, roughness, fine structure parameter values, etc.).

## EXPERIMENTAL

The object of study was iron based electrodeposits formed from various solutions under optimum electrolysis conditions tested at sliding friction with a series of standard loads. The iron deposits and their composites were formed according to the recommendations presented in [1]; those of iron–cobalt and iron–nickel, in [2, 8]. The disperse phase in the iron composites was particles of aluminum oxide with grain fineness M7, M14, and M20. Hardened steel 45 was used as the reference material.

The iron electrodeposits were subjected to sliding friction testing by the method of low-cycle fatigue wear, which is characterized by physical determination of the wear process and the intensity of the abrasive wear, satisfactory reproducibility, and the simple technique of its realization [9, 10].

The results were treated by the methods accepted in tribology and with application of relative deviations of neighboring units for ensembles of values.

## RESULTS AND DISCUSSION

The studies have shown that the mode of the wear resistance variation  $K$  due to the standard unit of load  $N$  for selected iron electrodeposits possesses certain peculiarities and differences (see Fig. 1a and Fig. 4a).

Electrodeposited alloys are characterized by the following: as the standard unit of pressure  $N$  increases from 1 to 2 MPa, their wear resistance (see Fig. 1a, curves 2 (iron–cobalt) and 3 (iron–nickel)) decreases faster than in pure iron (curve 4) and hardened steel 45 (curve 1). The lowest values of the wear resistance factor  $K$  are found for steel 45 (see Fig. 1a, curve 1), which was tested up to a standard pressure of 1.5 MPa, since, at higher loads, the mode of counterface wear varies.

For iron deposits (curve 4), the mode of the counterface wear varies as well at loads above  $N = 1.75$  MPa. The wear of iron deposits under low load conditions (up to  $N = 1.25$  MPa) is characterized by a lower value of the wear resistance factor  $K$  than for alloys of iron–cobalt (curve 2) and iron–nickel (curve 3). As the load increases ( $N = 1.25$ – $1.75$  MPa), the wear resistance  $K$  of the iron deposits becomes higher than for the iron–nickel alloy and achieves the values obtained for the iron–cobalt alloy.

The dependence of the relative deviations of neighboring units  $\delta_j$  of the wear resistance  $K$  for materials of steel 45 and iron–nickel alloy shows that the direction



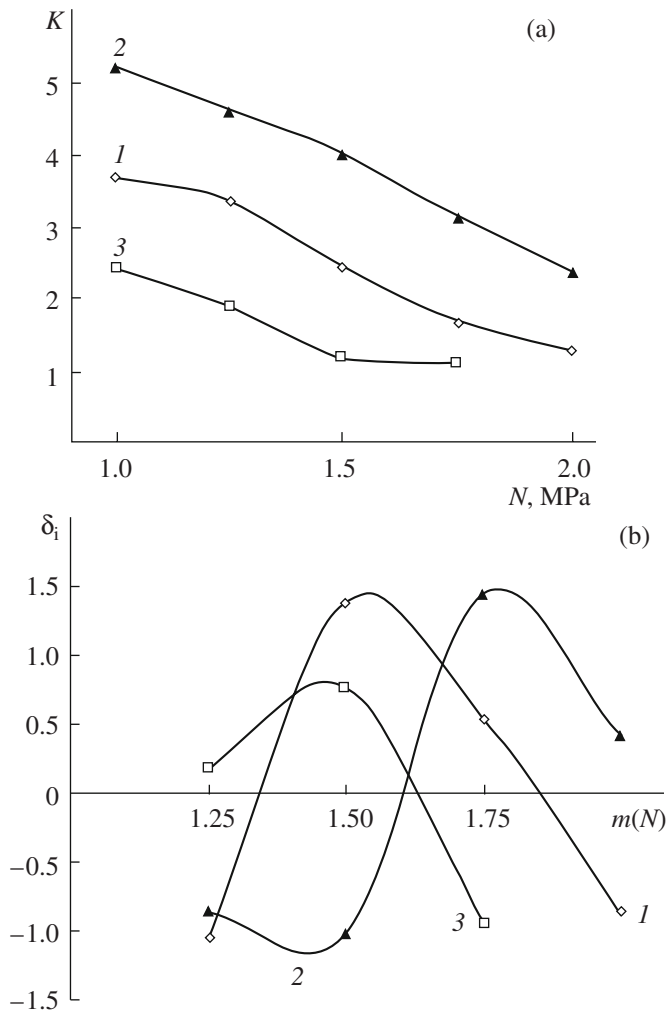


**Fig. 2.** Dependence of the wear resistance  $K$  on the load  $N$  (a) and the relative deviations  $\delta_j$  (b) on the load range  $m$  for iron based ECM at the following concentrations of aluminum oxide particles of grain fineness M7 (in wt %): 3.46 (1), 17.9 (2), and 22.1 (3).

and mode of the variation  $\delta_j$  are similar: from the highest values to the lowest ones (see Fig. 1b; curves 1 and 3, respectively).

It is obvious that, according to the proposed method, as the test loads increase, the hardening processes prevail in the surface layers of the given materials and their contribution to the wear resistance values increases.

In the course of friction of iron deposits (see Fig. 1b, curve 4) in the range of low loads (up to  $N = 1.5$  MPa), the values of  $\delta_j$  increase. In the given load range, softening processes prevail in the surface layers. In the range of higher loads, the values of  $\delta_j$  decrease; this counts in favor of the predominance of hardening processes. At the point of change of the direction of variation of the  $\delta_j$  values on curve 4, the contributions of the processes of hardening and softening to the wear resistance values become similar.

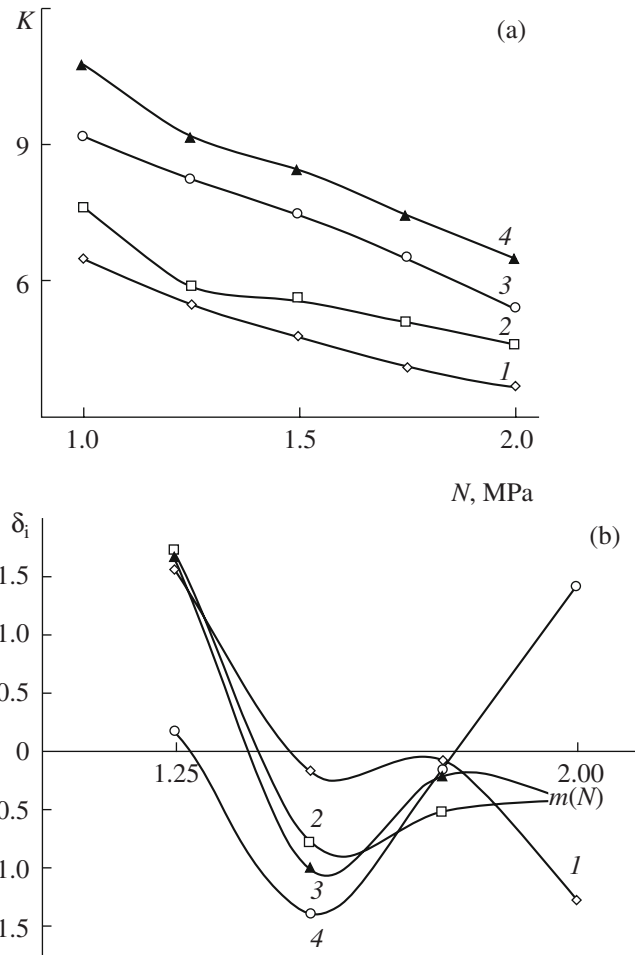


**Fig. 3.** Dependence of the wear resistance  $K$  on the load  $N$  (a) and the relative deviations  $\delta_j$  (b) on the load range  $m$  for iron based ECM at the following concentrations of aluminum oxide particles of grain fineness M14 (in wt %): 1.8 (1), 17.9 (2), 14.2 (3), and 19.5 (4).

For iron–cobalt deposits (see Fig. 1b, curve 2), the contribution of hardening processes at friction prevails in the whole load range. However, in the load range  $N = 1.5$ – $1.75$ , their values become similar to those of softening processes.

The analysis of the results of tests of composite deposits has shown that their wear resistance depends on the grain fineness ( $M$ ) and concentration (%) of the disperse phase as well as on the range  $m$  of the test loads  $N$  (see Figs. 2a–4a).

The high-concentration composites with particles of the disperse phase (DP) of 22.1 wt % and grain fineness M7 (see Fig. 2a, curve 3) possessed the wear resistance  $K$  on the order of iron deposits (Fig. 1a, curve 4). Low-concentration composites with 3.46% M7 particles are characterized by higher values of the wear resistance  $K$  (see Fig. 2a, curve 1) than the high-concentration ones (curve 3). The highest wear resistance is found for com-

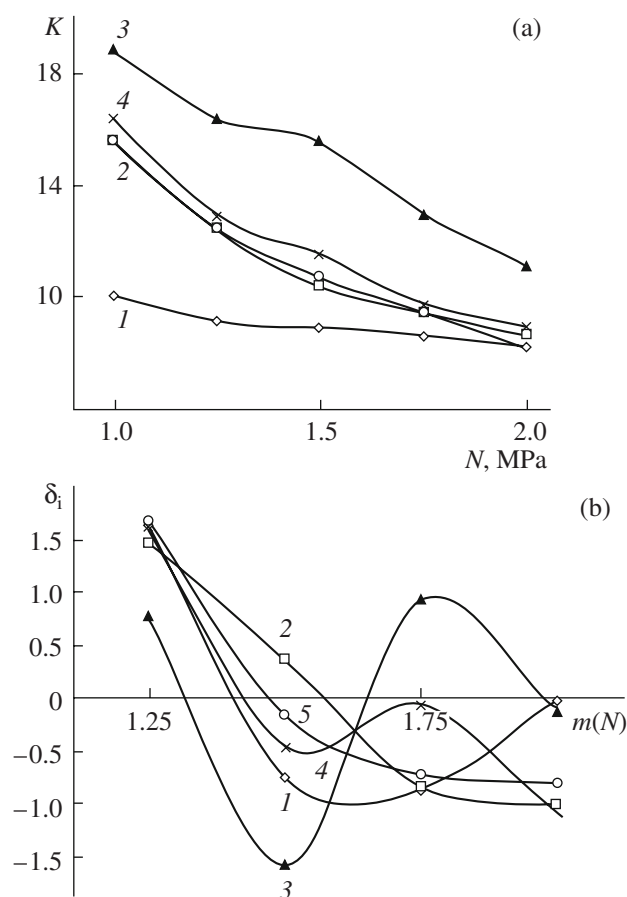


**Fig. 4.** Dependence of the wear resistance  $K$  on the load  $N$  (a) and the relative deviations  $\delta_i$  (b) on the load range  $m$  for iron based ECM at the following concentrations of aluminum oxide particles of grain fineness M20 (in wt %): 7.0 (1), 9.6 (2), 14.5 (3), 18.2 (4), and 20.3 (5).

posites with a concentration of DP particles of 17.9% (curve 2).

The dependence of the relative deviations of neighboring units  $\delta_i$  on the range  $m$  of the test loads  $N$  for composites with M7 particles shows that, for low-concentration (see Fig. 2b, curve 1) and high-concentration deposits (curve 3) in the load range of  $N = 1\text{--}1.5$  Mpa, softening processes prevail in the near-surface layers. At further increase of the test loads, hardening processes prevail. For the composites with the highest values of the wear resistance (see Fig. 2a, curve 2), a cyclic recurrence of the predominance of hardening and softening processes in the near-surface layers is found.

For composites with particles of grain fineness M7, the highest wear resistance is revealed at the concentration of 14.2% (see Fig. 3a, curve 3), and the lowest, at 1.8% (curve 1).

The mode of variation of the relative deviations  $\delta_i$  of the wear resistance for the test load range  $m$  for the composites with M14 particles is nonunique (see Fig. 3b). For the studied composites with M14 par-

ticles, the predominance of hardening processes in the load range of 1–1.5 MPa at friction is observed. Further increasing of the test load (1.5–2.0 MPa) of the composites with 19.5% particles leads to the predominance of softening processes in the surface layers (see Fig. 3b, curve 4). At friction of the composites with the highest wear resistance, the surface layers are characterized by a cyclic predominance of the processes of hardening and softening (see Fig. 3b, curves 1 and 3).

For the tested materials, the highest wear resistance is found for the composites with particles of the M20 grain fineness (see Fig. 4a). In addition, for the composites with a concentration of 7.0%, the most stable values of the wear resistance depending on the load are revealed (see Fig. 4a, curve 1). The composite material with a concentration of 14.5% disperse phase particles of grain fineness M20 is characterized by the highest wear resistance (see Fig. 4a, curve 3).

The study of the dependence of the relative deviations of neighboring units  $\delta_i$  of the range  $m$  of the test loads  $N$  for composites with M20 particles shows that the composites with 7% disperse phase are characterized by surface layers wherein, at low loads, hardening processes prevail; at higher loads, softening processes prevail (see Fig. 4b, curve 1). Composites with higher concentrations are mainly characterized by surface layers in which hardening processes prevail at friction in the whole load range (see Fig. 4b, curves 2 and 5) or phenomena of cyclic recurrence of the processes of hardening and softening take place (see Fig. 4b, curves 3 and 4).

Let us note that, for composites with M7, M14, and M20 disperse particles with concentrations close to the optimum ones [8], the analogous mode of behavior of hardening and softening processes is shown (see Figs. 2b–4b); that is, in the tested load range, at friction, these materials are characterized by cyclic recurrence of the processes of hardening and softening of the surface layers.

According to the results of the study, the conclusion can be reached that, by applying the method of material wear testing with uniform series of loads and the method of estimation of the relative deviations of neighboring units  $\delta_i$  of the material wear resistance, one can estimate the level and direction of the predominance of the processes of hardening or softening in the surface layers. In this case, there is no need to apply indirect methods of study of the physicomechanical properties of electrodeposits.

## CONCLUSIONS

1. It is experimentally found that, with specified friction conditions that are determined by a series of standard loads with an identical range of values, steady-state behavior, and a measure of wear, it is possible to find the nonuniformity of variation in the wear resistance of metallic materials.

2. It is revealed that the level and direction of the nonuniform variation of the metallic material wear resistance can be found and estimated on the basis of the analysis of the values of the relative deviations of neighboring units  $\delta_j$  of a statistical ensemble of experimental results of the wear. The contribution of hardening and softening processes to the wear resistance value can be estimated by the mechanism of variation of the values of the relative deviations of neighboring units of the statistical ensemble of wear resistance values.

3. It is found that, in the course of the wear of alloys of iron electrodeposits, the contribution of hardening and softening processes to the wear resistance depends on the alloy composition and the test load. In the course of the wear of composites based on iron with aluminum oxide particles with concentrations close to the optimum composition, the contribution of hardening and softening processes is characterized by cyclic recurrence and depends on the conjugation load.

#### REFERENCES

1. Gologan, V.F., Azhder, V.V., and Zhavguryanu, V.N., *Povyshenie dolgovechnosti detalei mashin iznosostoikimi pokrytiyami* (Increase of Lifetime of Machine Pieces by Application of Wear-Resistant Coatings), Chisinau: Shtiintsa, 1979.
2. Gur'yanov, G.V., *Elektroosazhdenie iznosostoikikh kompozitsii* (Electrodeposition of Wear-Resistant Composites), Chisinau: Shtiintsa, 1985.
3. Tenenbaum, M.M., *Iznosostoikost' konstruktivnykh materialov i detalei mashin pri abrazivnom iznashivani* (Wear Resistance of Construction Materials and Machine Pieces at Abrasive Wear), Moscow: Mashinostroenie, 1966.
4. Volkov, Yu.V., Volkova, Z.A., and Kaigorodtsev, L.M., *Dolgovechnost' mashin, rabotayushchikh v abrazivnoi srede* (Lifetime of Machines Operating in Abrasive Medium), Moscow: Mashinostroenie, 1964.
5. Grigorkin, V.I., Austenitic Manganese Steel and Rail Problem, *Metallovedenie, Termootbrabotka i Fizicheskie Svoistva Metallov i Splavov*, Lipetsk: MISIS, 1970, part 1, issue 7, pp. 159–169.
6. Bortsoi, T.V., Statistical Methods of Estimation of Relation between Electrochemical System Parameters with Distributed Values on the Electrode, *Elektron. Obrab. Mater.*, 2006, no. 4, pp. 24–36.
7. Bortsoi, T.V., Possibilities of Development of Statistical Methods of Estimation of Distributed Parameters of Electrochemical Deposits at Macrolevel, *Elektron. Obrab. Mater.*, 2007, no. 5, pp. 67–74.
8. Andreeva, L.N., Electrodeposition of Iron-Cobalt Alloys, in *Vosstanovlenie i uprochnenie detalei mashin iznosostoikimi pokrytiyami* (Recovery and Hardening of Machine Pieces by Wear-Resistant Coatings), Chisinau: Shtiintsa, 1995, pp. 9–16.
9. Borțoi, T., MD Inventor's Certificate no. 3087, *BOPI*, 2006, no. 6.
10. Bortsoi, T.V., Wear Resistance and Optimum Composition of Electrodeposited Composites, *Elektron. Obrab. Mater.*, 2005, no. 4, pp. 19–23.

## ELECTRICAL SURFACE TREATMENT METHODS

# Peculiarities of Electrode Processes on a Surface of Steel with Ion–Plasma Coatings of Titanium Nitride

A. I. Kostrzhitskii, T. V. Cheban, and O. M. Beregovaya

Odessa National Academy of Food Technologies, ul. Kanatnaya 112, Odessa, 65039 Ukraine

e-mail: kapitaskay@rambler.ru

Received October 27, 2007; in final form, February 26, 2008

**Abstract**—The influence of an aggressive environment on the behavior of titanium–nitride coated steel has been researched. The kinetics of the electrode potentials have been studied. The electrochemical corrosion parameters for different aggressive environments have been determined, and titanium nitride coatings are recommended for corrosion protection of steels.

**DOI:** 10.3103/S1068375508030034

## INTRODUCTION

In the last 25–30 years, ion–plasma coatings of titanium nitride and its analogs have been widely used in order to increase the wear resistance of machine pieces as well as the operating capability and lifetime of metal-cutting tools [1–4].

In the eighties–nineties of the XX century, there appeared the first works concerned with studying the possibilities to apply titanium nitride coatings for protection of low-carbon steels from corrosion [5–7]. It was mentioned that ion–plasma coatings of TiN, in their corrosion–electrochemical parameters, are cathodic in many aggressive environments. This, in turn, determines the general mechanism in the expected mode of the corrosion–electrochemical behavior of the coatings; that is, corrosion damage to steel is localized in the coating pores; the coating itself acts as a weakly polarized cathode [8–10]; and the damage mechanism is determined by the pore content of the coatings [11, 12], by the pore dimensions [13–15], and by the ratio of the pore diameter to the coating thickness [10, 15].

Despite certain progress in deposition of cathodic coatings, the problem of the interrelation of coating deposition modes and their functional characteristics (corrosion–electrochemical and protective ones) remains in abeyance.

## EXPERIMENTAL

The aim of the present paper is to study the influence of parameters of deposition of TiN coatings on their protective properties and corrosion–electrochemical characteristics in some neutral and acid aqueous solutions (running water, 3% NaCl solution, and aqueous solutions of H<sub>2</sub>SO<sub>4</sub> and HNO<sub>3</sub> of various dilution ratings). The substrate materials are the steels 08kp and

U8A with their corrosion–electrochemical characteristics being sufficiently close; therefore, the mode of the corrosion damage will be determined by the coating material only [8, 10, 13, 16].

Deposition of TiN coatings was realized by virtue of the installation "Bulat–3T." The initial material for electric-arc evaporators was the alloy BT1–0. The controlled parameters were the vacuum chamber nitrogen pressure  $P$ , the accelerating voltage on the substrate  $U$ , and the evaporator arc current  $I$ . The variation ranges for each parameter are presented in Table 1. In the course of observation of the resulting treatment, the method of experiment design and statistical data processing described in [17] was applied. Justification of this approach as applied to the study of protective properties of condensed films and coatings is given in papers [10, 14–16].

**Table 1.** Factor levels and variation ranges

Nomination and designation of factors	Factor code	Variation levels		Variation range, 2 $\sigma$
		+1	–1	
Accelerating voltage on the substrate $U_p$ , V	X <sub>1</sub>	220	50	170
Nitrogen pressure in the chamber $P$ , Pa	X <sub>2</sub>	0.665	0.0665	0.5985
Welding gun arc current $I$ , A	X <sub>3</sub>	120	80	40



**Table 2.** Results of studies of the deposition mode influence on electrode potentials of steel samples with titanium nitride coatings

Experiment number	$X_1$	$X_2$	$X_3$	Values of the electrode potentials (mV) in $t$					
				0	2 min	10 min	2 h	6 h	24 h
1	+	+	+	+610	+610	+595	-250	-315	-345
2	+	+	-	+525	+520	+375	-275	-340	-370
3	+	-	+	-180	-220	-250	-280	-350	-375
4	+	-	-	-205	-235	-265	-290	-340	-390
5	-	+	+	+560	+550	+540	-360	-410	-420
6	-	+	-	+580	+560	+540	-325	-370	-365
7	-	-	+	+535	+525	+480	-345	-365	-365
8	-	-	-	+570	+570	+535	-280	-370	-400

The corrosion–electrochemical behavior of TiN coatings was estimated according to results of the potentiodynamic studies. The potentiodynamic curves were studied by virtue of the potentiostat PI-50-1. The data reporting was carried out within 10–12 minutes after the immersion of the samples into the studied solution at the potential imposition rate of 12 mV/min. The samples for the studies were obtained at specified parameters:  $I = 100$  A,  $U = 220$  V, and  $T = 770$ – $820$  K. The varied parameters were the vacuum chamber pressure  $P$  and the coating thickness  $h$ . For the calculation of the parameters of the electrochemical corrosion process, the linear polarization method and the Stern–Geary equation were applied [18]. The technique of such studies as applied to condensed systems was described for the first time in paper [16] and was further developed in papers [10, 15, 19, 20].

## RESULTS AND DISCUSSION

The electrode potentials of steel samples with TiN coatings are time variant. The strongest influence on the mode of time variation of the electrode potentials of the steel samples with TiN coatings is rendered by the coating thickness. The variation of the deposition parameters (the nitrogen chamber pressure  $P$ , the welding gun arc current  $I$ , the condensation temperature  $T_K$ , and the accelerating voltage on the substrate  $U_P$  in the range of their optimum values affects behavior of the dependence  $\phi = f(\tau)$  significantly weaker. The parameters  $T_K$ ,  $I$ , and  $U$  render a certain influence on the absolute values of the electrode potentials of the given systems (Table 2).

The characteristic rate of the curves  $\phi = f(\tau)$  in neutral media (3% NaCl solution) is shown in Fig. 1; it may be described by the function

$$\phi = A\tau^n, \quad (1)$$

which is more characteristic of vacuum cathodic coatings [9, 10, 15]. The observation data treatment has shown that, in the range of 5–120 min, curves 3 and 4 (Fig. 1) are described to a high precision (93–95%) by the empirical formulas  $\phi = -20t^{0.48}$  and  $\phi = -45t^{0.32}$ , respectively. In the test time range of 120–420 min, the time dependence behavior  $\phi = f(t)$  is close to linear. In the final form, the mathematical notation of the dependences  $\phi = f(\tau)$  in the given medium has the following forms:

a) thin coatings

$$\phi = \begin{cases} -45\tau^{0.32} & (5-120 \text{ min}), \\ -180(1 + 3 \times 10^{-3}\tau) & (120-420 \text{ min}); \end{cases} \quad (2)$$

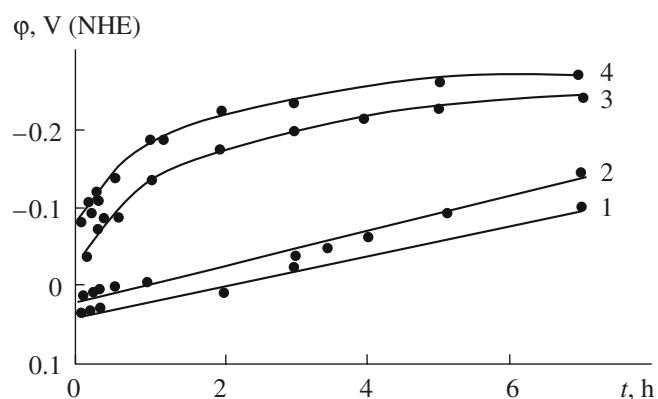


**Fig. 1.** Time variation of the electrode potentials of steel samples with titanium nitride coatings in running water ( $I$  and 2) and in a 3% NaCl solution (3 and 4),  $h$ ,  $\mu\text{m}$ : 7–8 (thick coatings) (1 and 3); 3–8 (thin coatings) (2 and 4);  $P = 0.4$  Pa;  $I = 100$  A;  $T_K = 825$  K;  $U_P = 200$  V.

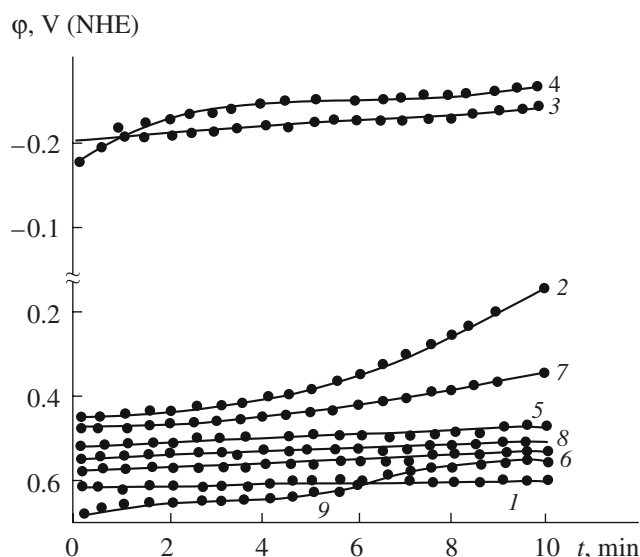


Fig. 2. Time variation of the electrode potentials of steel with titanium nitride coatings in a 3% nitric acid solution. Curves 1–8 correspond to the deposition modes in Table 2; curve 9, to the mean modes ( $P = 0.13$  Pa;  $I = 100$  A;  $U_p = 135$  V).

a) thick coatings

$$\varphi = \begin{cases} -20\tau^{0.48} & (5-120 \text{ min}), \\ -220(1 + 2.6 \times 10^{-3}\tau) & (120-420 \text{ min}). \end{cases} \quad (3)$$

In the absence of aggressive ions in the water (curves 1 and 2), the dependence  $\varphi = f(\tau)$  in the range of 5–240 min is properly described by the linear function, and, for the studied coatings, it has the form

$$\varphi = 16(1 - 2.2 \times 10^{-2}t) \text{ (thin coatings)}, \quad (4)$$

$$\varphi = 35(1 - 9 \times 10^{-3}t) \text{ (thick coatings)}; \quad (5)$$

in addition, this behavior of the dependence survives at further storing of the samples (up to 10–15 hours).

One can see from the analysis of the data of Fig. 1 and formulae (2)–(5) that the rate of the electrode potential variation in the 3% NaCl solution in the initial moments of the studies is significantly higher than in the absence of active components in the solutions. Then, the situation is changed: in aggressive environments, there practically occurs the potential stabilization; in subactive environments, the potential shift to the negative region with the same rate is observed. In the latter case, the potential stabilization takes place significantly later (in 15–18 hours). Proceeding from the known data on the environment influence on the number of “active” corrosion pits in cathodic vacuum coatings [10, 15, 16] and taking into account the fundamental notions on the interaction of stationary potentials with the coating pore content [12, 13], one can

state that the experimentally found differences of the dependences  $\varphi = f(\tau)$  (Fig. 1, formulae (2)–(5)) testify to both the different number of corrosion pits in the pores of the cathodic vacuum coatings in different aggressive environments and the different rate of their number increase with time. The latter is apparently due to the influence of the geometrical parameters of the pores on the nature of the processes in the system “coating–substrate.” The physicochemical situation in the given system may be estimated from the approach proposed in [9].

In acid media, the dependences  $\varphi = f(\tau)$  are properly described by linear functions. In particular, in the 3%  $\text{HNO}_3$  solution, four characteristic regions of the curves of the dependence  $\varphi = f(\tau)$  can be specified. At the very beginning of the tests (the first 10 min), irrespective of the deposition conditions, positive potential values with a weak shift to the negative range are observed for all the samples. The exceptional case is the samples obtained at low nitrogen pressure (Fig. 2, curves 3 and 4). The second time period of the tests (from 10 minutes to 1.5 hours) is characterized by a sharp shift of the potentials to the range of negative values. It is impossible to reveal the characteristic dependences of the  $\varphi$  variation rate on the deposition conditions; however, all the dependences are described by linear functions.

In the range of 2–6 hours, the electrode potential dependence on the accelerating voltage on the substrate  $U_p$  is available. Thus, for  $U_p = 50$  V and  $U_p = 220$  V, the time dependences are described by the equations

$$\varphi = -300 - 12\tau \text{ } (U_p = 50 \text{ V}); \quad (6)$$

$$\varphi = -250 - 15\tau \text{ } (U_p = 220 \text{ V}). \quad (7)$$

In the fourth time period (6–24 hours), the laws determined by formulae (6) and (7) take the form

$$\varphi = -375 - 0.5t \text{ } (U_p = 50 \text{ V}); \quad (8)$$

$$\varphi = -325 - 2.0t \text{ } (U_p = 220 \text{ V}). \quad (9)$$

The differences in the absolute values of the electrode potentials and in the time variation rate of the potentials of the samples obtained at different  $U_p$  count in favor of the influence of the deposition modes on the history of the electrode processes in the coating pores. Let us note that, in the  $\text{HNO}_3$  solution, the influence of  $I$  and  $P$  on the dependence  $\varphi = f(t)$  is expressed weakly.

We have applied the experiment design method for obtaining of the regression equation that connects such an electrochemical parameter as the potential or the rate of the potential variation with the corresponding factors. The first-order design with factor variation at two levels was applied [17]. Taking into account the specific character of the coating deposition by virtue of the installation “Bulat–3T,” the variable parameters were selected to be  $U_p$ ,  $P$ , and  $I$ ; the levels and ranges of their variation are presented in Table 1.

The regression equation in our case has the form

$$Y = b_0 + \sum b_i x_i + \sum b_{ij} x_i x_j, \quad (10)$$

where  $Y = \varphi$ ;  $b_0$  is the absolute term of the regression equation;  $b_i$  is the linear regression coefficient;  $b_{ij}$  is the coefficient of double factor interaction;  $x_i$  is the coded value of the factors, which is determined as

$$x_i = \frac{x_i - x_{i0}}{\varepsilon}; \quad x_{i0} = \frac{x_{imax} - x_{imin}}{2}; \quad (11)$$

$x_i$  is the running factor value; and  $x_{imax}$  and  $x_{imin}$  are the factor values at the variation levels. The  $2^3$  complete factorial matrix and the observation results are presented in Table 2. The data are given for various instants of time; the statistical analysis has been performed for the concrete observation time according to Table 2.

On the basis of the experiments carried out, some preliminary conclusions on the influence of the deposition parameters on the protective properties of the coating can be made. Taking into account the regression coefficients (Table 3), a certain influence of  $U_p$  on the values of  $\varphi$  is found; it is most obviously shown in the case of sufficiently long sample storing in the solution (for more than two hours). It is impossible to reveal specific relationships in the variation of  $\varphi$  on any studied deposition parameter.

After transformation of the regression equations to the denominated form, taking (1) into account, we obtain

$$\begin{aligned} \varphi = & -320 - 0.3 U_p - 7.2 \times 10^3 P \\ & - 0.52 I + 53 U_p P + 4 \times 10^{-3} U_p I. \end{aligned} \quad (12)$$

Equation (12) is given as an example for  $t = 6$  hours. Its analysis and the data of Tables 2 and 3 show that, as the accelerating voltage on the substrate increases, the electrode potentials shift to the positive value range (Fig. 3), this being an attribute of increased protective properties of the coatings. In terms of the purely electrochemical corrosion mechanism, this may be interpreted as a decrease of the pore content in the coatings. This conclusion is in good agreement with the known data on the influence of the deposition modes, in particular, of the accelerating voltage on the pore content of the coatings [5, 10].

As follows from Fig. 3, the behavior of the dependence  $\varphi = f(U_p)$  is determined also by two other parameters; however, it is rather difficult to reach a final conclusion on the character of this influence according to the present study results.

One can suppose only that the combination of high values of  $P$  and  $I$  is responsible for the increase of the number of ionized particles of the reacting gas and the evaporating metal. This also contributes to an increase

**Table 3.** Results of calculation of the regression coefficients (equation (10))

Experiment number	Values of the regression coefficients for the moment $t$					
	0	2 min	10 min	2 h	6 h	24 h
$b_0$	+374	+258	+214	−300	−358	−379
$b_1$	−187	−89	−100	+27	+22	+8.75
$b_2$	+194	+98	+89	−	−	−
$b_3$	+69	+109	+128	−8.0	−	−
$b_{12}$	+186	+299	+167	+13.0	+20.0	+8.75
$b_{13}$	+21	−82	−69	+17.0	+6.75	+16.0
$b_{23}$	+9.4	+116	+138	−	−	−

of the resistance power of the coatings and improvement of their protective properties. The physical properties characteristic of the selected method of coating obtaining are analyzed in detail in the literature, for example, in [21].

More accurate information on the influence of the deposition parameters on the protective properties of the coatings and their corrosion–electrochemical behavior was obtained by us on the basis of potentiodynamic studies and the analysis of polarization curves by the above-described techniques. A series of samples was specially prepared for the estimation of the influ-

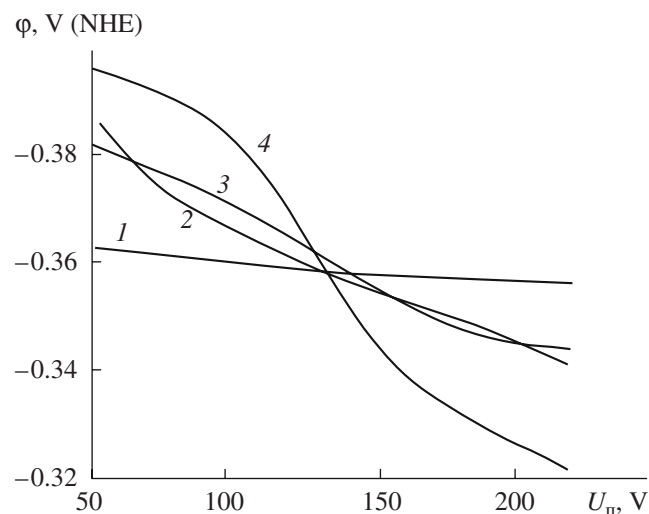


**Fig. 3.** Dependence of the electrode potentials on the value of the accelerating voltage on the substrate (equation (12)). Curves 1, 2, 3, and 4 correspond to the  $P$  combination in Table 1:  $I(-1, -1)$ ,  $(-1, +1)$ ,  $(-1, +1)$ ,  $(+1, +1)$ .

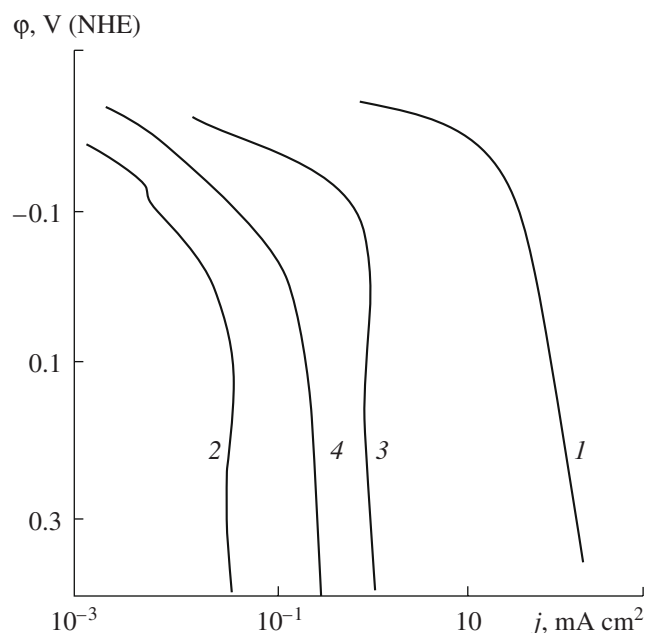


**Fig. 4.** Anode potentiodynamic polarization curves of steel 08kp (1) and titanium nitride coatings on steel (2–4) in a 3% sulfuric acid solution. The numbers of the curves correspond to the experiment numbers in Table 4.

ence of the test conditions on the corrosion–electrochemical behavior of the TiN coatings on the steel.

Taking into account the above-given dependences  $\varphi = f(\tau)$  and equation (12), the vacuum chamber pressure and the coating thickness were variable parameters; the parameters  $I$ ,  $U_p$ , and  $T_K$  remained constant in all the experiments ( $I = 100$  A,  $U_p = 220$  V, and  $T_K = 500$ – $550^\circ\text{C}$ ).

Sample potentiodynamic curves and the results of the experimental data analysis are presented in Fig. 4 and Table 4. The best protective properties of the coatings are shown in neutral dechlorinated media. The corrosion current decrease and the polarization resistance increase with the coating thickness increasing is a general yet not pronounced tendency. The difference in  $R_p$  for the samples obtained at different pressures is worth mentioning: at high  $P$ , the value of  $R_p$  is higher as a rule. This is a confirmation of the earlier-expressed supposition on the positive influence of high nitrogen pressure on the protective properties of coatings.

A comparison of the numerical values of the corrosion parameters for one type of coatings in different environments gives information on the environment's corrosive power influence on the resistance power of the coatings.

The dependences  $\varphi$ – $j$  for all the coating thickness and deposition modes are similar. In the initial polarization moments, they count in favor of a relatively free course of the anode process (the gently sloping curve runs with respect to the current density axis); as  $\varphi$

increases, the currents become higher. Beginning with a certain value of  $\varphi_p$ , the samples pass into the passive state (with the exception of the 3% NaCl solution); turning points on the  $\varphi$ – $j$  curves were not observed. This is explained by the accumulation of iron corrosion products in the coating pores and by the shielding of the correlative surface from the solution. In the 3% NaCl solution, a passivity region on the anode polarization curves was not found; this counts in favor of the high activity of chlorine–ions.

The second characteristic peculiarity is the regular shift of the polarization curves  $\varphi$ – $j$  depending on the coating thickness (Fig. 4). In the range of low currents, there are curves that correspond to the samples with thin coatings; as the thickness increases, they shift to the range of higher current densities. In addition, various variants of the relative position of the curves depending on the environment are found: in the  $\text{HNO}_3$  solution, curves 3 and 4 change places, and, in the 3% NaCl solution, they are situated proximately. However, the general tendency of the curve shift to the range of high values of  $j$  remains. We explain this fact by the manifestation of the mechanochemical mechanism of development of corrosion processes in the pores of cathodic vacuum coatings; this probability and the conditions of its realization are considered in [10, 14, 15]. Since the transition from the electrochemical mechanism of steel corrosion in coating pores to the corrosion damage process by the mechanochemical mechanism depends on many factors and is, to a certain extent, of random nature, some deviations in the behavior of the corrosion parameter variation described above in the discussion of the data of Table 4 become clear.

In conclusion, let us note one more fact important for application. For obtaining of the series of samples for the potentiodynamic studies (Table 4), their thickness was determined by the time of the coating deposition; it was identical for pairs of experiments 2–5, 3–6, and 4–7. The comparison of numerical values of  $h$  for the corresponding pairs of the experiments shows the presence of a certain dependence of the coating deposition rate on the chamber pressure value: at low pressure, the deposition rate is higher.

Studies of the deposition parameter influence on the kinetics of the TiN coating growth that were carried out with application of the experiment design method have shown that, in the range of technologically reasonable deposition parameters (see Table 1), the relation of the coating thickness and the deposition parameters is determined by the empiric formula

$$h = -28.1 - 2.38 \times 10^{-2} U_p - 10 \log P + 0.295 I - 6.2 U_p \log P + 4.24 \times 10^{-4} U_p I + 8.25 \times 10^{-2} I \log P + 1.3 \times 10^{-4} U_p I \log P, \quad (13)$$



**Table 4.** Parameters of the process of electrochemical corrosion of steel with vacuum coatings of titanium nitride

The studied sample and deposition parameters ( $P$ and $h$ )	Corr. process parameters	Values of corrosion process parameters in different environments			
		3% HNO <sub>3</sub> solution	3% H <sub>2</sub> SO <sub>4</sub> solution	3% NaCl solution	Distilled water
1. Steel 08kp	$\beta_a$	0.444	0.033	0.143	0.066
	$\beta_k$	0.033	0.067	0.111	0.045
	$R_P$	440	74	1430	10500
	$j_k$	0.022	0.13	0.019	0.0011
2. TiN coating $P = 0.4$ Pa $h = 3$ $\mu$ m	$\beta_a$	0.077	0.052	0.067	0.090
	$\beta_k$	0.100	0.087	0.605	0.80
	$R_P$	1800	10450	25000	120000
	$j_k$	0.01	0.00135	0.0011	0.0003
3. TiN coating $P = 0.4$ Pa $h = 5$ $\mu$ m	$\beta_a$	0.065	0.090	0.042	0.090
	$\beta_k$	0.042	0.067	0.29	0.154
	$R_P$	7200	9500	400000	400000
	$j_k$	0.0015	0.0018	0.00004	0.0006
4. TiN coating $P = 0.4$ Pa $h = 8.4$ $\mu$ m	$\beta_a$	0.049	0.050	0.067	0.086
	$\beta_k$	0.040	0.050	0.065	0.200
	$R_P$	15750	19250	45750	208000
	$j_k$	0.0006	0.00057	0.00027	0.0001
5. TiN coating $P = 0.13$ Pa $h = 3.5$ $\mu$ m	$\beta_a$	0.015	0.020	0.065	0.040
	$\beta_k$	0.042	0.042	0.030	0.040
	$R_P$	2475	4950	44000	55000
	$j_k$	0.002	0.001	0.0002	0.00016
6. TiN coating $P = 0.13$ Pa $h = 5.5$ $\mu$ m	$\beta_a$	0.050	0.067	0.065	
	$\beta_k$	0.030	0.067	0.068	–
	$R_P$	2600	5500	60000	
	$j_k$	0.0033	0.0265	0.00024	
7. TiN coating $P = 0.13$ Pa $h = 9.0$ $\mu$ m	$\beta_a$	0.167	0.167	0.336	0.110
	$\beta_k$	0.074	0.200	0.154	0.060
	$R_P$	2050	27800	57400	118000
	$j_k$	0.011	0.0014	0.0008	0.00015

Note:  $\beta_a$  and  $\beta_k$  are the Tafel constants for the anode and cathode reactions, respectively, V;  $R_P$  is the polarization resistance, Ohm  $\text{cm}^2$ ;  $j_k$  is the corrosion current, mA/ $\text{cm}^2$ .

whence it follows that, as the pressure increases, the thickness of the coating obtained for a certain time decreases. In addition, the character of this decrease is explained by other factors too. Accordingly, the deposi-

tion rate also decreases. This is explained by the partial sputtering of the forming coating; its intensity increases as the number of ionized molecules and atoms of gas increase at the pressure boost [21, 22].

## CONCLUSIONS

The possibility, in principle, to apply TiN coatings obtained by vacuum technology methods for protection of low-carbon steels from corrosion in neutral and acid environments is shown. The quantitative data on the parameters of the electrochemical corrosion process and the influence of the coating deposition modes on the values of the electrode potentials allow optimization of the coating deposition modes taking into account the expected operation conditions and the requirements for application of the treated metal products.

## REFERENCES

1. Andreev, V.N., Study of Efficiency of Wear-Resistant Coatings on Cutters of High-Speed Steel, *Stanki Instrum.*, 1982, no. 9, pp. 18–20.
2. Khanzarov, G.N., Magometov, B.R., and Abdullaev, E.G., Increase of Wear Resistance of Typesetting Machine Pieces with Plasma Coating, *Zashch. Met.*, 1982, vol. 18, no. 3, pp. 453–454.
3. Kostrzhitskii, A.I., Karpov, V.F., and Paskal, V.V., Methods of Wear-Resistance Coating Deposition on Pieces of Machines and Constructions, Kiev: UkrNIINTI, 1986, no. 23, Uk86. 49.
4. Karpov, V.F. and Kostrzhitskii, A.I., *Nanesenie iznosotoikikh pokrytii na instrument iz bystrorezhushchei stali* (Wear-Resistant Coating Deposition on Tools of High-Speed Steel), Kiev: UkrNIINTI, 1985, no. 2699, Uk85.
5. Golubets, V.M., Protsik, V.G., et al., Protective Properties of the 40X Steel with Titanium Nitride Coatings, *Fiziko-Khim. Mekh. Mat.*, 1983, no. 3, pp. 105–106.
6. Golubets, V.M., Protsik, V.G. et al., Influence of Plasma Vacuum Coating on Resistance to Corrosion Fatigue of Medium-Carbon Steel, *Fiz. Khim. Mekh. Mat.*, 1983, no. 5, p. 117.
7. Kostrzhitskii, A.I., Karpov, V.F., Paskal, V.V., Gusareva, O.F., and Terzeman, E.F., *Formirovanie i zashchitnye svoistva vakuumnykh pokrytii iz nitride titana na stali* (Formation and Protective Properties of Vacuum Coatings of Titanium Nitride on Steel), Kiev: UkrNIINTI, 1986, no. 486, Uk86.
8. Roikh, I.L., Lebedinskii, O.V., and Kostrzhitskii, A.I., On Protective Properties of Ion Coatings on Steel, in *Dokl. AN SSSR*, 1978, vol. 242, no. 6, pp. 1386–1389.
9. Kostrzhitskii, A.I., Electrochemistry of Local Corrosion in Pores of Cathodic Vacuum Coatings on Steel, *Fiziko-Khim. Mekh. Mat.*, 1985, no. 3, pp. 48–54.
10. Kostrzhitskii, A.I., Methods of Obtaining and Properties of Corrosion-Resistant Vacuum Multicomponent Films and Coatings, *Doctoral (Eng.) Dissertation*, Moscow: NIFKHI, 1988.
11. Kostrzhitskii, A.I., Lebedinskii, O.V., et al., Influence of Deposition Conditions on Pore Content of Copper Vacuum Coatings on Steel, *Fiz. Khim. Obrab. Mater.*, 1980, no. 1, pp. 103–107.
12. Kostrzhitskii, A.I., Lebedinskii, O.V., and Roikh, I.L., Electrochemical Finishing of the Coatings Obtained by Vacuum Ion Deposition, *Zashch. Met.*, 1979, no. 3, pp. 343–345.
13. Kostrzhitskii, A.I., On Role of Electrochemical Heterogeneity in Development of Corrosion Processes in Pores of Cathodic Vacuum Coatings, Kiev: UkrNIINTI, 1984, no. 633Uk–84Dep.
14. Kostrzhitskii, A.I., On Mechanism of Corrosion Process Development in Pores of Cathodic Vacuum Coatings on Steel, *Zashch. Met.*, 1985, vol. 21, no. 1, pp. 64–68.
15. Kostrzhitskii, A.I. and Lebedinskii, O.V., *Mnogokomponentnye vakuumnye pokrytiya* (Multicomponent Vacuum Coatings), Moscow: Mashinostroenie, 1987.
16. Kostrzhitskii, A.I., Study of Copper and Copper-Zinc Vacuum Coatings on Steel, *Cand. Sci. (Eng.) Dissertation*, Moscow: MVMI, 1978.
17. Tikhomirov, V.B., *Planirovanie i analiz eksperimenta* (Experiment Design and Analysis), Moscow: Legkaya Industriya, 1974.
18. *Korroziya. Spravochnik* (Corrosion. Handbook), Shreier, L.L., Ed., Moscow: Metallurgiya, 1981.
19. Kostrzhitskii, A.I., *Elektrokimiya planok splavov na osnove medi. Kharakter elektrodnykh protsessov pri vneshnei polarizatsii* (Electrochemistry of Copper Based Alloy Plates. Behavior of Electrode Processes at External Polarization), Kiev: UkrNIINTI, 1985, no. 526Uk–85Dep.
20. Lyapina, O.V., Physicochemical Processes on Surface of Copper Alloy Plates, *Cand. Sci. (Chem.) Dissertation*, Ivano-Frankivks: Stefanik PNU, 2006.
21. Roikh, I.L., Koltunova, L.N., and Lebedinskii, O.V., Protective Properties of Coatings Obtained by Vacuum Ion Deposition, *Zashch. Met.*, 1977, vol. 13, no. 6, pp. 549–661.
22. Lebedinskii, O.V., Kostrzhitskii, A.I., and Pribbe, S.A., Influence of Glow Discharge Parameters on Rate of Steel Substrate Sputtering, *Elektron. Obrab. Mater.*, 1979, no. 3, pp. 42–45.

## ELECTRICAL PROCESSES IN ENGINEERING AND CHEMISTRY

# Electroisothermal Convection and Its Role in the Process of Heat Exchange

F. P. Grosu<sup>a</sup> and M. K. Bologa<sup>b</sup>

<sup>a</sup> State Agrarian University of Moldova, ul. Mircheshti 44, Kishinev, MD-2049 Republic of Moldova

<sup>b</sup> Institute of Applied Physics of the Academy of Sciences of Moldova,  
ul. Academiei 5, Kishinev, MD-2028 Republic of Moldova

e-mail: mbologa@phys.asm.md

Received February 29, 2008

**Abstract**—Isothermal electrohydrodynamic phenomena in three important approximations—the isothermal, hydrostatic, and electrohydrodynamic equilibrium of dissociation–recombination processes of charge transfer in liquids—are considered. For the known mechanisms of isothermal charge formation, the influence of the electrohydrodynamic phenomena on the heat transfer is estimated by means of criterion dependencies obtained on the basis of determination of the scale of the moving force of electroconvection. The results may be used for calculations for electroconvective heat exchangers and for further study of isothermal electrohydrodynamic phenomena.

**DOI:** 10.3103/S1068375508030046

## INTRODUCTION

The intensifying effect of electric fields on convective heat exchange in liquid dielectrics was discovered long ago [1, 2] and is caused by electric convection [3] occurring under the influence of outer electric ponderomotive forces with volume density [4, 5]:

$$\vec{f} = \rho \vec{E} - \frac{1}{2} E^2 \nabla \epsilon + \frac{1}{2} \nabla \left[ \gamma \left( \frac{\partial \epsilon}{\partial \gamma} \right) E^2 \right], \quad (1)$$

where  $\gamma$  and  $\rho$  are the densities of the medium and free electric charges,  $\epsilon = \epsilon_0 \epsilon_r$  is the absolute permittivity, and  $\vec{E}$  is the electric intensity vector.

Motive forces of convective motions can be only vortex ones (their rotor is different from zero) [6]; hence, it follows that, firstly, the last summand in (1) may be omitted with the mentioned forces being analyzed and, secondly, in a locally electroneutral medium ( $\rho \equiv 0$ ), specifically in an ideal dielectric, the existence of the convection requires not only the medium nonuniformity with respect to  $\epsilon$  ( $\nabla \epsilon \neq 0$ ) but field heterogeneity ( $\nabla E^2 \neq 0$ ) as well.

In problems on heat exchange, the thermal heterogeneity is the source of the medium nonuniformity with respect to  $\epsilon$  due to the relationship  $\epsilon(T)$  and  $\nabla \epsilon = (d\epsilon/dT) \nabla T \neq 0$ . It is evidently convenient to set up heterogeneous electric fields with the help of a cylindrical system of electrodes from all points of view including their calculation. In order to find the purely 'dielectric' effect ( $\nabla \epsilon \neq 0$ ), i.e., excluding the liquid electric charging, it is desirable to conduct the experiments in alternating fields with the oscillation period being consider-

ably less than the electric relaxation time  $\tau \equiv \epsilon/\sigma$ , where  $\sigma$  is the dielectric electric conductivity [6]. Under such conditions, there are observed increases of the relative heat transfer coefficient of the heated wires stretched coaxially with the cylindrical counterelectrode  $\Delta\alpha/\alpha_0 \equiv (\alpha_E - \alpha_0)/\alpha_0 \leq (10-20)\%$ . The occurring electroconvection is called "electrothermal" (ETC).

At the same time, in steady fields and under similar conditions, the relative growth of the heat transfer coefficient amounted to 100% or more. Thus, such considerable heat exchange intensification in the electrostatic field is caused by purely coulomb forces  $\rho \vec{E}$ , i.e., the fluid electrization with the occurrence of space electric charges  $\rho \neq 0$ . This turns out to possibly explain the origination of the charges remaining in the framework of the electrothermal conceptions yet with allowance made for the weak but different from zero electric conductivity ( $\sigma \neq 0$ ) of the liquid according to the chain of equalities [7, 6]:

$$\begin{aligned} \vec{j} &= \sigma \vec{E}; \quad \nabla \vec{j} = 0 \\ \Rightarrow \rho &= \nabla(\epsilon \vec{E}) = \vec{j} \nabla \tau = \frac{d\tau}{dT} \vec{j} \nabla T, \end{aligned} \quad (2)$$

in view of the known dependencies  $\epsilon(T)$  and  $\sigma(T) \Rightarrow \tau(T)$ . Accounting for this fact led to significant progress both in the physical conception of the problem under study and in the generalization of the experimental data with the help of similarity theory criterion equations [8].

Furthermore, there was started the second stage of investigations in the sphere of electrohydrodynamics, which can be called thermoelectrohydrodynamics

(TEHD) of low-conducting liquids (LCL), embracing the sixties–seventies of the previous century, unlike the first one (the thirties) when TEHD of ideal liquids (IL) was researched.

However, full agreement between the experimental and theoretical results based on TEHD ideas wasn't obtained mainly in regard to the relationship  $\alpha_E/\alpha_0 = f(\theta_S)$ , where  $\theta_S$  is the temperature drop. With it decreasing, a great reduction of heat transfer was expected, but the mentioned dependence turned out to be suddenly weaker [8].

The search for the way out of this difficulty allowed deducing that isothermal electroconvection or electroisothermal convection (EITC), which is called so because it is observed at the presence or absence of temperature gradients, plays a significant (and sometimes a decisive) part in convective heat exchange.

Although this type of convection was discovered and investigated even by M. Faraday [9], some time later by O. Leshann [10] and E. Varburg [11], and then by A. Gyemant [12] and R. Hofmann [13], research workers began to use information on the EITC in order to explain and calculate electroconvective heat exchange after the seventies [8, 14–18], when “electrohydrodynamics” started to be developed as a scientific direction studying the interaction between electric and hydrodynamic fields [19–22].

EHD problems are connected with the central one, namely, the electrization of liquid dielectrics in outer electric fields under isothermal and electrohydrostatic conditions (originally). Works [3, 8–22] are devoted to the solution of this problem, as well as [23], in which there is presented a certain classification of liquid electrization mechanisms, mainly, equilibrium and non-equilibrium ones, depending on the existence or absence of dynamic equilibrium between the processes of dissociation of neutrals and recombination of charge carriers. In the first case, there is valid the density conservation law for total and partial currents:

$$\vec{j} = \vec{j}^+ + \vec{j}^-; \quad \text{div} \vec{j} = 0; \quad \text{div} \vec{j}^\pm = 0,$$

whereas, in the second one, partial currents don't conserve, namely,

$$\text{div} \vec{j}^\pm \neq 0. \quad (3)$$

As a rule, in what follows, we will consider EITC as applied to the first class of electrization mechanisms. Further, we neglect the convection current density when examining the electrohydrostatic approximation for the field, which is assumed in many problems of electrohydrodynamics. Owing to the isothermality of the force density, the electrohydrodynamic problem becomes independent of the thermal one (the convective heat conductivity equations) and, by virtue of the hydrostatics ( $\vec{v} = 0$ ), the EHD problem itself becomes an independent electric problem dependent on the last hydrodynamic problem. Such disintegration of the

TEHD general set is a typical feature of the problems of electroconvective heat exchange under the conditions of electroisothermal convection. Though the solution of the hydrodynamic problem supposes knowledge of the density of forces, we consider this problem as a more general one.

### 1. Peculiarities of Electroisothermal Convection and Its Intensity

The hydrodynamic part of the problem has the form

$$\gamma \left[ \frac{\partial \vec{v}}{\partial t} + (\vec{v} \nabla) \vec{v} \right] = -\nabla P + \vec{f} + \eta \nabla^2 \vec{v}; \quad (4)$$

$$\nabla \vec{v} = 0; \quad \vec{v}|_b = 0; \quad P|_b = 0,$$

where  $\vec{f}$  is the known density of forces, and the pressure is counted from boundary values assumed constant; thus, the boundary value is also homogeneous as for the rate by virtue of the adherence condition. We insert scale and dimensionless units

$$t = t_0 \cdot \tau; \quad \vec{r} = l \cdot \vec{r}_1; \quad \nabla = \frac{1}{l} \nabla_1; \quad (5)$$

$$\vec{v} = v_0 \cdot \vec{v}_1; \quad P = P_0 \cdot P_1; \quad \vec{f} = f_0 \cdot \vec{f}_1,$$

which are marked by indices the “0” and “1.”

The chosen  $t_0 = l^2/\nu$ ;  $v_0 = \nu/l$ ;  $P_0 = \gamma l^2/\nu^2$ , where  $\nu = \eta/\gamma$ ; and canceling  $\gamma \nu^2/l$  out, we obtain

$$\begin{cases} \frac{\partial \vec{v}_1}{\partial \tau} + (\vec{v}_1 \nabla_1) \vec{v}_1 = -\nabla_1 P_1 + \pi \vec{f}_1 + \nabla_1^2 \vec{v}_1; \\ \nabla_1 \vec{v}_1 = 0; \quad \vec{v}_1|_b = 0; \quad P_1|_b = 0, \end{cases} \quad (6)$$

where the dimensionless product

$$\pi \equiv \frac{f_0 l^3}{\gamma \nu^2} \quad (7)$$

appears to be a similarity criterion of EHD phenomena described by set (6), and the scale  $f_0$  is so selected that  $\vec{f}_1$  doesn't depend on it.

We search for the solution in the form

$$\vec{v}_1 \equiv \pi^m \vec{u}_1; \quad P_1 \equiv \pi P, \quad (8)$$

where  $m$  is a certain parameter that appears to differ negligibly from unity, and  $\vec{u}$  and  $P$  are the sought-for functions. Substitution of (8) into (6) gives

$$\begin{cases} \frac{\partial \vec{u}}{\partial \tau} + \pi^m (\vec{u} \nabla_1) \vec{u} = \pi^{1-m} (-\nabla_1 P + \vec{f}_1) + \nabla_1^2 \vec{u}; \\ \nabla_1 \vec{u} = 0; \quad \vec{u}|_b = 0; \quad P|_b = 0. \end{cases} \quad (9)$$



It is seen that the problem becomes self-similar with respect to the parameter  $\pi$  in two extreme cases: under a laminar regime at  $m = 1$  ( $(\vec{u} \nabla_1) \vec{u} \sim 0$ ) and a turbulent one at  $m = 1/2$  ( $\frac{\partial \vec{u}}{\partial t_1} \sim 0, \nabla_1^2 \vec{u} \sim 0$ ).

Thus, from (8), we have

$$\vec{v}_1 = \begin{cases} \pi \vec{u}(\vec{r}_1, t_2) & \text{at } \pi \ll 1; \\ \sqrt{\pi} \vec{u}(\vec{r}_1, t_1) & \text{at } \pi \gg 1. \end{cases} \quad (10)$$

For the dimensional velocity, we can write

$$\vec{v} = \frac{v}{l} \pi^m \vec{u}(\vec{r}_1, t_1), \quad (11)$$

where  $1 \geq m > 1/2$ , with  $m$  subsiding from 1 to  $1/2$  as convection develops from the laminar regime to the turbulent one.

As follows from (11),

$$\text{Re}_S \equiv \pi^m \quad (12)$$

plays the role of the Reynolds number characterizing the intensity of the convective motions caused by the outside motive force. Note that the transition of the laminar regime into the turbulent one can have a discontinuous character, for instance, at the flow in a straight tube when  $(\vec{v} \nabla) \vec{v} \equiv 0$  at arbitrary large  $\text{Re}$ , or a continuous character as in the case of infiltration (Darsi's law) when the flow has from the onset a chaotic character though it is laminar in terms of  $(\vec{v} \nabla) \vec{v} \sim 0$ . A similar situation is possible in the case of electroconvective flows when  $f_0 = \rho_0 E_0$  is the electric force scale, and  $\text{Re}_S$  becomes the Reynolds "electric" number

$$\text{Re}_E \equiv \left( \frac{f_0 l^3}{\gamma v^2} \right)^m, \quad (13)$$

characterizing the intensity of the isothermal electroconvective motions depending on the specific values  $f_0(E)$ . In addition, it should be kept in mind that the equilibrium density of forces  $\vec{f}_0$  should satisfy the necessary condition of the convection origin—antiparallelism of the vectors  $\vec{E} \uparrow \downarrow \nabla \rho$  or  $\vec{E} \nabla \rho < 0$  [8].

Thus, mathematically, the main peculiarity of electrophysical convective phenomena is that the electrohydrodynamic part of the problem is separated from the thermal one and, in the electrohydrostatic approximation (EHS), the electric part becomes independent. Physically, this means that the ponderomotive electric force assumes a pure Coulomb character of the outside isothermal force, thus making it possible to enter a number similar to the Reynolds number but with an electroconvective nature. Simultaneously, it has become possible without solution of the problem's

electric part to find the dependence of this similarity criterion on the main force  $\pi$ , namely,  $\text{Re}_E \sim \pi$  under the convection laminar regime and  $\text{Re}_E \sim \sqrt{\pi}$  under the turbulent one. On this basis, we can make good progress in establishing the general regularities of the electroconvective heat exchange (ECHE) using a store of problems and their solutions for heat transfer at the forced motion of the heat carrier [24, 25].

## 2. General Regularities of Heat Exchange under the Conditions of Electroisothermal Convection

The general regularities of the convective heat exchange are based on the notions of the boundary layer, specifically, the Nusselt number proportional to the heat transfer coefficient is generalized by the formula

$$Nu = F(\text{Pr}) \text{Re}^n = F(\text{Pr}) \text{Re}^{0.5-0.8} \quad (14)$$

through the inverse proportionality of the heat flow to the thickness of the hydrodynamic boundary layer and the relations with the thickness of the heat boundary layer [24, 25] with  $n = 0.5$  in the case of the laminar boundary layer and  $n = 0.8$  with turbulent one, which virtually doesn't occur in EC problems;  $F(\text{Pr})$  is a proportionality coefficient depending on the Prandtl number  $\text{Pr} = \nu/a$ , where  $a$  is the thermal diffusivity of the medium. This number appears in the heat part of the problem, which is described by the equation of convective heat conduction [24]

$$\vec{v} \nabla T = a \nabla^2 T, \quad (15)$$

which, after being brought to the dimensionless form with the help of the substitutions

$$\vec{v} = v_0 \vec{v}_1 = \frac{v}{l} \vec{v}_1; \quad T = \theta_S T_1; \quad \nabla = \frac{1}{l} \nabla_1,$$

where  $\theta_S$  is the temperature drop (head), becomes

$$\text{Pr}(\vec{v}_1 \nabla_1) T_1 = \nabla_1^2 T_1.$$

As the specific heat flow is proportional to the temperature gradient  $\vec{q} \sim \nabla T$ , it is natural for the occurrence of the coefficient  $F(\text{Pr})$  depending on the  $\text{Pr}$  number in formula (14). With the electric field being present under the conditions of isothermal convection in (14),  $\text{Re} \rightarrow \text{Re}_E$  should be replaced with formula (13):

$$\begin{aligned} Nu_E &= F(\text{Pr}) \text{Re}_E^n = F(\text{Pr}) \left( \frac{f_0 l^3}{\gamma v^2} \right)^{nm} \\ &= F(\text{Pr}) \pi^{0.5-0.25}, \end{aligned} \quad (16)$$

where the exponent is  $0.5 \geq mn \geq 0.25$  (it is assumed that  $n = 0.5$ ). The relative narrowness of this interval in the wide range of the convection regimes is one of the general regularities of the heat transfer of solids to dielectric fluids under EITC.

### 3. The General Problem of Isothermal Electrization of a Liquid Dielectric as Applied to Heat Exchange

The initial three equations of the chain (2) constitute a part of the fundamental equations of Maxwell electrodynamics in the stationary case ( $\partial/\partial t = 0$ ), where, with the second and the third ones being accurate, the first equation requires supplementation by the current densities of convection  $\rho \vec{v}$  and diffusion in compliance with the Nernst–Planck equations [26, 20]. Then, in the approximation of the bi-ion system and the identity of the diffusion coefficients ( $D^\pm \equiv D$ ) and the mobility ( $k^\pm \equiv k$ ) of the charge carriers, we have

$$\vec{j} = \sigma \vec{E} + \rho \vec{v} - D \nabla \rho. \quad (17)$$

The appearance in (17) of the summand containing the velocity  $\vec{v}$  is principal as it makes the hydrodynamic and electric parts of the problem interdependent thus casting some doubt on the possibility of selecting the scale  $f_0$  for the force in such a way as for the dimensionless force  $\vec{f}_1$  to be independent of it, which could effect the accuracy of formulas (10), (11) from the viewpoint of the independence of  $\vec{u}$  of the parameter  $\pi$  and other dimensionless parameters. However, with reference to the heat exchange problems, in the long run, these short comings can be corrected in view of the dependence (16) of the similarity criterion characterizing the extent of the through conduction current density relation to the convective current density according to the following formulas:

$$\frac{\sigma E}{\rho v} \sim \frac{\sigma E}{(\epsilon E/l)(v/l)} \equiv \frac{l^2}{v\tau} \equiv \pi_1. \quad (18)$$

Less principal is the adding into (17) of the diffusion current, as it doesn't disturb the independence of the problem's electric part from the hydrodynamic one. Conforming to the criterion generalizations on the heat exchange, there can be inserted one diffusion criterion reflecting the relation of the through conductance currents to the diffusion ones in accordance with the known relationships:

$$\frac{|\sigma \vec{E}|}{|D \nabla \rho|} \sim \frac{\sigma E l^2}{D \epsilon E} \equiv \frac{l^2}{D \tau} \equiv \pi_2. \quad (19)$$

Notice that  $l^2/v \equiv \tau_v$  is the mechanical relaxation time and  $l^2/D \equiv \tau_D$  is the diffusion relaxation time; therefore, the criteria  $\pi_1$  and  $\pi_2$  can be physically interpreted as the relationship of the respective relaxation times:

$$\pi_1 \equiv \tau_v/\tau; \quad \pi_2 \equiv \tau_D/\tau. \quad (20)$$

With  $\pi_1$  and  $\pi_2 \rightarrow \infty$ , there occurs the extinction with respect to these criteria, meaning quick electric modifications of the physical system against the background of the slow hydrodynamic and diffusion ones, which is expressed in the neglect in (17) of the convec-

tion and diffusion currents. However, more accurate and general criterion generalization of the test data on heat exchange in comparison with (16) should be used:

$$Nu_E = F(\text{Pr}) \pi_1^p \pi_2^q \pi^{nm}, \quad (21)$$

where the exponents  $p$  and  $q$  should be determined experimentally, and  $nm$  should be refined in accordance with the predicted range.

We'll assign other special peculiarities of the heat exchange at EITC while actually selecting the main scale for the force  $f_0$  with concrete examples.

### 4. Particular ECHE Cases

We'll consider several ECHE models on the basis of problems on isothermal electrification of dielectric liquids [23].

**4.1. Heat exchange under the conditions of electromechanical convection**, i.e., in heterogeneous systems such as emulsions, suspensions, etc., is a typical electroisothermal convective phenomenon. In this case, the charges accumulate on the surface of dispersed particles with the surface density of the charges at the interface being defined by the formula

$$\gamma = j_n(\tau_2 - \tau_1) \equiv j_n\{\tau\}, \quad (22)$$

where  $\{\tau\} \equiv \tau_2 - \tau_1$  is the relaxation time jump at the interface, the index "1" refers to the dispersed phase, and "2" refers to the closed one. We find the scale for the forces from considerations of the process's specific character; the system dispersion in this case is

$$f_0 = q_0 n_0 E_0,$$

where  $q_0 n_0 \equiv \rho_0$  is the density of the space charges caused by the dispersed particles carrying the charge  $q_0$  at the concentration  $n_0$ , which, according to (22), is due to the difference of the relaxation times [8]:

$$\rho_0 = q_0 n_0 \sim \epsilon_2 E_0 \left(1 - \frac{\tau_1}{\tau_2}\right) n_0 r^2,$$

where  $r$  is the radius of the particles supposed to be spherical and of the same size. The concentration of particles is  $n_0 = c/v_1 \sim c/r^3$ , where  $c$  is the mass concentration, and  $v_1$  is the volume of one particle.

In total,

$$f_0 \equiv \frac{c \epsilon_2 E_0^2}{r} \left(1 - \frac{\tau_1}{\tau_2}\right). \quad (23)$$

In practically important cases,  $\tau_1 \ll \tau_2$  and the second summand in brackets (23) can be neglected. Then, from (7), in view of (23), we obtain (the indices at  $\epsilon$  and  $E$  are omitted)

$$\pi = \frac{\epsilon E^2 l^2 c l}{\gamma v^2 r}. \quad (24)$$

In this problem, with great accuracy, the diffusion can be neglected in view of  $\pi_2 \rightarrow \infty$ , but there appears one more dimensionless product  $cl/r$ . Taking into consideration that, at any nonzero values of the concentration  $c$ , this criterion degenerates in view of the very large values of  $l/r \gg 1$ , the Reynolds number in accordance with (24) should be defined by the formula

$$Re_E = \left( \frac{\varepsilon E^2 l^2}{\gamma v^2} \right)^{1-0.5} \left( \frac{cl}{r} \right)^{1-0}. \quad (25)$$

With allowance made for (25), for the number  $Nu_E$  from (21), we find

$$Nu_E = F(Pr) \left( \frac{\varepsilon E^2 l^2}{\gamma v^2} \right)^{0.5-0.25} \left( \frac{cl}{r} \right)^{0.5-0}. \quad (26)$$

The exponents reduce as the electroconvective process develops. The criterion  $\pi_1$  in this problem turned out odd. The experimental data on the heat transfer from a flat disc surface to emulsions in a uniform field are generalized by the relationship [8]

$$Nu_E = 5.8 \left( \frac{\varepsilon E^2 d^2}{\gamma v^2} Pr \right)^{0.26},$$

which agrees with what was theoretically predicted (26). The closeness of the exponent to the “turbulent” boundary of the range of  $0.5 \geq mn \geq 0.25$  indicates that there occurs a medium with violent electroconvective mixing, which is observed clearly by sight [27]. This is also the explanation for the disappearance (extinction) of the dependence on the concentration  $c$ , i.e., on the simplex  $ldl/r$ .

Under similar conditions in suspensions, there is ascertained the criterion experimental relationship [8]

$$Nu_E = 0.46 c^{0.33} \left( \frac{\varepsilon E^2 d^2}{\gamma v^2} Pr \right)^{0.36} \left( \frac{Pr_w}{Pr_l} \right)^{0.25},$$

which also agrees with what was theoretically expected (26). The exponent's higher value (0.36) than in the case of emulsions ( $mn = 0.26$ ) points to the less intensive electrohydrodynamic effects. This is also proved by the onset of the dependence on  $\sim c^{0.33}$ .

Thus, relationship (26), which was obtained on the basis of general theoretical considerations, is completely confirmed experimentally, thus testifying to the justifiability of the physical conceptions concerning the mechanism of isothermal electroconvection in heterogeneous media.

**4.2. Heat exchange at unipolar conduction (corona discharge).** At corona discharge in gases, there occurs a unipolar conduction caused by ions in the area of the corona electrode outside the corona layer [28]:

$$\vec{j} = \kappa \rho \vec{E}, \quad (27)$$

where  $\kappa$  is the mobility of the ions in the corona electrode area. This formula allows us to find the scale for the force

$$f_0 = j/\kappa. \quad (28)$$

Substituting (28) into (16) brings us to the theoretically expected relationship

$$Nu_E = F(Pr) \left( \frac{j l^3}{\kappa \gamma v^2} \right)^{0.5-0.25}. \quad (29)$$

For gases  $Pr \approx 1$ ; therefore,  $F(Pr) = \text{const}$ .

This relationship is thoroughly checked for the heat transfer of a corona wire stretched coaxially with a cylinder electrode (both in the horizontal and vertical position) for various gases (air, carbon dioxide, argon, helium) at different pressures admissible for the conditions of corona discharge existence, for instance, in He from 0.2 up to 20 at. Relationship (29) is completely confirmed [29].

There are grounds for believing that the “electric wind” phenomenon attending the corona discharge is also realized in dielectric liquids in a greatly nonuniform field; therefore, dependencies close to (29) with the same exponents should be observed in liquids too [30].

**4.3. Generalization of the case of unipolar conduction.** For partial densities of conduction electric currents, the following can be written:

$$\vec{j}^+ = \kappa^+ \rho^+ \vec{E}; \quad \vec{j}^- = \kappa^- \rho^- \vec{E}. \quad (30)$$

Hence, it follows that

$$\rho \vec{E} = \frac{\vec{j}^+}{\kappa^+} - \frac{\vec{j}^-}{\kappa^-} \Rightarrow \rho E = \frac{j^+}{\kappa^+} - \frac{j^-}{\kappa^-}, \quad (31)$$

where the colinearity of vectors involved in (30), (31) is taken into account. As current forces are measured quantities, it is more convenient to represent (31) through the sum and difference  $\vec{j}^\pm$  and  $\kappa^\pm$  by the formulas

$$\begin{cases} \vec{j}^+ + \vec{j}^- \equiv \vec{j}; & \kappa^+ + \kappa^- \equiv \mathfrak{K}; \\ \vec{j}^+ - \vec{j}^- \equiv \vec{\delta}_j; & \kappa^+ - \kappa^- \equiv r. \end{cases} \quad (32)$$

Solving set (32) with respect to  $\vec{j}^\pm$  and  $\kappa^\pm$  and substituting these values into (31) we find

$$\rho \vec{E} = \frac{2(\vec{\delta}_j \mathfrak{K} - \vec{j} r)}{\mathfrak{K}^2 - r^2} \Rightarrow \rho E = \frac{2(\delta_j \mathfrak{K} - jr)}{\mathfrak{K}^2 - r^2}. \quad (33)$$

Formulas (30) and all the others are general in the cases of the presence of only through conduction currents when

$$\sigma = \sigma^+ + \sigma^- = \kappa^+ \rho^+ + \kappa^- \rho^-, \quad (34)$$

and formulas (31), (33) are the generalization of the special case of corona discharge (unipolar conduction)

when one of the current partial densities drops out, for example, at  $j^- = 0 \Rightarrow \delta = j \Rightarrow$ :

$$\rho E = \frac{2j(\mathfrak{N} - r)}{(\mathfrak{N} - r)(\mathfrak{N} + r)} = \frac{j^+}{\kappa^+} \equiv \frac{j}{\kappa} = f_0$$

according to formula (28).

Here and henceforward, we shall restrict ourselves to the simulation of ECTE in a parallel-plate capacitor with one plate serving as the heat-release surface. Then, all the field characteristics considered in EHS approximation may be functions of the coordinate  $x$  normal to the plates; however,  $j^\pm$  and  $j$  in the accepted approximation of the dynamic equilibrium (item 1) should be constant. Thus, the force presented by expression (33) will be constant too, and it will be accepted as the scale for  $f_0$ . Assuming  $\kappa^+ = \kappa^- = \kappa$ , we have

$$f_0 = \delta_j / \kappa. \quad (35)$$

We'll verify the required condition for convection origination. With this aim, we'll find the electric intensity distribution by solving equation (31):

$$\varepsilon E' E \equiv A; \quad A \equiv (j^+ / \kappa^+) - (j^- / \kappa^-) = \text{const.}$$

We find

$$E = \sqrt{\frac{2Ax}{\varepsilon} + c} \Rightarrow \vec{E} \nabla \rho = \varepsilon E E'' = -\frac{1}{\varepsilon} \left( \frac{A}{E} \right)^2 < 0 \quad (36)$$

at any sign of  $A$ . Thus, the equilibrium is unstable and electroconvection is possible.

The only change of heat transfer equation (29) is that, instead of the current density  $j$ , we will figure the difference of the partial currents  $\delta_j = j^+ - j^-$ , which should be accepted with respect to the absolute magnitude.

In this mechanism of charging, the experimental estimation of  $j^+$  and  $j^-$  separately is problematic. The determination of the current densities in the "needle-plate" system of electrodes at different polarities and voltages and their preassigned values is probably one way of solution.

**4.4. Separation of the "charged component" in electric conduction.** Another generalization of the unipolar electric conduction case is the presentation of the conductivity in the form

$$\sigma = \sigma^0 + \kappa \rho, \quad (36a)$$

where  $\kappa$  is the mobility of the surplus charges (causing the space charge), which can be called the "charged" component, and  $\sigma_0 = \text{const}$  is the "background" "electroneutral" component. In the special case  $\sigma^0 = 0$ , we obtain the unipolar conduction item 4.2. The conduction model (36.a) is used also in relaxation problems [31]. Substituting into (2)  $\tau = \varepsilon / \sigma$ , where  $\varepsilon = \text{const}$ , and  $\sigma$  is expressed by formula (36.a), we obtain the differential equation for  $\rho$  [23]:

$$\varepsilon \kappa j \nabla \rho = -\rho (\sigma^{(0)} + \kappa \rho)^2, \quad (37)$$

the solution of which for a parallel-plate capacitor at the boundary condition at the heat-release surface

$$\rho(x)|_{x=0} = \rho_0 \quad (38)$$

has the form [23]

$$\ln \frac{\theta(1+\beta)}{1+\beta\theta} + \frac{1}{1+\beta\theta} - \frac{1}{1+\beta} = -\xi, \quad (39)$$

where it is denoted as

$$\theta \equiv \rho / \rho_0; \quad \xi \equiv x / \delta_p; \quad \beta \equiv \kappa \rho_0 / \sigma^0; \quad \delta_p \equiv \varepsilon \kappa j / (\sigma^0)^2. \quad (40)$$

We restrict ourselves to  $\beta \ll 1$  when from (39) we obtain the formula

$$\rho = \rho_0 l^{-\frac{x}{\delta_p}}, \quad (41)$$

indicating a quick diminishing of the charge density  $\rho$  when moving away from the electrode surface. The electric intensity is obtained by integration of (41):

$$E(x) = E_\infty - \frac{\rho_0 \delta_p}{\varepsilon} l^{-\frac{x}{\delta_p}}, \quad (42)$$

where  $E_\infty$  is the intensity far from the electrode surface ( $x \gg \delta_p$ ).

As the scale for the force  $f_0$ , it is logical to take the average value in the range  $0 \leq x \leq \delta$  of the hydrodynamic layer thickness, i.e.,

$$\begin{aligned} f_0 \equiv \bar{f} &= \frac{1}{\delta} \int_0^\delta \rho(x) E(x) dx \\ &= \frac{1}{\delta} \left[ \rho_0 \delta_p E_\infty \left( 1 - l^{-\frac{x}{\delta_p}} \right) - \frac{\rho_0^2 \delta_p^2}{2\varepsilon} \left( 1 - l^{-\frac{2\delta}{\delta_p}} \right) \right]. \end{aligned}$$

The estimates show that  $\delta \gg \delta_p$  and the second summand in square brackets is negligibly small in comparison with the first one, so we assume

$$f_0 = \frac{\rho_0 \delta_p E_\infty}{\delta}.$$

Substituting  $\delta_p$  from (40) and with  $E_\infty = u/l$  with  $u$  being the voltage on the capacitor, we obtain

$$f_0 = \frac{\rho_0 \kappa j u \tau^2}{\delta \varepsilon l}. \quad (43)$$

For the number  $\text{Re}_E$ , from (13) according to (43), we find

$$\text{Re}_E = F(\text{Pr}) K^{\frac{m}{1-0.5m}}; \quad K \equiv \frac{\rho_0 \kappa j u \tau^2 l}{\varepsilon \gamma v^2}, \quad (44)$$

where it is taken into account that the hydrodynamic boundary layer thickness  $\delta$  with the accuracy of the



proportionality coefficient depending on the Pr number [24] is  $\delta \sim \text{Re}_E^{1/2} l$ . Taking into consideration formulas (44) for the  $Nu_E$  number, the following generalized relationship in the electrization model (36a) under study can be predicted:

$$Nu_E = F(\text{Pr}) K^{\frac{nm}{1-0.5m}} = F(\text{Pr}) K^{\frac{0.5m}{1-0.5m}} \quad (45)$$

$$= F(\text{Pr}) K^{1-\frac{1}{3}},$$

with the exponent of the criterion  $K$  diminishing from 1 to 1/3 as convection develops from weak to strong convective flows. Note that relationship (45) allows additions by simplex multipliers of the  $\pi_1, \pi_2$  type (20).

**4.5. Diffusion model.** Let's consider one more model when the diffusion current is taken into account according to (17) where  $\vec{v} \equiv 0$  (the EHS approximation) and  $\sigma = \text{const}$  is some average value with respect to the volume. The mathematical problem definition is as follows:

$$E'' - E/\delta_D^2 = j/\varepsilon D; \quad E(x)|_{x=l} = E_0; \quad (46)$$

$$E'(x)|_{x=l} = 0,$$

where  $\delta_D$  is the Debye layer thickness  $\equiv \delta_D = \sqrt{\tau D}$ ,  $0 \leq x \leq 2l$ , and  $x = l$  is the capacitor middle.

The field intensity in the center of the capacitor  $E_0$  can be expressed through the potentials of the plates ( $\pm u$ ) according to the initial conditions for  $\varphi(x)$ :

$$\varphi(0) = u; \quad \varphi(l) = 0; \quad \varphi(2l) = -u.$$

The final solution has the form [23]

$$E(x)/\bar{E} \equiv r(x) = \omega + \frac{1-\omega}{a} \text{ch} v(x), \quad (47)$$

where it is denoted as

$$\omega \equiv j/\sigma \bar{E}; \quad a \equiv \frac{\text{sh} \mu}{\mu}; \quad \mu \equiv l/\delta_D; \quad (48)$$

$$v(x) = \frac{l-x}{\delta_D}; \quad \bar{E} = \frac{u}{l}.$$

As in the previous example, we average the force  $\rho E$  with respect to the hydrodynamic boundary layer being preliminarily calculated:

$$\rho = \varepsilon \bar{E} r'(x) = -\frac{\varepsilon u \mu^2 (1-\omega)}{l^2 \text{sh} \mu} \text{sh}(x). \quad (49)$$

Then,

$$f_0 = \vec{f} = \frac{1}{\delta} \int_0^\delta \rho E dx = \frac{\varepsilon \bar{E}^2}{2\delta} [r^2(\delta) - r^2(0)]. \quad (50)$$

Let's estimate the difference  $(r(\delta) - r(0))$  and the sum  $(r(\delta) + r(0))$ :

$$r(\delta) - r(0) \equiv \left( \frac{dr}{d\delta} \right)_0 \delta = \frac{\delta}{\delta_D} \mu (\omega - 1) \equiv \Delta; \quad (51)$$

$$r(\delta) + r(0) \equiv 2[\omega - \mu(\omega - 1) \text{cth} \mu] \quad (52)$$

$$\equiv 2[\omega - \mu(\omega - 1)] \equiv S,$$

as  $\delta_D \ll \delta \ll l$ .

In the case of homocharges at the electrode [23],  $\omega > 1 \Rightarrow \Delta > 0$ , and the convection to occur there should entail  $S > 0$  as well as  $f_0 \sim \Delta S$ . Hence, we obtain one more condition for the appearance of electroconvection:

$$\omega > \frac{\mu}{\mu - 1} \equiv 1 + \frac{1}{\mu} \Rightarrow \omega - 1 > \frac{1}{\mu}, \quad (53)$$

$$\text{as } \mu \gg 1 \Rightarrow \frac{1}{2} S = \omega - \mu\omega + \mu \equiv \omega - \mu + \mu = \omega.$$

Thus,  $S = 2\omega \approx 2$  and the force scale is

$$f_0 = \frac{\varepsilon \bar{E}^2}{2\delta} \frac{\delta}{\delta_D} \mu (\omega - 1) 2\omega \Rightarrow f_{0 \min} = \frac{\varepsilon \bar{E}^2}{\delta}. \quad (54)$$

Substitution of (54) into (16) gives

$$Nu_E = F(\text{Pr}) \left( \frac{\varepsilon l u^2}{\delta_D \gamma v^2} \right)^{0.5-0.25} \sim u^{1-0.5}, \quad (55)$$

i.e., at the realization of this model, the heat transfer is linear with respect to the voltage under the laminar regime and is root under the turbulent one.

## CONCLUSION

Thus, the hydrodynamic aspects of liquid isothermal electrization phenomena have been considered from the point of view of equilibrium mechanisms of current passage, as well as the effects of these phenomena on the processes of convective heat exchange. The obtained results can be used both in practice and for the further study of EHD phenomena by thermodynamic methods. Investigations considering the nonisothermality and nonhydrostatics of electrization processes at their nonequilibrium mechanisms merit attention.

## REFERENCES

1. Sentfleben, H.Z., *Phys*, 1931, vol. 32, p. 550.
2. Alad'ev, I.T. and Efimov, V.A., *Inzh. Fiz. Zhurn.*, 1963, vol. 6, no. 8, pp. 125-132.
3. Ostroumov, G.A., Electric Convection (review), *Inzh. Fiz. Zhurn.*, 1966, vol. 10, no. 5, p. 683.
4. Landau, L.D. and Lifshits, E.M., *Elektrodinamika sploshnykh sred* (Electrodynamics of Continuous Media), Moscow: Fizmatgiz, 1957.

5. Panovskii, V. and Fillips, M., *Klassicheskaya elektrodinamika* (Classic Electrodynamics), Moscow: Fizmatgiz, 1963.
6. Grosu, F.P. and Bologa, M.K., Forces Causing the Electric Convection of Low-Conductivity Liquids, *Electron. Obrab. Mater.*, 1970, no. 2, pp. 14–19.
7. Stratton, J., *Teoriya elektromagnetizma* (Electromagnetic Theory), Moscow-Leningrad: Gostekhizdat, 1948.
8. Bologa, M.K., Grosu, F.P., and Kozhukhar', I.A., *Electroconveksiya i teploobmen* (Electroconvection and Heat Transfer), Kishinev: Shtiintsa, 1977.
9. Faraday, M., *Ekspperimental'nye issledovaniya po elektrichestvu, tom. 1* (Experimental Researches in Electricity, vol. 1), Moscow: AN SSSR, 1947.
10. Leshann, O., Effect of the Electric Forces on the Liquids, *Molec.Phys.*, 1888, vol. 54, no. 3.
11. Varburg, E., *Annal.Phys.*, 1895, vol. 54, no. 4.
12. Gyemant, A., *Electrot Z.*, 1929, vol. 32, p. 1225.
13. Hofmann, R.Z., *Phys.*, 1934, vol. 92, p. 759.
14. Jones, T.B., Electrohydrodynamically Enhanced Heat Transfer in Liquids (Review), *Adv. in Heat Transfer*, 1978, vol. 14, pp. 104–148.
15. Mocluskey, F.M., Atten, P., Perez, A.T., Heat Transfer Enhancement by Electroconvection Resulting from an Injected Space Charge between Parallel Plates, *Int. J. Heat Mass Transfer*, 1991, vol. 34, no. 9, pp. 2237–2250.
16. Kozhukhar', I.A., Heat Transfer under the Conditions of Electric Convection, *Doctoral (Eng.) Dissertation*, Kiev, 1992, 47 p.
17. Zhakin, A.I., *Electrohydrodynamics: Basic Concepts, Problems and Applications*, Kursk: Kursk University, 1996.
18. Apfel'baum, M.S., On Distributions of Electric Fields in Some Types of Stationary Slightly Ionized Streams, *Electron. Obrab. Mater.*, 2007, no. 1, pp. 31–46.
19. Gogosov, V., Polyanskii, V., et al., *Prikl. Mekh. Mat*, 1969, vol. 33, no. 2, pp. 232–241.
20. Ostroumov, G.A., *Vzaimodeistvie elektricheskikh i gidrodinamicheskikh polei* (Interaction of Electric and Hydrodynamic Fields), Moscow: Nauka, 1979.
21. Rubashov, I.B. and Bortnikov, Yu.S., *Electrogazodinamika* (Electric Gas Dynamics), Moscow: Gostekhizdat, 1971.
22. Stishkov, Yu.K. and Ostapenko, A.A., *Electrogidrodinamicheskie techeniya v zhidkikh dielektrikakh* (Electrohydrodynamic Flows in Liquid Dielectrics), Leningrad: LGU, 1989.
23. Grosu, F.P., Bologa, M.K., et al., Charge Formation in Liquid Dielectrics under the Action of Electrostatic Field, *Electron. Obrab. Mater.*, 2007, no. 5, pp. 15–38.
24. Landau, L.D. and Lifshits, E.M., *Mekhanika sploshnykh sred* (Mechanics of Continuous Media), Moscow: Fizmatgiz, 1954.
25. Isachenko, V.P., Osipova, V.A., and Sukomel, A.E., *Teploperedacha* (Heat Transfer), Moscow: Energiya, 1969.
26. Plank, M., Uber die Efreugung von Elektricitat und Warme in Elektrolyten, *Ann. Phys. Chem.*, 1890, vol. 39, pp. 161–186.
27. Lazarenko, B.R., Kozhukhar', I.A., and Bologa, M.K., *Int. J. Heat Mass Transfer*, 1975, vol. 18, pp. 589–596.
28. Kaptsov, N.A., *Elektricheskie yavleniya v gasakh i vakuumе* (Electric Phenomena in Gases and Vacuum), Moscow: Gostekhizdat, 1950.
29. Lazarenko, B.R., Grosu, F.P., and Bologa, M.K., Convective Heat Transfer Enhancement by Electric Fields, *Int. J. Heat Mass Transfer*, 1975, vol. 18, pp. 1433–1441.
30. Petrichenko, N.A., *Electric Wind in Isolating Liquids, Cand.Sci. (Eng.) Dissertation*, Leningrad, 1973.
31. Tsyrlin, L.A., On Non-Stationary Currents in Bodies with Small Intrinsic Conduction, *Vopr. Matem. Fiz.*, Leningrad: Nauka, 1976, pp. 143–151.

---

ELECTRICAL PROCESSES  
IN ENGINEERING AND CHEMISTRY

---

# One-Dimensional Nonstationary Calculation of Prebreakdown Electrodynamic Characteristics of Weakly Ionized Media

M. S. Apfel'baum

*Institute of Thermal Physics of Extreme States, Joint Institute of High Temperatures, Russia Academy of Sciences,  
ul. Izhorskaya 13, stroeniye 2, Moscow, 125412 Russia*

*e-mail: msa@ihed.ras.ru*

Received December 14, 2007

**Abstract**—A theoretical model of electrohydrodynamic prebreakdown phenomena in a weakly ionized media is proposed. Differential equations and initial conditions for describing it are written. The 1D analytical and numerical solutions of these equations for the calculations of the current time characteristics are given.

**DOI:** 10.3103/S1068375508030058

## INTRODUCTION

Sufficiently considerable Ohm's law deviations concerning the solid weakly conducting media in the prebreakdown constant in time applied fields of the plane capacitor were experimentally discovered by Poole [1]. Later on, the nonlinear deviations from this law, both in homogeneous and highly nonhomogeneous prebreakdown applied electric fields, were observed in liquid and gas weakly conducting media.

Theoretically, the investigated media conductivity growth with the intensity module increase of the electric field was grounded by Frenkel [2] by means of the Arrhenius type of equations for the rate of volume ionization taking into account the decrease of the potential of such ionization by a strong electric field. A similar kind of work yield decrease in a prebreakdown field was determined by Schottky and Onsager, who, using physical kinetics methods, obtained an expression mathematically close to Frenkel's one for the dependence of the prebreakdown rate of dissociation in weak electrolytes upon the intensity module of the electric field. However, while being analytically obtained with respect to such velocities and the stationary dependencies of the conductivity upon the electric field intensity value limited by the prebreakdown field, a certain factor was not taken into consideration by Onsager and Frenkel, namely, the influence of the charged particles drift in this field, their hydrodynamic (gas-dynamic) transfer (one should note that solid weakly conducting media are not discussed in this paper), and the diffusion caused by their volume concentrations gradient upon the spatial distribution of those concentrations. Neither of the abovementioned works nor the later ones investigated the time changes of the prebreakdown electrodynamic characteristics, which were observed in the tests with a high voltage source of the direct applied voltage

of the procedures (the application of a source of alternating in time high voltage with a theoretical description of the corresponding experiments is also not discussed by the author of the present paper).

On the basis of the previously derived electrohydrodynamic differential equations of the prebreakdown charge formation in the weakly conducting media, the author of the present paper showed (e.g., in [3 and 4]) that, in order to make use of the Frenkel and Onsager formulas for the calculation of the stationary conductivity of the investigated media, it is enough to preserve the conditions of their electric (plasma) quasi-neutrality. In this case, the density of the space charge being formed in the prebreakdown fields should be much lower than the plasma density of the self-neutralizing background of the charges with different signs. Then, according to [4], the system of the electrodynamic equations of the charge formation can be solved regardless of the system of hydrodynamic equations for the velocity commensurability of the media flows and ionic drift in the electric field, considering that, in the hydrodynamic equations of motion of sufficiently dense and thermal conducting media in a strong electric field (which are also mentioned in this paper), the influence of viscosity should be taken into account according to [5]. It is also believed that free electrons in such media generally attach the neutrals; therefore, an additional macroscopic electron component is not considered in this paper.

In the case of a plane high-voltage capacitor, stationary (steady) exponential volt-ampere characteristics can be easily obtained from the Frenkel formula for the conductance and the equation of the charge conservation in a differential form. In the case of a spherical capacitor, the distribution of the stationary potential of the electric field in its interelectrode gap satisfies the

complicated ordinary differential equation of the first order, derived from the charge conservation law and the Frenkel conductance, in terms of the equality between the capacitor plates voltage and the applied voltage.

From the analytical solution of this equation, which was obtained by us for the first time in [4] and satisfies such a condition, there follow the ohmic linearity of the volt-ampere characteristics in weak fields and its square dependence in the prebreakdown ones observed in highly heterogeneous fields. The derived solution describes mathematically and physically also more strictly (than the unipolar solutions in the case of diluted gases of Townsend's type) the transition (from linear to quadratic) part of the volt-ampere characteristics. Namely, we used another parameter instead of the empirical constant in the formula for the voltage of the crown discharge ignition. The parameter can be calculated for a given composition of the medium at hand. It was also measured, and one can find it in different manuals. Moreover, the author's theoretical high-voltage volt-ampere characteristics consider, as distinct from those of Townsend's, the influence of the temperature and charge composition of the medium molecule on the prebreakdown characteristics. We should also note that, in order to obtain an estimation of the volt-ampere characteristics, it is less advisable to use the constant of the voltage of the crown discharge ignition type for the investigated media than for diluted gases media, because of the difficulties of experimental registration of such kind of voltage in sufficiently dense, viscous and thermal conducting media.

In cases of the observed Ohm's law deviations, certain problems seem to be urgent, which are being solved in the present paper, namely, the nonstationary problems of calculation of such electrodynamic characteristics as the high-voltage conductance and ampere-time characteristics prior to the moment of the current reaching stationary values (the case of a source of applied high voltage alternating in time is not considered). The measurement results of such characteristics are described in [6]. Below, there will be obtained the analytical solution for electrohydrodynamic differential equations for such a nonstationary problem for the case of plane-parallel electrodes with an interelectrode gap  $d \ll \sqrt{S}$  (here,  $S$  is the surface area of a capacitor plate) and a numerical solution of the equations of electrodynamic approximation for a similar problem in the case of coaxial cylinder electrodes whose interelectrode gap is far less than their forming length  $l$ . From the calculations of the total electric currents according to the obtained solutions, it follows that, with the increase of the applied voltage (up to the prebreakdown value), their time changes reinforce up to their establishment, which agrees with the measurement results [6].

## THEORETICAL MODEL AND THE INITIAL EQUATIONS

For the volume concentrations of charges and, perhaps, for the impurities present in the case of weakly conducting media, the following inequalities should hold:

$$\begin{cases} n_{\pm} \ll n_a; \\ n_p \ll n_a. \end{cases} \quad (1)$$

The first of them (1) can be considered as one of the conditions of weak ionization or dissociation and, hence, the conductance of the examined media. Let us assume that the velocity of the volume ionization or dissociation in such media is a known concentration thermodynamic function of their neutral molecules and impurities, as well as the temperature and value of the electric field intensity. Besides, the charge recombination is supposed to be only double-particle:

$$W_1 = W_1(n_a, n_p, T, |\vec{E}|) = W_1(n_a, n_p, T, 0)f(|\vec{E}|); \quad (2)$$

$$\begin{cases} W_r = K_r n_+ n_-, \\ K_r = \frac{(b_+ + b_-)|e|}{\epsilon \epsilon_0}. \end{cases} \quad (3)$$

The expression used for  $K_r$  in the absence of the applied electric fields was derived by Langevin. Onsager grounded, by means of the physical kinetics, a weak influence of macroscopic electric fields up to the breakdown fields for the value of the ion coefficient of recombination determined according to (3), as well as their sufficiently strong influence on the value of the dissociation constant (the coefficient) of the weak liquid electrolytes studied by him. At the same time, for the coefficient of recombination, he also obtained the second of the equations (3) and, for the monotone increasing dependence of the constant of dissociation for the intensity module of the macroscopic electric field, the expression as an analytical and a zero Bessel function of the first order of an imaginary argument in the prebreakdown fields close to a nonanalytic zero exponent from the root of this module obtained by Frenkel from the equation of the Arrhenius type in [2]. Here is examined, in addition to the dissociation of the molecules with the ionic bonds, the media ionization with the electrons attaching the molecules with covalent bonds.

For the coefficient of diffusion of free charges, the Nernst-Townsend-Einstein correlation is

$$D_{\pm} = \frac{k_B T b_{\pm}}{|e|}. \quad (4)$$

In order to obtain the continuous scalar  $f$  function of the vector argument, which is introduced in (2) and



describes the dependence of the rate of the volume ionization increase or dissociation of the purified media molecules or dissociation of impurities contained in the contaminated media, upon the module of the electric field intensity, the Frenkel expression [2] should be used, as was done in the former works:

$$f(\vec{E}) = \exp\left(\beta|\vec{E}|^{\frac{1}{2}}\right); \quad \beta = \frac{|e|^{\frac{3}{2}}}{\sqrt{\pi\epsilon\epsilon_0}k_B T}. \quad (5)$$

Under these conditions, the equations of charge formation appear as follows:

$$\frac{\partial q}{\partial t} + (\vec{V}, \nabla q) - \frac{k_B T b}{|e|} \Delta q + (\vec{E}, \nabla \sigma) = -\frac{q\sigma}{\epsilon\epsilon_0}, \quad (6A)$$

$$\Delta \phi = -\frac{q}{\epsilon\epsilon_0},$$

$$\begin{aligned} \frac{\partial \sigma}{\partial t} + (\vec{V}, \nabla \sigma) + b^2 (\vec{E}, \nabla q) - \frac{k_B T b}{|e|} \Delta \sigma \\ - \frac{\sigma_0^2}{\epsilon\epsilon_0} \exp(\beta|\vec{E}|^{1/2}) + \frac{\sigma^2}{\epsilon\epsilon_0} = 0. \end{aligned} \quad (6B)$$

The system of the electrohydrodynamic equations (6) takes into account the diffusion transfer and convection for ionic components in a moving medium and the Poisson equation for the macroscopic electric field potential. This system should be mathematically enclosed by hydrodynamic (gasdynamic) equations for the total mixture under conditions (1). In this case, the differential equation for the mass conservation of the incompressible media under isothermal conditions is [5]

$$\operatorname{div} \vec{V} = 0. \quad (7)$$

To the equation of continuity (7), according to [5], there should be added the equation of pulse conservation in the case of incompressibility of the sufficiently viscous and dense media being studied without taking into account the equations of the energy conservation due to the weak Joule heating and the energy dissipation caused by the viscosity. Let us write the pulse equation as the equation of vorticity transfer [5] assuming that the vortex-free field of the electric polarization of the bonded charges only redistributes the pressure of the investigated medium:

$$\vec{\chi} = \operatorname{rot} \vec{V}, \quad (8)$$

$$\rho \frac{d\vec{\chi}}{dt} - \rho(\vec{\chi}, \nabla) \vec{V} - \rho \nu \Delta \vec{\chi} = [\nabla q, \vec{E}]. \quad (9)$$

The initial general conditions for the equations being obtained are the following ones:

$$q(t=0) = V(t=0) = 0; \quad \sigma(t=0) = \sigma_0. \quad (10)$$

The analytical solution for the steady distribution of the high voltage sphere potential in the above equations was obtained in [4] with the derived conditions of quasi-neutrality of the weakly conducting media in question. The equation will become

$$\phi(r) = \left(\frac{I}{4\pi\sigma_0}\right)^{\frac{1}{2}} \left[ \frac{8}{\beta} - \sqrt{\frac{\epsilon\epsilon_0}{\tau\sigma_0}} \left( |\vec{E}|^{\frac{1}{2}} + \frac{8}{\beta} \right) \right] \operatorname{sign}(\phi(r_0)). \quad (11)$$

$$|\vec{E}| \exp\left(\frac{\beta}{2} |\vec{E}|^{\frac{1}{2}}\right) = \frac{I}{4\pi\sigma_0 r^2}; \quad |\phi(r_0)| = U.$$

The solution in the case of a spherical high-voltage capacitor with a preset potential difference  $U$  between its plates is similar. The above-mentioned linearity of the volt-ampere characteristics of the weak fields and the square dependence of strongly heterogeneous prebreakdown ones result from (11) due to the corresponding limiting transitions. As to the distribution of the prebreakdown steady potential of spherical symmetry of (11), it differs greatly from that of the Laplace due to the space charge field influence. At the same time, in the case of a high-voltage plane capacitor, the electric field beyond the subelectrode boundary layers (where the electric charges quasi-neutrality is violated) remains homogeneous due to the charge conservation law. The heterogeneity of the spatial field distribution, which depends on the electrode boundary conditions, along with a space charge, forms when the prebreakdown voltage is applied only in such layers. For these cases, the results of various experiments in the plane capacitor field confirm the formula of calculation of the stationary (steady) prebreakdown volt-ampere characteristics under the conditions of the Frenkel quasi-neutrality of the investigated media, which theoretically forms from the corresponding integral of one-dimensional charge conservation differential equation. Then, in the case of the constant determination of such integration with respect to the electric field, this dependence is as follows:

$$\sigma_0 \frac{U}{d} \exp\left[\frac{\beta}{2} \left(\frac{U}{d}\right)^{\frac{1}{2}}\right] = \frac{I}{S}. \quad (12)$$

The nonstationary solutions are the analytical one for the case of a high-voltage plane capacitor and the numerical one for a cylindrical capacitor.

Regardless of the vortical characteristics of the prebreakdown (Fig. 1) flows of the investigated media within the interelectrode gap of the plane capacitor, a sufficiently simple particular solution satisfies the elec-

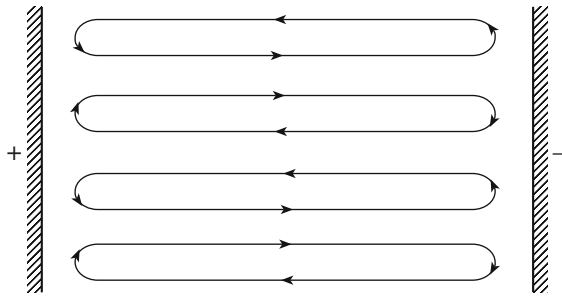


**Fig. 1.** The elementary scheme of the prebreakdown flows of weakly conducting media in the interelectrode gap of a plane capacitor.

trodynamic equations (6) and the initial conditions for these equations (10):

$$I = \sigma S U / d, \quad q = 0, \quad |\vec{E}| = U / d,$$

$$\sigma = \frac{\varepsilon \varepsilon_0 [\sigma_0 \tau + \varepsilon \varepsilon_0 - (\varepsilon \varepsilon_0 - \sigma_0 \tau) e^{-2t/x}]}{\tau [\sigma_0 \tau + \varepsilon \varepsilon_0 + (\varepsilon \varepsilon_0 - \sigma_0 \tau) e^{-2t/x}]}, \quad (13)$$

$$\tau = \frac{\varepsilon \varepsilon_0}{\sigma_0 \exp(0.5 \beta |\vec{E}|^{1/2})}.$$

The solutions of equations (6), which satisfy the electrochemical (at dissociation) or ionization boundary conditions across the capacitor plates, as well as the integral condition of independence of the potential difference between the capacitor plates upon the time, are close to the solution of (13) beyond the limits of the non-quasi-neutral boundary layers. Theoretically, it can be grounded by the described [9] methods of asymptotic boundary layer expansions on small parameters corresponding to the quasi-neutrality regimes with equation terms (6) having major space derivatives. The velocities of the prebreakdown flows of the weakly conducting medium can be small in this case and commensurable in comparison with the ionic drift rates in the electric field. The expressions for such criteria of similarity of the phenomena being described have been derived in [4, 7, and 8]. There have also been carried out estimations of the values of these parameters for the investigated prebreakdown regimes. At the same time, it has been shown that, for rather a wide class of media, the conditions of the electric (plasma) quasi-neutrality can also be achieved by the application of strong electric fields. Then, regardless of the characteristics of the cellular vortical electrohydrodynamic flows in the interelectrode gap (Fig. 1) and the boundary conditions across the electrodes, the ampere–time characteristics of the plane capacitor in the case of a source of direct in time high voltage can be calculated in accordance with (13) in a one-dimensional approximation. It follows from (13) that, with the increase of the applied voltage (prior to the breakdown), the time deviations of the prebreakdown currents also intensify before they attain

their stationary value, which agrees with the experimental results [6]. As follows from (13) and as should have been expected, for the conductivity according to the corresponding limit transition in time to infinity, we obtain the known Frenkel formula, in which the scalar continuous function  $f$ , which was introduced to (1) for the description of the velocity increase of the prebreakdown ionization (dissociation), is determined with respect to (5). It is from this formula that expression (12) for the stationary volt–ampere characteristics follows according to the charge conservation law. What is more, as follows from (13), at the transition from the weakly conducting media to the ideal dielectrics, this known formula fails to be applicable in practice, since, in this situation, the maxwellian time of the medium relaxation becomes sufficiently great.

As follows from the results of [7], under the quasi-neutrality conditions, formula (13) can also be obtained at various mobility of positive and negative charges. The analytical analogue of formula (13) in the case of cylindrical and spherical capacitors and, even more so, in the case of the two-dimensional configuration of high-voltage capacitors of the “over plane wire” type and the three-dimensional configuration of the “needle plane” type is impossible to be derived from equations (6) even regardless of the hydrodynamics influence upon the electrodynamic characteristics. In such cases, the calculation of the volt–ampere characteristics prior to the establishing of the stationary current value can be performed numerically using a simplified (for the exterior problems according to [9]) equation system (6) with the initial conditions (10). The analogue of formula (13) for strong heterogeneous electric fields of any complicated configuration can be obtained only under the condition of their Laplace characteristics preservation (note that the corresponding (13) general formula, in which  $f$  is not necessarily determined by (5), was derived in the previous paper [8]).

In order to obtain an elementary numerical solution in the case of a cylindrical capacitor and subsequent calculations of the corresponding ampere–time characteristics, the system of nonstationary one-dimensional electrodynamic equations [10] was used as obtained from the vectorial equations (6A) using, in the one-dimension cases, the Gauss equations for the intensity of the electric field of cylindrical symmetry instead of the Poisson equation for its potential:

$$\frac{\partial q}{\partial t} + \frac{E \partial \sigma}{\partial r} = -\frac{q \sigma}{\varepsilon \varepsilon_0},$$

$$\frac{\partial \sigma}{\partial t} = \frac{\sigma_0^2 \exp\left(\beta E^{\frac{1}{2}}\right) - \sigma^2}{\varepsilon \varepsilon_0}, \quad (14)$$

$$\frac{\partial E}{\partial r} + \frac{E}{r} = \frac{q}{\varepsilon \varepsilon_0}.$$

When obtaining the system of equations (14) in the left parts of (6A), there were preserved the terms describing the nonstationary changes of quasi-neutral conductance from the low-voltage to the high-voltage Frenkel one first obtained in [2] and the space charge formation from a zero to a stationary one. The excluded terms with the space major derivatives influence (at the quasi-neutrality criterion fulfillment) only the change of the required distributions of the electrodynamic characteristics in quasi-neutral, subelectrode boarding layers. For obtaining a numerical solution of the equation system (14), there were used the initial conditions (10) for the conductance and density of the space charge, as well as the Laplace condition of the electric field in the cylindrical capacitor at the initial moment of time:

$$E(r, 0) = \frac{U}{r \ln\left(\frac{r_1}{r_2}\right)}. \quad (15)$$

In (15),  $r_1$  and  $r_2$  are the inner and outer radii of coaxial cylinders. When selecting a step of an array on the radial coordinate, it was assumed that the thicknesses of the forming boarding layers of the quasi-neutrality violations were small in comparison with this step. Here, the calculation was performed from the inner cylinder to the outer one. The interior electrode served as the anode (with the change of its sign, the problem comes to the previous one: with the sign change of the field intensity and the space charge density). The last statement is grounded numerically in [11], where, with the use of the extensions of equations of type (14) for the nonisothermic case, there has been studied a similar nonstationary problem of the electric field in the vicinity of a dispersed spherical particle getting cool. Apart from that nonisothermic problem, when solving the isothermic one described in the present paper, it seems impossible to use a nonstationary integral of the equation of the charge conservation at room temperatures  $T$

$$\varepsilon \varepsilon_0 \frac{\partial E}{\partial t} + \sigma E = \frac{I}{2\pi r l} \quad (16)$$

for the reduction of the equation system order (14). For the calculations whose results are presented below, integral (16) was used for the control of the numerical calculation of the difference equations obtained from the differential equations (14) in a nondimensional form. In addition, with respect to (16), there was determined the required dependence of the current upon the time prior to the currents reaching their stationary value. A transition to the dimensionless equations was

performed by following the transformation of the required and initial values:

$$\begin{aligned} \tilde{t} &= \frac{t}{\tau}, \quad \tilde{E} = \frac{Ed}{U}, \quad \tilde{q} = \frac{qd^2}{\varepsilon \varepsilon_0 U}, \\ \tilde{\beta} &= \beta \left(\frac{U}{d}\right)^{1/2}, \quad \tilde{r} = \frac{r}{d}, \\ \tilde{\sigma} &= \frac{\sigma}{\sigma_0 \exp\left(\frac{\tilde{\beta}}{2}\right)}. \end{aligned} \quad (17)$$

Then, as obtained from (14), the system of equations transformed into the dimensionless form is as follows:

$$\begin{aligned} \frac{\partial \tilde{E}}{\partial \tilde{r}} + \frac{\tilde{E}}{\tilde{r}} &= \tilde{q}, \\ \frac{\partial \tilde{q}}{\partial \tilde{t}} + \frac{\tilde{E} \partial \tilde{\sigma}}{\partial \tilde{r}} &= -\tilde{q} \tilde{\sigma}, \\ \frac{\partial \tilde{\sigma}}{\partial \tilde{t}} &= \exp\{\tilde{\beta}(\sqrt{\tilde{E}} - 1)\} - \tilde{\sigma}^2. \end{aligned} \quad (18)$$

The dimensionless initial conditions will resemble

$$\begin{aligned} \tilde{\sigma}(\tilde{r}, 0) &= \exp\left(\frac{\tilde{\beta}}{2}\right), \\ \tilde{q}(\tilde{r}, 0) &= 0, \\ \tilde{E}(\tilde{r}, 0) &= \frac{1}{\tilde{r} \ln\left(\frac{r_1}{r_2}\right)}. \end{aligned} \quad (19)$$

More over, in order to obtain the ampere–time characteristics of the high voltage cylindrical capacitor filled with the investigated medium, according to the numerical solution of equation (18) with the initial conditions (19), integral (16) was pretransformed into a dimensionless form that appears as follows:

$$\begin{aligned} \frac{\partial \tilde{E}}{\partial \tilde{t}} + \tilde{\sigma} \tilde{E} &= \frac{\tilde{I}}{\tilde{r}}, \\ \tilde{I} &= \frac{I}{2\pi l \sigma_0 U \exp\left(\frac{\tilde{\beta}}{2}\right)}. \end{aligned} \quad (20)$$

From the similar problem of a plane capacitor and its analytical solution (13), it follows that the establishing occurs at  $\tilde{t} \approx 1$ . Therefore, for obtaining the required numerical solution, there was selected a time step of  $\Delta \tilde{t} = 0.02$ . The stationary solution was achieved approximately within 50 steps. In order to carry out the

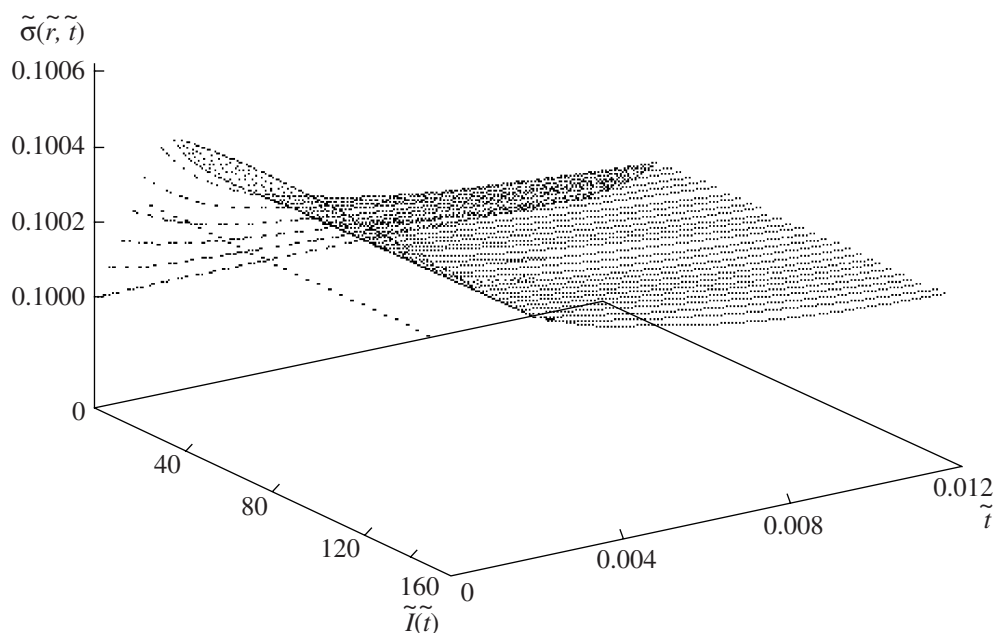


**Fig. 2.** The space–time distribution of the prebreakdown conductance of the weakly conducting medium in the interelectrode gap of a cylindrical capacitor (see the text for comment).

specific numerical calculations along the radial coordinate, there was selected a similar high-voltage capacitor 5 cm long, the same as for the previous calculations [12] of its volt–ampere characteristics after their establishment, namely, with a 1.2 mm internal radius and a 2 mm external one ( $d = r_2 - r_1$ ). Similar to as in (12) were chosen the dielectric media permeability (2. 24) and its low voltage conductance ( $10^{-11} \frac{\text{S}}{\text{m}}$ ). A refined trans-

former oil, for instance, can be considered to be such a low conductance and dielectric permeability media.

The temperature, due to weak Joule heating, was assumed to be room temperature. The voltage applied to the capacitor equaled 10 kV. In calculations according to the space coordinate, the step equaled 0.1. The differential equations (18) were replaced by the corresponding difference ones. It should be noted that, in the previously [3, 8] described physical mechanisms of a space charge formation in a high-voltage field of cylindrical symmetry, such difference equations and their nonstationary solutions for the first steps with respect to  $t$  were already derived and, therefore, are not presented here. In accordance with such difference equations, at each following time step, first, were calculated the volume distribution of the conductance; next, the density of the space volume; and, after that, the intensity distribution of the electric field in the interelectrode gap. They were calculated on the basis of the Gauss equation. After the calculations were performed at each time step, according to the difference similarity of the integral (20), there were calculated the time changes of the

total current up to its establishing. At each step, there were recalculated the corresponding matrix arrays of the space–time distributions of the required variables. Whereupon they were substituted into the difference similarity of the integral (20). Note that the calculation results for the first steps in time have already been described in [3, 8], where there is described the difference of  $q$  and  $E$  resulting for the initial Laplace high-voltage fields of the plane and cylindrical capacitors. In addition, in [3, 8], the distinction of the electrodynamic characteristics in the case of the homogeneity of the prebreakdown applied field in the case of its strong heterogeneity was analyzed in [8] at stationary  $q$  and  $E$ . A distinction of the flows structure in a strong heterogeneous applied field from the cellular flows in a plane capacitor was also described earlier. Therefore, in the present paper, on the basis of the obtained analytical and numerical solutions, we shall describe the similarity of the desired characteristics for the cases of homogeneous and strongly heterogeneous applied fields. It consists, for both cases, in the rather quick time evolution of a low voltage conductance to a steady high voltage. This follows both from formula (13), referring to  $\sigma$  in a plane capacitor, and from the diagram in Fig. 2 in the case of a cylindrical one. The diagram in Fig. 2 presents a space–time change of  $\sigma$  graphed according to the results of the numerical calculations described above. Note that the counting stability of the difference scheme presented in this paper was not examined. However, this can be done by analogy with the stability analyses [14] for close one-dimensional problems. The change of  $\tilde{\sigma}$  is stipulated by the affect of the prebreak-



down field on the velocity of the dissociation (ionization) reaction of the investigated media. In this situation, for the initial data with which the numerical calculations were carried out (the scheme of which is given above), a sufficiently fast establishing of the conductance occurs within a period of time close to 1 s. The similar times of the conductance establishing also result from the analytical solution of (13). What is more, this similarity concerns the ampere–time characteristics as well.

The diagram in Fig. 3 displays the time evolution of the prebreakdown current up to the establishment of a stationary current value taking into consideration the results of the numerical calculation of equations (18) and their integral (20). This diagram is geometrically close to the curves of the prebreakdown nonstationary currents of the plane capacitor, which is graphed in accordance with formula (13) and presented in [13]. Such diagrams prove the monotony of the prebreakdown current increase from the time up to its establishing starting with the high voltage supply at the electrodes from the direct current source. In this case, the media becomes rather highly electrified. The degree of its charging can be determined with respect to the established current. By analogy with (11) and (12), the distribution of the field intensity of cylindrical symmetry follows from the formula based on the charge conservation law:

$$|\vec{E}| \exp\left(\frac{\beta}{2} |\vec{E}|^2\right) = \frac{I}{2\pi\sigma_0 l r}, \quad (21)$$

where  $I$  is a stationary current.

The integral charge  $Q$  outside the subelectrode layers of quasi-neutrality violation is

$$Q = \int_V q dV,$$

where  $q$  is defined from the last equation (14), and (21) is determined analytically. Here, the result is

$$Q = \tau I \left[ \exp\left(\frac{-\beta\sqrt{E_2}}{2}\right) - \exp\left(\frac{-\beta\sqrt{E_1}}{2}\right) \right]; \quad (22)$$

$$E_1 = E(r_1), \quad E_2 = E(r_2).$$

Then, with respect to (23) for the data with which there were performed the described numerical calculations at the current establishment, it turns out that  $Q \approx 10^{-9}$  holds. This theoretical result shows a high degree of charging in high-voltage devices, which is confirmed experimentally. Therefore, in the design and construction of such devices for manufacturing applications,

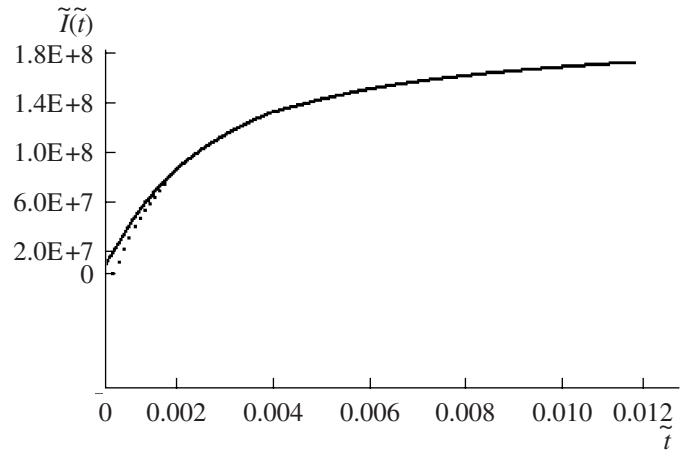


**Fig. 3.** The prebreakdown ampere–time characteristics of a cylindrical capacitor filled with a weakly conducting medium (see the text for comment).

certain additional facilities should be provided for neutralizing such kinds of charge or their earthing.

#### ACKNOWLEDGMENTS

The author thanks B.A. Shutov for his assistance in carrying out the numerical calculations for a cylindrical capacitor.

#### MAIN DESIGNATIONS

$\sigma_0$  – low voltage conductivity of a medium;

$U$  – applied electrical voltage;

$d$  – interelectrode gap;

$e$  – proton or ion charge;

$k_B$  – Boltzmann constant;

$D$  – diffusion coefficient;

$b$  – mobility coefficient;

$q$  – charge volume density;

$V$  – media motion velocity;

$n$  – concentration;

$E$  – intensity of the electric field;

$S$  – charge surface area;

$r$  – radial coordinate;

$t$  – time;

$\tau$  – charge relaxation time;

$\chi$  – vorticity;

$\varepsilon$  – dielectrical permeability;

$I$  – electric current power;

$T$  – absolute temperature;

$f$  – a function of the scalar and vector argument;

$W$  – volume velocity of the charge and neutrals formation.

## REFERENCES

1. Poole, H.H., On the Dielectric Constant and Electrical Conductivity of Mica in Intense Field, *Phil. Mag.*, 1916, S. 6, vol. 2, no. 187, pp. 112–129.
2. Frenkel, Ya.I., On the Theory of the Electrical Breakdown in Dielectrics and Electron Semiconductors, *Zh. Eksp. Teor. Fiz.*, 1938, vol. 8, issue 12, pp. 1291–2001.
3. Apfel'baum, M.S., The Equations of Equilibrium Ionization of Combustion Products in the Electric Field, *Fiz. Goren. Vzryva*, 1988, no. 2, pp. 60–65.
4. Apfel'baum, M.S., On a Calculation Scheme of Electrohydrodynamic Flows, *Elektrokhimiya*, 1986, issue 11, pp. 1463–1471.
5. Landau, L.D. and Lifshits, E.M., *Teoreticheskaya fizika. t. 6. Gidromekhanika* (Theoretical Physics. vol. 6. Hydromechanics), Moscow: 1989.
6. Dikarev, B., Karasev, G., Romanets, R., and Shimon, N., Modeling and Experimental Research of the Non-Stationary Processes of Conduction and Space Charge Accumulation in Dielectric Liquids, *Proc. 13th Int. Conf. Dielectric Liquids*, Nara, 1999, pp. 33–36.
7. Apfel'baum, M.S. and Kozyrenko, V.E., Physical Modelling and the Calculation of Electrohydrodynamic Flows, *Elektrokhimiya*, 1991, issue 7, pp. 855–863.
8. Apfel'baum, M.S., Ionization and Flow of Weakly Conducting Liquid in Hererogeneous Electric Field, *Elektron. Obrab. Mater.*, 1988, no. 1, pp. 60–65.
9. Naife, A.Kh., *Vvedenie v metody vozmuschenii* (Introduction into the Methods of Perturbations), Moscow: 1984.
10. Ostroumov, G.A., *Vzaimodeistvie elektricheskikh i gidrodinamicheskikh polei* (Interaction of the Electric and Hydrodynamic Fields), Moscow: 1979.
11. Apfel'baum, M.S. and Apfel'baum, E.M., On Electric Field Distribution in the Vicinity of Particles in a Weakly Ionized Disperse Medium, *Chem. Phys. Report*, 2000, vol. 18, pp. 2313–2328.
12. Apfel'baum, M.S., One-Dimensional Stationary Problems of Calculation of Pre-Breakdown Voltampere Characteristics in Weakly Ionized Media, *Elektron. Obrab. Mater.*, 2005, no. 2, pp. 50–53.
13. Apfel'baum, M.S., One-Dimensional Problems of Calculation of Pre-Breakdown Ampere-Time Characteristics of Weakly Ionized Media, *Elektron. Obrab. Mater.*, 2006, no. 1, pp. 37–43.
14. Marchuk, G.I., *Metody vychislitel'noi matematiki* (Methods of Numerical Mathematics), Moscow: 1970.

## ELECTRICAL PROCESSES IN ENGINEERING AND CHEMISTRY

# Spectrophotometric Study of Condensates Obtained at Nonequilibrium Evaporation of a Solution under the Action of Glow Discharge

A. V. Khlyustova<sup>a</sup>, O. A. Vasil'ev<sup>b</sup>, N. A. Sirotkin<sup>b</sup>,  
Yu. V. Manakin<sup>b</sup>, and A. I. Maksimov<sup>a</sup>

<sup>a</sup> Institute of Solution Chemistry, Russia Academy of Sciences, ul. Akademicheskaya 1, Ivanovo, 153045 Russia  
e-mail: kav@isc-ras.ru

<sup>b</sup> Ivanovo State University of Chemistry and Technology, pr. F. Engel'sa 7, Ivanovo, 153000 Russia

Received November 16, 2007

**Abstract**—Spectrophotometric studies of colored solutions of inorganic salts before and after glow discharge action and condensates obtained at nonequilibrium evaporation are presented in this paper. The experimental results show that the absorption curves of the condensates differ from the absorption curves of the initial and treated solutions. These absorption spectra of the nonequilibrium condensates differ from the absorption spectrum of the condensate obtained at equilibrium (thermal) evaporation.

**DOI:** 10.3103/S106837550803006X

With the glow discharge burning with the electrolyte cathode, there is observed the transfer of both solvent and solutes into the gas phase. The investigation of the kinetics of such nonequilibrium evaporation of a solvent was conducted previously and the accumulation in the condensate of ions of potassium, chlorine, nitrite, and nitrate carried from the solution was proved experimentally [1, 2].

The study of the solute transfer by comparison of the absorption spectra of the condensate and the initial solution is the purpose of this work.

The cell working volume was 230 ml. Copper wire served as the cathode material, and copper and niobium rods were the anodes. Colored solutions of  $\text{NiSO}_4$ ,  $\text{NiCl}_2$ ,  $\text{Ni}(\text{NO}_3)_2$ ,  $\text{Co}(\text{NO}_3)_2$ , and  $\text{FeCl}_3$  were treated during the experiments. The solution concentration varied in the range from 0.1 to 1.0 mol/l. The discharge current changed from 15 to 35 mA. The interelectrode space was 1–1.5 mm. In the course of the experiment, the condensate was collected and analyzed spectrophotometrically as well as by the methods of qualitative analysis to test for the presence of ions.

### EXPERIMENTAL PROCEDURE

The installation of the electric circuit is presented in Fig. 1. To carry out the research work, there was manufactured a cell whose diagram is shown in Fig. 2.

The spectrophotometric investigation was carried out with the help of SPECOLL-11 spectrophotometers with a wave length range of 330–750 nm and SF-103 spectrophotometers with a range of 190–1100 nm.

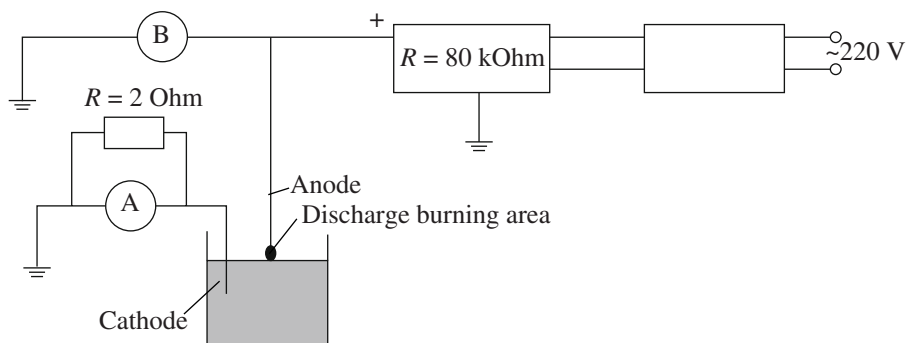


**Fig. 1.** The electric circuit of the working installation for investigation of transfer processes using photometric methods.

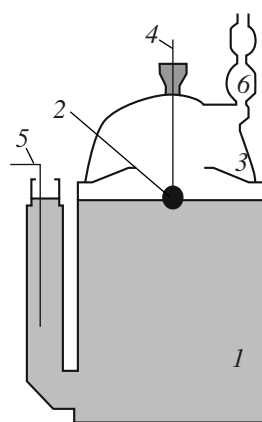


**Fig. 2.** The working cell view for investigation of transfer processes. 1—solution; 2—discharge burning area; 3—place of condensate collecting; 4—anode; 5—metal cathode; 6—reverse cooler.

## RESULTS AND DISCUSSION

The results of the experiments using the qualitative analysis of the condensate for cations and anions show that the glow discharge action on the electrolyte solu-

The qualitative analysis data on the condensate collected in the course of the nonequilibrium evaporation under the action of glow discharge

The initial solution, concentration, discharge current, treatment time	Qualitative response to the respective ion
FeCl <sub>3</sub> 0.2 mol/l, <i>I</i> = 25 mA, <i>t</i> = 40 min	$\text{Fe}^{3+} + n\text{SCN}^- \longrightarrow \text{Fe}(\text{SCN})_3 \downarrow$ red sediment
Co(NO <sub>3</sub> ) <sub>2</sub> 0.2 mol/l, <i>I</i> = 20 mA, <i>t</i> = 45 min	$\text{Co}^{2+} + 4\text{SCN}^- \longrightarrow [\text{Co}(\text{SCN})_4]^{2-} \downarrow$ blue coloring
BaCl <sub>2</sub> 1 mol/l, <i>I</i> = 25 mA, <i>t</i> = 40 min	$\text{Ba}^{2+} + \text{SO}_4^{2-} \longrightarrow \text{BaSO}_4 \downarrow$ white sediment
NiCl <sub>2</sub> 0.5 mol/l, <i>I</i> = 25 mA, <i>t</i> = 40 min	$\text{Ni}^{2+} + (\text{CH}_3\text{CNOH})_2 \longrightarrow \text{Ni}(\text{CH}_3\text{CNO})_2 + 2\text{H}^+$ blue-violet coloring
BaCl <sub>2</sub> 1 mol/l, NiCl <sub>2</sub> 0.5 mol/l, <i>I</i> = 25 mA, <i>t</i> = 40 min	$\text{Cl}^- + \text{Ag}^+ \longrightarrow \text{AgCl} \downarrow$ white sediment

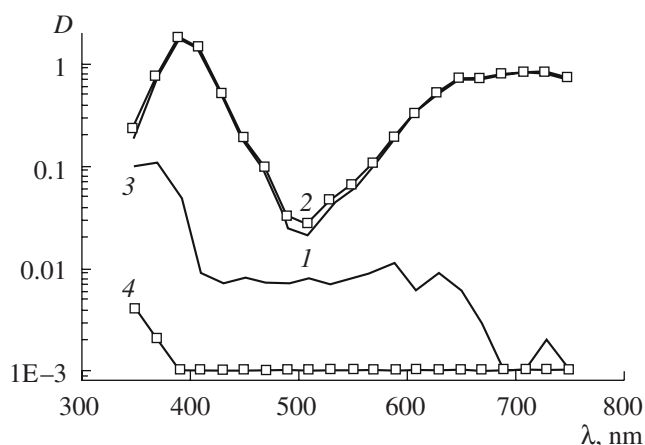


**Fig. 3.** Absorption spectra of the untreated (curve 1), treated (curve 2), and nonequilibrium (curve 3) condensates, as well as the condensate at the equilibrium (thermal) evaporation (curve 4) of the solution of NiCl with the starting concentration 0.5 mol/l. The discharge current is 20 mA.

tions causes the accumulation of anions and cations of the nonvolatile solutes in the condensate (see the table).

The glow discharge influence on the inorganic salt solution absorption spectrum is demonstrated with nickel chloride (Fig. 3). As is seen from the presented data, the spectra of the initial solution and the solution subjected to the discharge action differ insignificantly. At the same time, the absorption spectrum of the condensate obtained through nonequilibrium evaporation differs fundamentally both from the spectrum of the condensate obtained through equilibrium evaporation and from the spectrum of the initial solution. It is evident that the differences of the spectra of the initial solution and the nonequilibrium condensate can't be explained only by the small concentration of the solute in the condensate. Similar relations are observed at the study of other colored solutions of salts.

It should be noted that the condensate collected at the nonequilibrium evaporation always has a more acid medium than the initial solution. Thus, for example, the initial solution of NiCl<sub>2</sub> has a starting value of pH 5.5 and the condensate has pH 1.5. Probably, the main contribution to the growth of the condensate acidity is made by the nitrogen oxides generation in the plasma zone. It is supposed that this fact is the reason for the significant difference of the condensate absorption spectrum from the initial solution spectrum.

However, the direct adding of the nitric acid into the solution doesn't cause such changes of the spectrum. At the same time, the glow discharge action on the nitric acid solution is the cause of the accumulation of its condensate, the absorption spectrum of which in the short-wave band differs greatly from the initial acid spectrum (Fig. 4). Hence, the change of the condensate absorp-



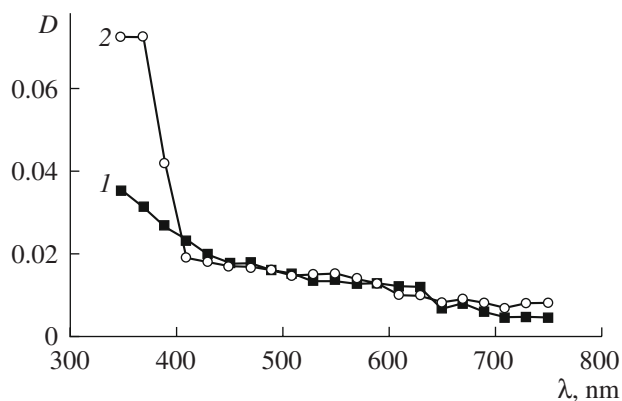


**Fig. 4.** Absorption spectra of the nitric acid before the glow discharge action (curve 1) and of the condensate (curve 2) generated in the process of the discharge burning. The value of the solution pH before the action and in the condensate is 1.5. The discharge current is 25 mA.

tion spectra observed at the nonequilibrium evaporation of both salt solutions and the acid is the difference in the structural states of the aqueous solutions in this process resulting in the variation of the hydration characteristics of the ions and of their spectra.

## CONCLUSIONS

In the course of the nonequilibrium evaporation of aqueous solutions of electrolytes under the action of atmospheric pressure glow discharge, there occurs the transfer of the solvent (water) and nonvolatile solutes into the gas phase and the following condensation with the condensate state differing from the initial solution because of the solvent structural changes initiated by the discharge. It appears as qualitative variation of the absorption spectra of the colored inorganic salt solutions.

## ACKNOWLEDGMENTS

This work was performed at the base of Ivanovo State University of Chemical Technology.

## REFERENCES

1. Khlyustova, A.V. and Maksimov, A.I., Transfer of Solution Components into Plasma Zone under the Conditions of Glow Discharge at Atmospheric Pressure with Electrolyte Cathode, *Electron. Obrab. Mater.*, 2003, no. 1, pp. 44–47.
2. Khlyustova, A.V., Dydykin, M.G., Maksimov, A.I. and Poyakov, M.S., Investigation of Solvent Transfer Kinetics by Weight Method under Atmospheric Pressure Glow Discharge Conditions, *Electron. Obrab. Mater.*, 2007, no. 5, pp. 48–51.

---

ELECTRICAL PROCESSES  
IN ENGINEERING AND CHEMISTRY

---

## Temperature Influence on the Equilibrium and Kinetics of Fluoride-Ion Adsorption by Heat-Treated Al Oxyhydrates

V. I. Zelentsov, T. Ya. Datsko, and E. E. Dvornikova

*Institute of Applied Physics, Academy of Sciences of Moldova, ul. Academiei 5, Chisinau, MD–2028 Republic of Moldova*

*e-mail: vzelen@yandex.ru, tatianadatsko@phys.asm.md*

Received December 20, 2007; in final form, March 26, 2008

**Abstract**—The effect of temperature on the fluoride adsorption by heat-treated samples of aluminum alloy AMG-6 electrochemical machining products has been studied. Kinetic curves and adsorption isotherms at solution temperatures of 20, 30, and 40°C have been received, and the adsorption rate constants, diffusion coefficients, and the values of the activation energy have been determined. The obtained  $E_a$  value corresponds to values of the activation energy characteristic of ion exchange processes controlled by internal diffusion. Thermodynamic functions of the adsorption process  $\Delta F_0$ ,  $\Delta H_0$ , and  $\Delta S_0$  have been calculated. The differential free molar energy changes, the isosteric heat, and the entropy of the fluorine adsorption have been analyzed versus the filling degree of the sample surface with fluorine ions. The absence of the process rate dependence on the mixing rates, as well as the character of the dependences of  $F$  (equilibrium degree reaching, %) on the  $\sqrt{t}$  demonstrates that the process under consideration is controlled by an internal diffusion step. The mechanism of fluorine ion fixation on the modified surface of aluminum oxyhydrates has been discussed.

**DOI:** 10.3103/S1068375508030071

### INTRODUCTION

The high selectivity of aluminum oxyhydroxides with respect to fluorine is well known [1–4]. It is always desirable to find a sorbent characterized by both the highest adsorption capacity and kinetic rate. Numerous studies are concerned with solution of the problem [5–7]. However, application of oxyhydrate sorbents for removal of fluorine ions requires intimate knowledge of the adsorption mechanisms. The equilibrium and kinetics are two aspects of the adsorption process. Important information may be obtained by studying the temperature dependences of the adsorption equilibrium constant and the adsorption process rate [8–12]. Therefore, we have studied the influence of the solution temperature on the equilibrium and kinetics of fluorine ion adsorption by heat-treated products of dimensional electrochemical machining (DECM) [13] of the aluminum alloy AMG-6. Earlier, we studied the pore structure of these samples [14]. For them, the adsorption isotherms were measured, the exchange constants and Langmuir equation parameters were calculated, and an hypothesis of the adsorption mechanism was given [15]. The aim of the present paper was to study, in the course of the experiments on the adsorption, the solution temperature influence on the fluorine adsorption rate and the sorbent adsorption capacity with respect to fluorine, as well as their dependences on the nature of the sorbent surface (the temperature of the heat treatment of AMG residues).

### EXPERIMENTAL AND RESULTS AND DISCUSSION

Residues obtained as the result of DECM of the aluminum alloy AMG-6 were subjected to treatment according to [14] (hereinafter, they are denoted as AMG-100, AMG-200, AMG-400, and AMG-600). For the determination of the stage responsible for the process rate, the influence of the solution stirring rate on the adsorption process rate was studied; the kinetic curves were plotted at three solution temperatures of 293, 303, and 313 K (Fig. 1), which were the basis for the calculation of the rate constants, the diffusion coefficients, and the adsorption activation energies. The curves have the form characteristic of strong interaction of an adsorbent and an adsorbate. Initially, the adsorption value is practically proportional to time, since the adsorbent surface is free from adsorptive. After equilibration, the adsorption becomes time independent and the corresponding parts of the curves are almost parallel to the time axis.

The kinetic analysis of the adsorption interaction of fluoride ions with the samples heat-treated at different temperatures has shown that the adsorption process may be described by the pseudo-first-order chemical equation, since one of the reagents is the solid phase.

The first-order adsorption rate equation usually has the form [16]

$$da/dt = k(a_e - a_t), \quad (1)$$

where  $a_e$  is the amount of adsorbed substance corresponding to the adsorption equilibrium under the given

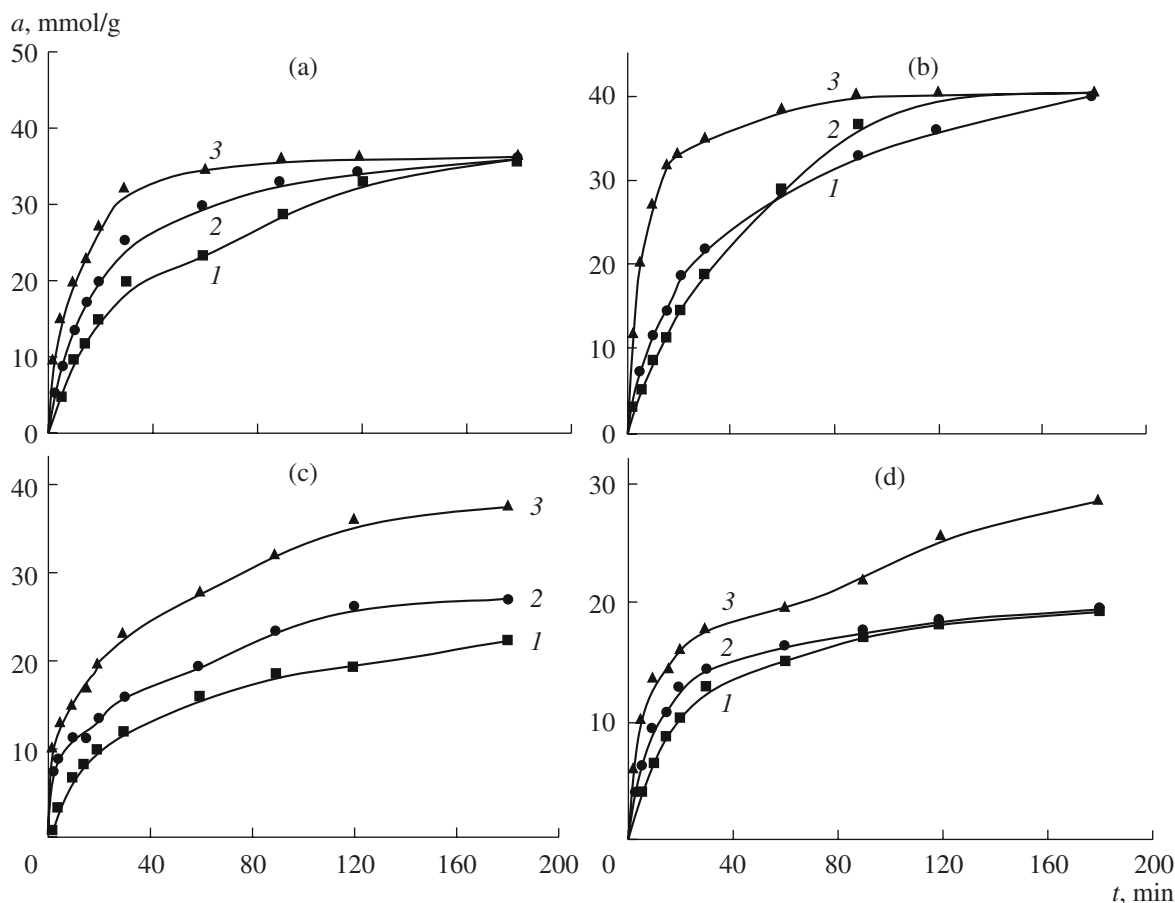


**Fig. 1.** Kinetics of fluoride-ion adsorption by the samples of AMG-100 (a), AMG-200 (b), AMG-400 (c), and AMG-600 (d) at the following solution temperatures, °C: (1) 20, (2) 30, and (3) 40.

conditions,  $a_t$  is the amount of the substance adsorbed by the time  $t$ , and  $k$  is the equation constant.

The physical meaning of the constant  $k$  of this equation is quite clear: as the system approaches equilibrium (that is, at higher surface saturation characterized by the factor  $(a_e - a_t)$ ), the adsorption rate is lower. The constant  $k$  depends on the adsorbing surface dimension and on the adsorbate diffusion coefficient.

The influence of the solution temperature on the adsorption rate is of interest: as the former grows, the latter increases, since heating always contributes to acceleration of equilibration in the system. Values of the rate constants for fluoride-ion adsorption by heat-treated residue samples obtained at different temperatures of the solution (20, 30, and 40°C) were used for the calculation of the adsorption activation energy  $E_a$  (kJ/mol) according to the known Arrhenius equation

$$k = Be^{\frac{E_a}{RT}}. \quad (2)$$

Studies of the dependence of the fluoride adsorption by the samples on the stirring rate have shown that the latter practically does not influence the former. This is evidence of the fact that the external-diffusion factor

does not play a significant role in the studied process and the latter appears to be determined by the internal diffusion of ions in the sorbent grains.

The values of the effective diffusion coefficients were calculated by the modified Fick equation [17]

$$\ln[1 - F(t)^2] = -\frac{\pi^2 D^2}{r^2} t, \quad (3)$$

where  $F(t)$  is the equilibrium degree for the time  $t$ ,  $D$  is the diffusion coefficient ( $\text{cm}^2/\text{s}$ ), and  $r$  is the radius of the particles (cm) under the assumption of their spherical form.

The values of  $F(t)$  were obtained from their equilibrium degree vs  $\sqrt{t}$  curve (Fig. 2). The rectilinear behavior of the dependence shows that the sorption process is controlled mainly by the internal diffusion.

The diffusion coefficients were determined from the slope of the curves plotted by equation (3) (Fig. 3). From the diffusion coefficient dependence on  $1/T$ , the apparent activation energy of the adsorption in the pores (the diffusion activation energy)  $E_a^D$  (kJ/mol) was calculated. The values of the calculated rate constants, the diffusion coefficients, the activation energies of the

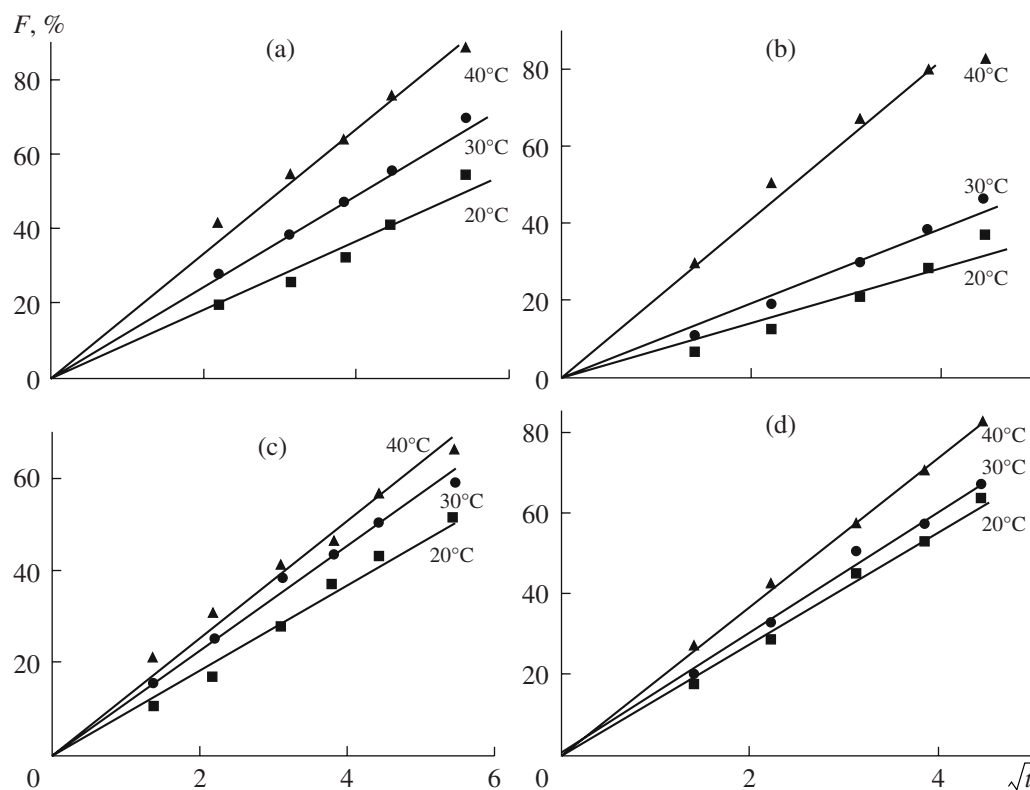


**Fig. 2.** Dependence of  $F$  on the  $\sqrt{t}$  for different solution temperatures of the samples AMG-100 (a), AMG-200 (b), AMG-400 (c), and AMG-600 (d).

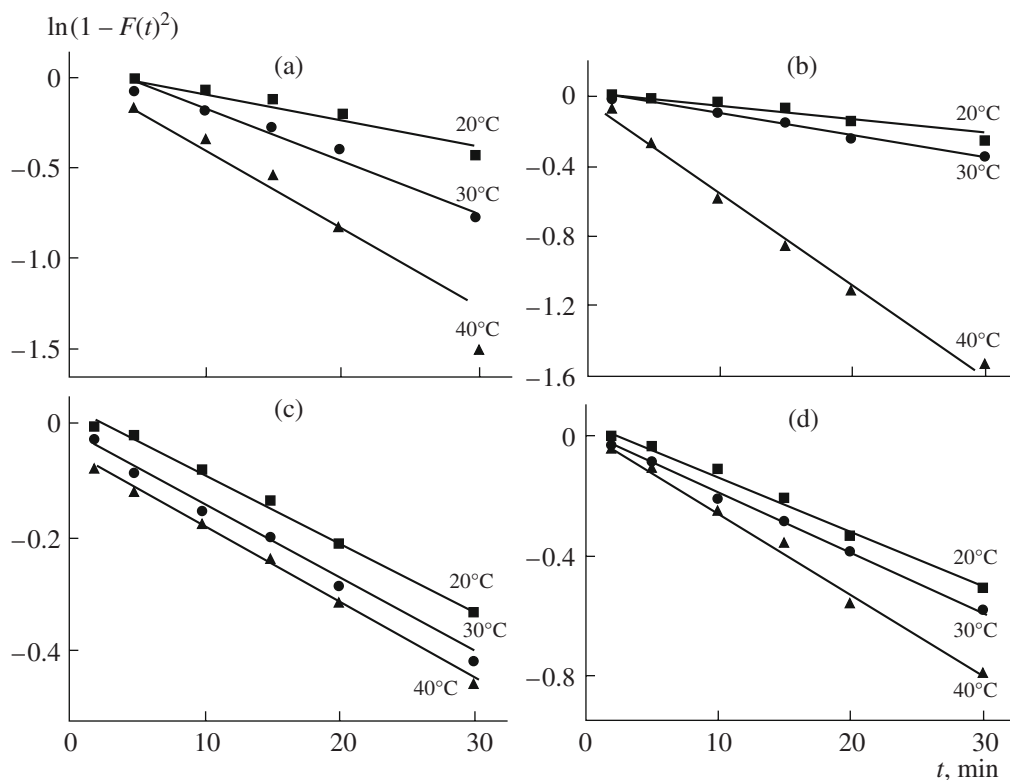


**Fig. 3.** Dependence  $\ln(1 - F(t)^2)$  on the time for different solution temperatures of the samples AMG-100 (a), AMG-200 (b), AMG-400 (c), and AMG-600 (d).



**Table 1.** The rate constants  $k$ , the diffusion coefficients  $D$ , the activation energy  $E_a$  of the adsorption process, the diffusion activation energy  $E_a^D$ , and the adsorption capacity  $a_m$  of the heat-treated products of DECM of the AMG-6 alloy with respect to fluoride ions

Sample	Solution temperature, K	$k \times 10^4$ , l/(mol s)	$D \times 10^8$ , cm <sup>2</sup> /s	$E_a$ , kJ/mol	$E_a^D$ , kJ/mol	$a_m$ , mM/g
AGM-100	293	3.00	0.282	41.42	26.8	35.96
	303	4.67	0.405			–
	313	9.33	0.570			36.4
AGM-200	293	2.73	0.096	61.9	44.1	36.0
	303	3.45	0.139			–
	313	3.47	0.302			40.0
AGM-400	293	3.00	0.123	32.3	20.4	26.8
	303	4.67	0.152			–
	313	6.17	0.166			34.8
AGM-600	293	4.00	0.153	19.2	11.2	19.2
	303	4.52	0.177			–
	313	5.06	0.206			28.9

adsorption and diffusion, and the adsorption capacity of the studied samples are presented in Table 1.

As has been noted, the rate constants  $k$  for all the samples increase as the solution temperature grows (this being obligate for chemical reactions). The values of the diffusion coefficients are of the same order as for metal ion sorption on the aluminum oxide surface [18]. In all the cases, the diffusion coefficients and the adsorption capacity of the samples increase as the solution temperature grows. This may be attributed to the fact that the temperature growth causes an increase of the kinetic energy of motion of the fluorine ions and their fastest forwarding to the adsorption centers—hydrated aluminum ions on the surface. The chemical interaction between the fluorine ions and the surface centers can increase as the solution temperature grows, since electrostatic interactions can contribute.

The solution temperature increase leads to variation of the sorbent surface electric properties: due to the PZC (point of zero charge) shift, the electrostatic repulsion of the fluorine ions and the potential determining hydroxyl ions decreases; in addition, at the temperature growth, the EDL (electrical double layer) diffusion part compression occurs [19]. The values of the diffusion coefficients inside the particles increase most obviously when the solution temperature is above 30°C; this shows that the resistance of fluorine diffusion inward the sorbent grains weakens at the temperature growth. The highest values of the diffusion coefficients are characteristic of the sample AMG-100 ( $0.28\text{--}0.57 \times 10^{-8}$  cm<sup>2</sup>/s). This may be due to the fact that the mentioned sample is characterized by the greatest effective diameter of the pores calculated from the adsorption data (70 Å) [14]. The diffusion coefficients of the other samples vary according to their values of the effective

pore diameters. The values of the diffusion coefficient for the sample AMG-200 at 20°C is lower than for the other samples (since  $d_{\text{eff}} = 52$  Å); at the solution temperature above 30°C, with increasing mobility of fluorine ions, the diffusion coefficients increases. It appears that, under these conditions, the pore diameter stops being the determining factor.

The adsorption capacity of the heat-treated samples with respect to fluorine increases at the solution temperature growth from 20 to 40°C (Table 1); this shows that the process of fluorine adsorption by the aluminum oxyhydrate samples is endothermal in nature. The  $E_a^D$  values decrease in the series AMG-100 > AMG-400 > AMG-600. The diffusion activation energy of the sample AMG-200 is the highest. This means that fluorine ions require more energy in order to diffuse inward the sample of AMG-200 than inward the samples of AMG-100, AMG-400, and AMG-600. This behavior is in good agreement with the behavior assumed from the values of the diffusion coefficients inside the particles.

However, the values of the adsorption activation energy  $E_a$ , varying in a symbate way with respect to the values of the maximum adsorption capacity of the samples and characterizing the adsorption process nature, reflect the chemical nature of the adsorption for not all the samples. Thus, for the sample AMG-600, the activation energy is 19.2 kJ/mol, this being more characteristic of the physical adsorption.

The fluoride-ion adsorption isotherms were measured from solutions with a concentration of the F<sup>−</sup> ion from  $10^{-4}$  to  $5 \times 10^{-1}$  mol/l at the solution temperatures of 293, 303, and 313 K [15].

The equilibrium states at the adsorption of components from the solution are expressed by the adsorption

**Table 2.** Dependence of the heat of fluoride-ion adsorption by adsorbent samples on the surface population  $\theta$ 

Sample	$a$ , mmol/g	$C_p$ , mmol/l	$\theta$	$C_p$ , mmol/l	$\theta$	$\bar{Q}$ , kJ/mol
AMG-100	293 K			313 K		
	28	17	0.77	2	0.77	81.33
	30	36	0.82	4	0.82	82.16
	32	58	0.88	9	0.88	70.79
	34	82	0.93	18	0.93	57.66
	$a_m = 36.4$ mmol/g			$a_m = 36.4$ mmol/g		
AMG-200	293 K			313 K		
	26	42	0.72	2	0.64	115.80
	28	51	0.78	3	0.69	107.88
	30	66	0.83	5	0.74	98.00
	32	85	0.89	7	0.78	94.91
	$a_m = 36.0$ mmol/g			$a_m = 40.8$ mmol/g		
AMG-400	303 K			313 K		
	16	14	0.66	1	0.46	207.39
	18	20	0.67	2	0.52	180.92
	20	30	0.75	4	0.57	158.34
	22	42	0.82	8	0.63	130.29
	24	58	0.90	13	0.69	117.49
$a_m = 26.8$ mmol/g			$a_m = 34.8$ mmol/g			
AMG-600	293 K			303 K		
	12	20	0.62	5	0.65	101.61
	14	50	0.73	13	0.76	99.10
	16	84	0.83	30	0.87	75.77
	$a_m = 19.2$ mmol/g			$a_m = 18.4$ mmol/g		

equation that interrelates the adsorption value  $a$ , the concentration  $C$ , and the temperature  $T$ . One of the principles of the system equilibrium thermodynamic function is the differential free molar energy of adsorption  $\Delta F$  [20,21]

$$\Delta F = -RT \ln K, \quad (4)$$

where  $K$  is the apparent constant of the adsorption equilibrium.

We will use the quantity  $-\Delta F$ , since, in our experiments, the temperature, volume, and weight of the system wherein the adsorption equilibrium was achieved are constant.

The adsorption was carried out from a binary solution (water–NaF) and, since the water concentration was higher by more than two orders of magnitude than the basic adsorbed component NaF, drawing an analogy with the vapor-phase adsorption [20], the expression for the standard decrease of the free molar energy of adsorption  $-\Delta F$  can be written in the form

$$-\Delta F = RT \ln C_s / C_e, \quad (5)$$

where  $C_s$  is the concentration of saturated NaF solution (mmol/l), and  $C_e$  is the equilibrium concentration of sodium fluoride (mmol/l) at the temperature  $T$ .

From the experimental isotherms of the sodium fluoride adsorption in the adsorption coordinates (or the adsorption layer population  $\theta$ ,  $\theta = a/a_m$ ), the equilibrium NaF concentration at two solution temperatures  $T_1$  and  $T_2$  for all the studied samples and the values of the fluoride adsorption molar energy decrease were calculated according to equation (5) at the equilibrium concentrations  $C_1$  and  $C_2$  corresponding to the determined  $\theta$  value. Standard values of the adsorption molar energy NaF ( $-\Delta F^0$ ) were found from the  $-\Delta F$ -vs- $\theta$  curve at  $\theta \rightarrow 0$ .

The differential isosteric heats of adsorption  $\bar{Q}$  at different populations  $\theta$  were calculated according to equation [21]

$$\bar{Q} = -RT^2(d \ln C_e / dT)_\theta. \quad (6)$$

Table 2 and Fig. 4 show values of the isosteric heat of fluorine adsorption for adsorbent samples depending on the surface filling degree by the adsorbate.

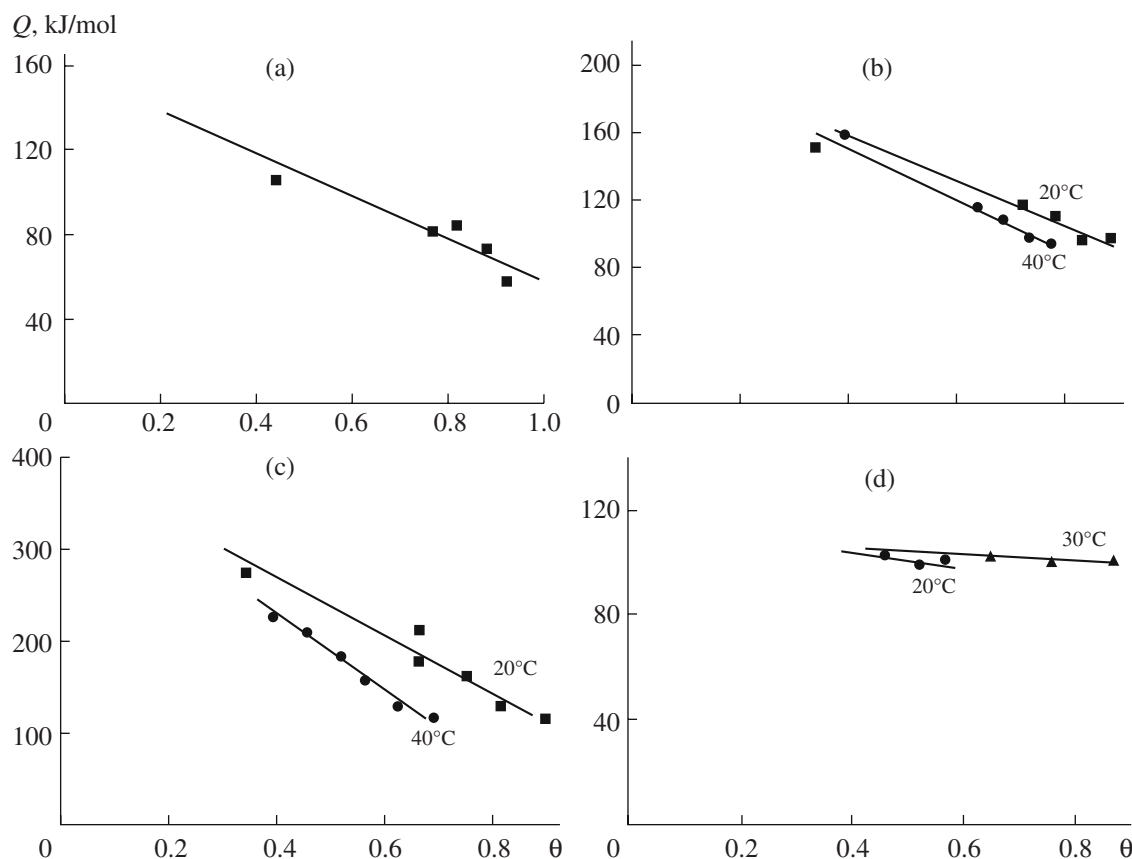


Fig. 4. Dependence of differential heats of fluorine adsorption from aqueous solutions on the filling degree of the surface of the samples. AMG-100 (a), AMG-200 (b), AMG-400 (c), and AMG-600 (d).

The data of Table 2 and Fig. 4 allow analyzing the dependence of the differential isosteric adsorption heat on the surface filling degree: its absolute value for all the samples gradually decreases as  $\theta$  increases. This decrease is related to both the increase of the sodium fluoride solubility coefficient with a rise in the temperature and the decrease of the solution chemical potential. It may also be attributed to the sorbent surface heterogeneity: initially, fluorine is adsorbed on the most active centers with the corresponding adsorption heats being greater in value; then, in proportion to the adsorption layer population, progressively less active surface centers come into interaction with this being reflected in the decrease of the adsorption heats.

From the  $\bar{Q}$ -vs- $\theta$  curve, by extrapolation to  $\theta \rightarrow 0$ , the standard isosteric fluorine adsorption heats  $\bar{Q}^0$  were found for all the studied samples.

The decrease of the standard molar entropy of adsorption  $\Delta S^0$  is related to the  $\Delta F^0$  values and the standard adsorption enthalpy ( $\Delta H^0 = -\Delta \bar{Q}^0$ ) by the fundamental relationship [22]

$$\Delta F^0 = \Delta H^0 - T\Delta S^0, \quad (7)$$

where from the  $\Delta S^0$  values were found.

The calculated  $-\Delta F^0$  values, the apparent constants of the adsorption equilibrium ( $\log K$ ), the standard isosteric heats, and the adsorption entropies are presented in Table 3.

It turned out that the values of the adsorption equilibrium constant logarithms for the studied samples in the interval of the investigated temperatures are within the range of 3.5–5.4. An increase of the solution temperature leads to an increase of the adsorption constant and, therefore, to an increase of the free energy of sodium fluoride adsorption. It should be noted that  $-\Delta F^0$  for the sample AMG-200 for all the solution temperatures is higher than for the other samples. This is a reflection of the variation of the porous structure of this sample as a result of the heat treatment that, as was mentioned in [14], leads to amorphization of its structure and, as a consequence, to development of the maximum specific area. The  $\bar{Q}^0$  values weakly depend on the solution temperature; however, they strongly differ for all the studied samples, varying from 156.5 to 364 kJ/mol.

The  $\Delta S^0$  values for the adsorption of fluoride ions from aqueous solutions for the studied samples

**Table 3.** Values of the standard decreases of the free adsorption energy  $-\Delta F^0$ , the isosteric adsorption heats  $\overline{Q}_0$ , and the standard entropy decreases  $\Delta S^0$  at fluoride-ion adsorption by heat-treated samples

Sample	Solution temperature, K	$\log K$	$-\Delta F^0$ , kJ/mol	$\overline{Q}_0$ , kJ/mol	$\Delta S^0$ , kJ/mol
AMG-100	293	3.69	20.70	156.40	-0.463
	303	3.50	20.30	—	—
	313	3.51	21.04	156.40	-0.432
AMG-200	293	3.92	22.02	203.20	-0.620
	303	4.24	24.60	202.80	-0.588
	313	5.42	32.50	201.96	-0.541
AMG-400	293	3.54	19.80	—	—
	303	3.74	21.70	364.60	-1.13
	313	4.15	24.90	336.20	-0.994
AMG-600	293	3.75	21.06	174.40	-0.523
	303	3.87	22.50	186.50	-0.541
	313	4.25	22.50	177.70	-0.486

(Table 3) count in favor of the fact that they vary only slightly at the solution temperature increase for one and the same sample, yet they differ by a factor of 1.5–2 for different samples. Nevertheless, in the absolute value, the standard variation of the adsorption entropy is not so appreciable (0.43–1.13 kJ/(mol K)). The  $\Delta S$  values are negative; that is, the mobility of the adsorbed fluorine is less than that in the bulk solution at equilibrium. Thus, fluoride-ion adsorption by sorbent samples is determined by the system entropy decrease. In proportion to the adsorption layer filling degree, the differential entropies slightly increase while remaining all the while in the range of negative values; this testifies to the fluoride-ion mobility increase in the adsorption layer while approaching a monolayer coating. It follows from the obtained data that the sample selectivity with respect to fluorine ions increases with a rise in the temperature; that is, the process of exchange of fluorine, being present in the solution in the form of hydrated fluoride ions, for hydroxyl ions is endothermal. The fluorine adsorption increasing with a rise in temperature may be due, first of all, to the increase of the sodium fluoride solubility coefficient; due to the surface charge variation [19]; and, probably, due to fluorine entering into the inner coordination sphere of aluminum (fluoride ions are able to compete with  $\text{OH}^-$  groups of Al oxyhydroxides in the inner coordination sphere of aluminum ions) [23].

## CONCLUSIONS

The influence of the solution temperature on the rate and equilibrium of the fluorine adsorption process on the heat-treated samples of residues obtained at DECM of the AMG-6 alloy has been studied. The adsorption process adheres to the pseudo-first-order chemical

kinetics equation. The variation of the solution temperature in the adsorption process leads to two important consequences: (i) the rate of the fluorine ion diffusion inward the sorbent particles increases; (ii) the temperature increase results in an increase of the sorbent adsorption capacity with respect to fluoride ions. The thermodynamic parameters of the adsorption process make it possible to predict how the adsorption can vary with the temperature variation. The study of the solution temperature influence on the equilibrium and kinetics of the process of fluorine-anion adsorption allowed determination of the values of the apparent thermodynamic parameters of the adsorption process ( $\Delta G^0$ ,  $\Delta H^0$ , and  $\Delta S^0$ ).

The obtained results confirm the expressed hypothesis of the possible mechanisms of fluorine ion sorption. Thus, the apparent variation of the enthalpy in the course of the fluoride-ion adsorption by the studied samples is 109–350 kJ/mol; this counts in favor of the chemical reaction proceeding in the sorption process.

The obtained values of  $E_a$  (20–62 kJ/mol) correspond to the activation energy values characteristic of the processes controlled by inside diffusion.

The predominant mechanism of fluorine removal appears to consist of the chemisorbed ligand exchange reaction, including the formation of and intraspheric complex of fluorine and aluminum. The low values of  $E_a$  for the samples of AMG-400 and AMG-600 show that the adsorption by these samples may be physical. This means that the rate-limiting step of fluorine adsorption contains mainly the physical process. These data, coupled with the rectilinear dependences of the equilibrium degree  $F(\%)$  on  $\sqrt{t}$ , have shown that the kinetics of the fluoride-ion sorption for the studied sam-



ples are determined by the diffusion inside the particles, and the diffusion coefficient values are within the range of 0.10–0.57 cm<sup>2</sup>/s.

## REFERENCES

1. Klyachko, V.A. and Apel'tsyn, I.E., *Ochistka prirodnikh vod* (Purification of Natural Water), Moscow: Stroiizdat, 1971.
2. Yeun, C. Wu and Anan, Nitya, Water Defluoridation with Activated Alumina, *J. Environ. Eng. Div.*, 1979, vol. 105, no. 2, pp. 357–367.
3. Kul'skii, K.A. and Strokach, P.P., *Tekhnologiya ochistki prirodnikh vod* (Technology of Natural Water Purification), Kiev: Vysshaya Shkola, 1986.
4. Romanov, A.M., Drondina, R.V., Matveevich, V.A., et al., *Ochistka podzemnykh vod ot toksichnykh primesei elektrokhimicheskimi metodami* (Underground Water Purification from Toxic Impurities by Electrochemical Methods), Chisinau, 1985.
5. Maurice, S. Onyango and Hitoki, Matsuda, Fluoride Removal from Water Using Adsorption Technique, *Adv. Fluor. Sci.*, 2006, vol. 2, pp. 1–48.
6. Meenakshi, and Maheshwari, R.C., Fluoride in Drinking Water and Its Removal, *J. Hazard. Mater.*, 2006, vol. 137, no. 1, pp. 456–463.
7. Krishna, Biswas, Sanat, Kumar Saha, and Uday, Chand Ghosh, Adsorption of Fluoride from Aqueous Solution by a Synthetic Iron(III)–Aluminum(III) Mixed Oxide, *Ind. Eng. Chem. Res.*, 2007, vol. 46 (16), pp. 5346–5356.
8. Hiemstra, T. and Van Riemsdijk, W.H., Fluoride. Adsorption on Goethite in Relation to Different Types of Surface Sites, *J. Colloid Interface Sci.*, 2000, vol. 225, no. 1, pp. 94–104.
9. Akbar, Eskandarpour Maurice S. Onyango, Aoyi, Ochieng, and Shigeo, Asai, Removal of Fluoride Ions from Aqueous Solution at Low pH Using Schwertmannite, *J. Hazard. Mater.*, 2008, vol. 152, no. 2, pp. 571–579.
10. Subhashini, Ghorai and Pant, K.K., Equilibrium, Kinetics, and Breakthrough Studies for Adsorption of Fluoride on Activated Alumina, *Sep. Purif. Technol.*, 2005, vol. 42, no. 3, p. 265.
11. Fan, X., Parker, D. J., and Smith, M.D., Adsorption Kinetics of Fluoride on Low Cost Materials, *Water Res.*, 2003, vol. 37, no. 20, pp. 4929–4937.
12. Sushree, Swarupa Tripathy, Jean-Luc, Bersillon, and Krishna, Gopal, Removal of Fluoride from Drinking Water by Adsorption onto Alum–Impregnated Activated Alumina, *Sep. Purif. Technol.*, 2006, vol. 50, no. 3, pp. 310–317.
13. Davydov, A. and Kozak, E. *Vysokoskorostnoe elektrokhimicheskoe formoobrazovanie* (High–Rate Electrochemical Morphogenesis), Moscow: Nauka, 1990.
14. Zelentsov, V.I. and Datsko, T.Ya., Porous Structure of Products of DECM of Aluminum Alloy Subject to Heat–Treatment, *Elektron. Obrab. Mater.*, 1999, no. 4, pp. 59–65.
15. Zelentsov, V.I., Datsko, T.Ya., and Dvornikova, E.E., Fluorine Adsorption by Heat–Treated Aluminum Oxyhydrates, *Elektron. Obrab. Mater.*, 2008, No. 1, pp. 75–81.
16. Emmanuel', N.M. and Knorre, D.G., *Khimicheskaya kinetika* (Chemical Kinetics), Moscow: Vysshaya Shkola, 1969.
17. Hajjaji, M., Kacim, S., Alami, A., El Bouadili, A., and El Mountassir, M., *Appl. Clay Sci.*, 2001, vol. 20, pp. 1–8.
18. Papelis, C, Roberts, P.V., and Leckie, J.O., Modelling the Rate of Cadmium and Selenite Adsorption on Micro– and Mesoporous Transition Aluminas, *Environ. Sci. Technol.*, 1995, vol. 29, pp. 1099–1108.
19. Bleza, M.A., Figliolia, N.M., Maroto, A.J.G., and Regazzoni, A.E., The influence of Temperature on the Interface Magnetite–Aqueous Electrolyte Solution, *J. Colloid Int. Sci.*, 1984, vol. 101, no. 2, pp. 410–418.
20. Dubinin, M.M., *Adsorbtsiya i poristost'* (Adsorption and Porosity), Moscow, 1972.
21. Koganovskii, A.M., Levchenko, T.M., and Kirichenko, V.A., *Adsorbtsiya rastvorenykh veshchestv* (Adsorption of Dissolved Materials), Kiev: Naukova Dumka, 1977.
22. Gerasimov, Ya.I., et al., *Kurs fizicheskoi khimii* (Course of Physical Chemistry), Moscow: Khimiya, 1973, vol. 2.
23. Duke, Catherine V. A., Miller, Jack M., Clark, James H., and Kybett, Adrian P., <sup>19</sup>F Mas NMR and FTIR Analysis of the Adsorption of Alkali Metal Fluorides onto Alumina, *J. Mol. Catal.*, 1990, vol. 62, no. 2, pp. 233–242.

## ELECTRICAL PROCESSES IN ENGINEERING AND CHEMISTRY

# Study of the Effect of Heightened Temperatures and Pressure on the Electric Strength of Polymethylsiloxane Liquid PMS-20 and Castor Oil Saturated with Nitrogen

**A. Ya. Dmitrishin, V. I. Gun'ko, L. I. Onishchenko, I. Yu. Grebennikov, S. O. Toporov**

*Institute of Pulse Research and Engineering, National Academy of Sciences of Ukraine,*

*Pr. Oktyabr'skii 43-a, Nikolaev, 54018 Ukraine*

*e-mail: iipt@iipr.com.ua*

Received January 9, 2008

**Abstract**—The results of the study of the influence of heightened temperatures and pressure on the electric strength of polymethylsiloxane liquid PMS-20 and castor oil saturated with nitrogen are presented in this paper. It is possible to apply the data at creation of electrotechnical devices, in particular, high-voltage pulse capacitors.

**DOI:** 10.3103/S1068375508030083

At present, there is being carried out work on the development of submersible electric-discharge complexes with improved power characteristics at the IPRE of the National Academy of Sciences of Ukraine. High-voltage pulse capacitors in which electrically strong gas (being a compressible material) is used to balance the liquid dielectric temperature expansion are applied as electric power accumulators. However, some gas dissolving in the capacitor liquid dielectric changes the electrophysical parameters of the fluid.

With the capacitor working as a part of a submersible electric-discharge complex at the ambient temperature of 100°C, there occurs the excess pressure inside it causing the growth (in conformity with Henry's law [1]) of the concentration of gas dissolved in the liquid dielectric. Moreover, a liquid dielectric saturated with gas is one of the main components of the dielectric system of a solid multilayer dielectric. Its durability mostly depends on the liquid electric strength as the dielectric system component most responsive to the effect of the partial discharges.

The estimation of the influence of electrically strong gases on the electrophysical parameters of liquid dielectrics has been conducted previously at the IPRE of the National Academy of Sciences of Ukraine. It turned out that the electric strength of liquid dielectrics (except for castor oil) diminishes with them being gas saturated at atmospheric pressure.

Data on the growth of the electric strength of gases at the excess pressure are presented in [2, 3]. In [4, 5], it is demonstrated with polar and nonpolar liquid dielectrics that the influence of the excess pressure on the increase of the partial discharges' voltage causes in turn a rise of the liquid electric strength. However, the increase of the excess pressure above some certain

value for both gases and liquids is irrational as the electric strength grows insignificantly, and, for each substance, the optimum excess pressure value is specific.

In this connection, the purpose of this work is to estimate the effect of the heightened temperatures and pressure on the electric strength of liquids saturated with an electrically strong gas.

Liquid dielectrics used in high-voltage pulse capacitor structures are chosen to carry out the investigation:

—polymethylsiloxane liquid PMS-20 GOST 13032-77;

—castor oil GOST 18102-94.

Nitrogen, which is widely used in electrical engineering, served as the electrically strong gas.

The liquids were previously refined and stabilized. The characteristics of the refined and stabilized liquids (the relative permittivity  $\epsilon$ , loss tangent  $\tan \delta$ , volume electric resistivity  $\rho_v$ , and electric strength  $E_{st}$ ) are presented in Table 1.

The liquids were flooded into the sealed test cells with consideration for their volumetric expansion coefficient, and the cells were filed with nitrogen without

**Table 1.** Data of measuring the characteristics of polymethylsiloxane liquid PMS-20 and castor oil after being refined and stabilized

Liquid dielectric	$\epsilon$	$\tan \delta$	$\rho_v$ Ohm cm	$E_{st}$ kV/mm
Polymethylsiloxane liquid PMS-20	2.65	$4 \times 10^{-4}$	$2.5 \times 10^{12}$	17.5
Castor oil	4.51	$1.2 \times 10^{-3}$	$6.95 \times 10^{11}$	26.5

**Table 2.** Data of measuring the electric strength of polymethylsiloxane liquid PMS-20 and castor oil saturated with nitrogen at various temperatures and gas pressures

Liquid dielectric	At a temperature of 15°C		At a temperature of 80°C		At a temperature of 100°C	
	Excess pressure, Pa	$E_{st. av.}$ , kV/mm	Excess pressure, Pa	$E_{st. av.}$ , kV/mm	Excess pressure, Pa	$E_{st. av.}$ , kV/mm
Polymethylsiloxane liquid PMS-20	0	15.4	$0.7 \times 10^5$	13.9	$0.9 \times 10^5$	12.6
	$1 \times 10^5$	21.6	$1.5 \times 10^5$	18.0	$1.7 \times 10^5$	16.4
	$2 \times 10^5$	23.2	$2.4 \times 10^5$	20.9	$2.6 \times 10^5$	19.0
	$3 \times 10^5$	25.5	$3.3 \times 10^5$	23.0	$3.5 \times 10^5$	20.9
Castor oil	0	21.4	$0.7 \times 10^5$	17.9	$0.9 \times 10^5$	15.3
	$1 \times 10^5$	27.7	$1.4 \times 10^5$	23.3	$1.7 \times 10^5$	21.3
	$2 \times 10^5$	33.2	$2.3 \times 10^5$	27.8	$2.6 \times 10^5$	23.8
	$3 \times 10^5$	38.9	$3.2 \times 10^5$	33.2	$3.5 \times 10^5$	28.4

excess pressure at the ambient temperature. After keeping for 24 hours, there was determined the electric strength of the liquids. Then, the test cells with the liquids and nitrogen were heated at a temperature of  $80^{+5}^{\circ}\text{C}$  for four hours. Manometer readings were taken and the electric strength was determined. The temperature was increased up to  $100^{+5}^{\circ}\text{C}$ , and the liquid samples with nitrogen were heated for four hours. Manometer readings were taken, and the electric strength of the liquids was evaluated.

The pressure and electric strength of the liquids in the test cells filled with nitrogen at excess pressures of  $1 \times 10^5$ ,  $2 \times 10^5$ , and  $3 \times 10^5$  Pa were similarly measured.

Data on the electric strength of polymethylsiloxane liquid PMS-20 and castor oil saturated with nitrogen at different temperatures and gas pressures are presented in Table 2.

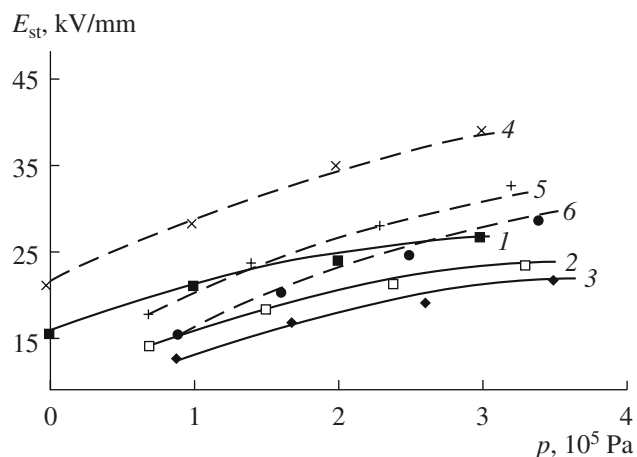
The electric strength versus the temperature and pressure characteristics based on the measurement results for polymethylsiloxane liquid PMS-20 and castor oil saturated with nitrogen are presented in the figure.

The analysis of these relationships shows that, in sealed volumes, at heightened temperatures up to  $100^{\circ}\text{C}$  with the pressure increasing, the electric strength rises exponentially. It is determined that, with the temperature growing up to  $100^{\circ}\text{C}$ , the electric strength of the liquids reduces. It is experimentally found that the compensation for the temperature decrease of the electric strength of polymethylsiloxane liquid PMS-20 and castor oil could be provided by an increase of the gas pressure. Thus, at  $100^{\circ}\text{C}$ , with the gas pressure increasing up to  $3 \times 10^5$  Pa, the electric strength of the liquids grows:

—that of polymethylsiloxane liquid PMS-20 by 1.65 times;

—that of castor oil by 1.85 times.

The conducted investigation is important from the scientific standpoint as it allows one to establish the peculiarities of the short-time and, therefore, long-term electric strength of the isolation at the saturation with electrically strong gas and to estimate the conditions causing the toughening of the occurrence of partial discharges in the liquid dielectric at heightened temperatures and pressures. From the practical standpoint, the results could be the basis for designing the inner isolation of high-voltage electrotechnical devices (capacitors, transformers, etc.) operating in strong electric



The electric strength–pressure relation for polymethylsiloxane liquid PMS-20 at temperatures of 15, 80, and  $100^{\circ}\text{C}$  (curves 1, 2, and 3, respectively) and for castor oil at temperatures of 15, 80, and  $100^{\circ}\text{C}$  (curves 4, 5, and 6, respectively) saturated with nitrogen.

fields at heightened temperatures and pressures providing high durability and specific energy characteristics of the products.

#### REFERENCES

1. *Phizicheskaya entsiklopediya: v 5 tomakh* (Physical Encyclopedia: in 5 Vol.), Prokhorov, A.M., Ed., Moscow, 1988.
2. Renne, V.T., *Electricheskie kondensatory* (Electric Capacitors), Leningrad, 1968.
3. Nashchokin, V.V., *Tekhnicheskaya termodinamika i teplotekhnika* (Technical Thermodynamics and Heat Engineering), Moscow, 1975.
4. Kuchinskii, G.S., *Vysokovol'tnye impul'snye kondensatory* (High-Voltage Pulse Capacitors), Leningrad, 1973.
5. Kuchinskii, G.S., *Vysokovol'tnye impul'snye kondensatory* (High-Voltage Pulse Capacitors), Moscow, 1975.



---

ELECTRICAL PROCESSES  
IN ENGINEERING AND CHEMISTRY

---

## Surface Properties and Modeling Potentiometric Titration of Aqueous Illite Suspensions<sup>1</sup>

A. Kriaa<sup>a,b</sup>, N. Hamdi<sup>b</sup>, and E. Srasra<sup>b</sup>

<sup>a</sup> *Departement de Chimie, Ecole Supérieure des Sciences et Techniques de Tunis,  
Rue Taha Hussein-Montfleury Tunis, Tunisia*

<sup>b</sup> *Unité matériaux, Technopole Borj Cedria, BP 95-2050 Hammam lif, Tunisia*

*e-mail: kriaa1993@yahoo.fr*

*Received November 19, 2007*

**Abstract**—The potentiometric titration behavior of complex illitic clay minerals provided from different origins (two Tunisian illite samples and an American illite sample) was investigated and interpreted according to the surface complexation theory. In the present investigation, the focus is on the surface charge characteristics. The proton surface charge can be calculated by subtracting the supernatant titration curves from those of the illite suspension at ambient temperature with an aerated medium. The points of zero charge (PZC), which were determined using the Gran plot method and the fast titration technique, were in the range of ~8.5–9.2. Our potentiometric titration curves were modeled using derived parameters of the Gran method. The surface ionization constants were determined by implementing the theory of surface complexation models (SCMs): the NEM, the constant capacitance model (CCM), and the triple layer model (TLM). The pK<sub>a</sub>s values determined from derived parameters of the Gran plot data were in the range of pK<sub>a1</sub> = 4.5–5.52 and pK<sub>a2</sub> = 9.78–10.4 and are compared to those obtained by SCMs.

**DOI:** 10.3103/S1068375508030095

### INTRODUCTION

Over the past several decades, significant advances have been achieved in the understanding of the chemistry of mineral surfaces and the mineral–water interface. One of the major developments is the successful application of surface complexation models (SCMs) to enhance our understanding of surface interactions involving simple minerals as well as synthesized single metal oxide and hydroxide minerals [1–5]. Among the SCMs commonly used in the literature are the diffuse layer model, the constant capacitance model, and the triple layer model, which are based on their ability to simulate the acid–base titration behavior of oxide surfaces. These three models are similar in their descriptions of surface reactions, each treating the surface as if it were composed of amphoteric hydroxide functional groups capable of reacting with sorbing cationic or anionic species to form surface complexes. However, these models differ in their complexity and descriptions of the electrical double layer and the manners in which changes in the background electrolyte concentration are incorporated in the model computations. Some authors have given a schematic representation of the electrical properties of the interfacial region [1], where the three SCMs in terms of adjustable parameters, including surface chemical reactions and the charge-potential relationships, are summarized in Table 1.

On the other side, because of their complex chemical composition, application of SCMs to complex natural clay minerals, as well to purified phyllosilicate clay minerals, is relatively rare. We can cite some studies on kaolinite [6, 7], on montmorillonite [8, 9], on bentonites [10], and on natural illite and glauconite [11–14]. We must notice that some experimental studies based on surface complexation modeling on natural and complex clay minerals, taking into account the considerable aqueous dissolution, have been carried out by some authors [7, 11, 14]. However, as mentioned by these authors, the correction for the dissolution effects yielded a modest improvement in the model simulation. The complexity of the model calculations were found to be increased greatly when numerous additional chemical reactions are considered. Also, the inclusion of ion exchange interactions produced no substantive improvement in the model fit by using the NEM and CCM. In general, the involvement of the CEC sites in proton adsorption has been most frequently neglected. Some authors emphasized that the exchange reactions between alkali or alkaline earth cations and protons is important only at low pH [15]. Other studies have corrected for the contribution of the CEC, because the reached pH was low enough [16, 17].

In this study, potentiometric titration experiments were used to investigate the acid–base chemistry of different illitic complex clay minerals. A new simple model approach based on derived parameters of the Gran method titration was proposed in order to deter-

<sup>1</sup> The text was submitted by the authors in English.

**Table 1.** Surface complexation reactions and model parameters

	DLM	CCM	TLM
Surface chemical reactions	$\equiv\text{SOH} + \text{H}^+ \leftrightarrow \equiv\text{SOH}_2^+ \quad K_{a1}$ $\equiv\text{SOH} \leftrightarrow \equiv\text{SO}^- + \text{H}^+ \quad K_{a2}$ $K_{a1}^{\text{int}} = K_{a1} \exp(F\Psi_0/RT)$ $K_{a2}^{\text{int}} = K_{a2} \exp(F\Psi_0/RT)$	Same as DLM	Same as DLM Ion pair complexes $\equiv\text{SOH} + \text{Cat}^+ \leftrightarrow \equiv\text{SO}^- - \text{Cat}^+ + \text{H}^+ \quad K_{\text{Cat}}$ $\equiv\text{SOH} + \text{An}^- + \text{H}^+ \leftrightarrow \equiv\text{SOH}_2^+ - \text{An}^- \quad K_{\text{An}}$
Charge-potential relationships	$-\sigma_0 = \sigma_d = -0.1174$ $\sqrt{I} \sinh(ZF\Psi_d/2RT)$	$\sigma_0 = C_1\Psi_0$	$\sigma_d = -0.1174 \sqrt{I} \sinh(ZF\Psi_d/2RT)$ $\sigma_0 = (\Psi_0 - \Psi_\beta)C_1$ $\sigma_0 + \sigma_\beta = (\Psi_\beta - \Psi_d)C_2$
Adjustable parameters	$K_{a1}^{\text{int}}, K_{a2}^{\text{int}}, D_s$ (total surface site density)	$K_{a1}^{\text{int}}, K_{a2}^{\text{int}}, C_1$ and $D_s$	$K_{a1}^{\text{int}}, K_{a2}^{\text{int}}, K_{\text{Cat}}, K_{\text{An}}, D_s, C_1, C_2$

mine the surface ionization constants. In addition, the well-known SCMs with different formulations and assumptions were applied neither to model the experimental data nor to compare with the pKas values obtained from the Gran parameters analysis.

It is well known that illite makes up half or more of the clay minerals in the earth's crust. Some works on different aspects of its behavior have been studied [11, 12], e.g., electrochemical properties and adsorption of contaminants.

Structurally, illite is a 2 : 1 layer-type clay mineral composed of one gibbsite sheet  $\gamma\text{-Al}(\text{OH})_3$  sandwiched between two silica sheets ( $\text{SiO}_4$ ), and the illite solution systems have only two kinds of surfaces: a siloxane surface and an edge surface [12]. Moreover, Katari and Tauhe [18] reported that certain clays such as illite can acquire a permanent negative charge on the face due to isomorphic substitution of  $\text{Al}^{3+}$  for  $\text{Si}^{4+}$  in the layer with tetrahedral coordination. A cloud of oppositely charged counter ions forming a diffuse double layer surrounds this negative surface. In addition, the flat basal surface of clay minerals is negatively charged due to cation exchange, but the edge surface behaves as an oxide. On their edges ( $\approx 10\%$  of the total surface area), charges arise from the breaking of Al–O and Si–O bonds resulting in amphoteric Al–OH and Si–OH surface function groups. These surface hydroxyls can be protonated or deprotonated depending on the pH of the suspension and the PZC of the edge of the clay particles. At a pH below the PZC, there will be an excess of  $\text{Al}(\text{OH})_2^+$  relative to Al–O $^-$ , resulting in a net positive charge for the edges. Some crystallographic considerations performed by Keren and Sparks [19] concerning the structure of pyrophyllite show that the most reactive surface functional group on the edge surfaces is the hydroxyl exposed on the periphery of the clay mineral. This functional group is associated with the structural cations Al(III) and Si(IV), which are located in the octahedral and tetrahedral sheets, respectively. At the edge of the

octahedral sheet, the Al(III) OH is a Bronsted acid site. The hydroxyl group associated with this site can interact with a proton at low pH values. At the edge of the tetrahedral sheet, hydroxyl groups are singly coordinated to  $\text{Si}^{4+}$  cations.

The major purposes of the study are (i) to investigate the surface charge characteristics of three illitic clay minerals provided from different locations by potentiometric titration using the Gran method and fast titration technique, (ii) to implement a new simple model in order to determine pKas values using derived parameters of the Gran plot method, and (iii) to confirm these pKas values by implementing the SCMs to characterize the acid–base chemistry of complex illite samples. These aspects have not been widely studied in the literature in relation to the few studies concerning illite clay mineral [11–14]. We think, in agreement with [13], that, in order to acquire more details on the acid–base properties at illite surface binding sites, a comparative study concerning illite samples collected from different locations would be conducive to obtain a more comprehensive understanding of the adsorption. Furthermore, a unified thermodynamic model can be set up to describe the general behavior of the surface acid–base properties over a group of illitic minerals.

## MATERIALS AND METHODS

### Clays

The solid samples were gathered from three sources: (1) an American illite sample from Montana (USA) (light green color specimen), (2) an illite sample (glauconite) from Gafsa in southern Tunisia (dark green color specimen), and (3) an illite-chlorite mixed-layer sample from El Hamma in southern Tunisia (red color specimen). Hereafter, they are abbreviated as It (Mo), It (Ga), and It (Ha), respectively. The clay fraction (particle size  $< 2$  micrometers) was purified by classical methods [20] and transformed into the sodium form with a 1 M NaCl solution. After washing, sedi-

**Table 2.** Chemical composition of the samples

%	SiO <sub>2</sub>	Al <sub>2</sub> O <sub>3</sub>	Fe <sub>2</sub> O <sub>3</sub>	MgO	Na <sub>2</sub> O	K <sub>2</sub> O	CaO	Ignition loss
It (Mo)	50.24	24.38	5.58	2.13	1.21	9.39	0.05	7.53
It (Ga)	53.34	3.41	24.98	4.04	0.5	7.58	0.19	7
It (Ha)	53.42	15.82	9.44	3.49	2.08	7.04	0.89	8.05

mentation, and dialysis, the fine clean sediment was freeze dried.

### CHEMICAL ANALYSIS

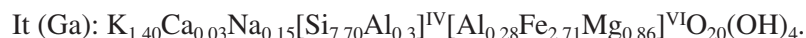
The chemical analysis of the purified samples is summarized in Table 2. It follows from this analysis that

Compared to the American illite, the Tunisian glauconite (It (Ga)) contains a higher content of Fe<sub>2</sub>O<sub>3</sub> and

a low ratio of Al<sub>2</sub>O<sub>3</sub>. One can notice that our samples contain a high amount of K indicating that all the samples are illitic clay minerals.

The peak surfaces of the d<sub>001</sub> reflections of illite and chlorite, respectively, were determined using PANalytical X'Pert High Score Plus software. The amount of chlorite in the illite was estimated as 20%.

The average structural formulas of the purified It (Mo) and It (Ga) samples are as follows:



The structural formula of It (Ha) has not been determined; the presence of chlorite makes the formula more complicated.

It follows from these formulas that the illite samples used in this study represent two types of substitutions (octahedral and tetrahedral substitutions). The charge per unit cell is 1.61 for It (Ga) and 1.98 for It (Mo). As can be noticed, the It (Ga) sample contains essentially Fe in the octahedral sheet, but, in the It (Mo) sample, Al (III) occupies the octahedral sheet. Moreover, the tetrahedral substitution rate is more important for It (Mo) than for It (Ga).

The cationic exchange capacities (CEC) and the specific surface areas (SSA) for the three purified samples are summarized in Table 3. It appears that all the CEC values are relatively lower than the other clay minerals (smectite), thus confirming that these solid samples belong to illitic minerals. The  $S_{BET}$  values of these samples are close.

### PZC Determination by Fast Titration

Potentiometric titrations of the illite samples were conducted in a reactor pyrex cell that included the fol-

lowing: a microburette with a very fine tip containing the titrant (HCl) and an HI 9321 microprocessor pH meter (Hanna Instruments) combination electrode, which was calibrated with two commercial pH buffers at ambient temperature with an aerated medium.

The acid-base potentiometric titration curves at different salt concentrations were used to measure the proton adsorption or proton charge. The experimental method employed was similar to that used by Boisset [21] for "alumina, hematite, and rutile" and Kriaa [22] for Kaolinite. 30 ml of the background electrolyte (NaCl) solution of concentration 0.1, 0.01, and 0.001 containing a 0.05 g sample was equilibrated for 15 min with continuous stirring in order to reach an equilibrium pH value. When a small amount of HCl was added to protonate a significant part of the surface sites, the pH quickly stabilized ( $\Delta pH < 0.03$  unity pH) and was read within 30 s. During the titration and after the addition of HCl, the pH rapidly reached a constant value and remained invariable with time. The titration was stopped when the pH was around 4 in order to avoid the possible occurrence of chemical phenomena such as the dissolution of the illite clay mineral. All the experiments were repeated at least in duplicate to confirm the results. Blank titrations were also performed with similar solutions in the absence of the clay suspensions.

**Table 3.** CEC cationic exchange capacity and SSA specific surface area values of the three illitic samples

Specimen	CEC, meq/100 g	$S_{BET}$ , m <sup>2</sup> /g
It (Mo)	27	45
It (Ga)	24	60
It (Ha)	34	51

### Potentiometric Titration Curves Using the Gran Plot Method

The experimental method was similar to that used by Du [11] for illite suspensions. For all the acid-base

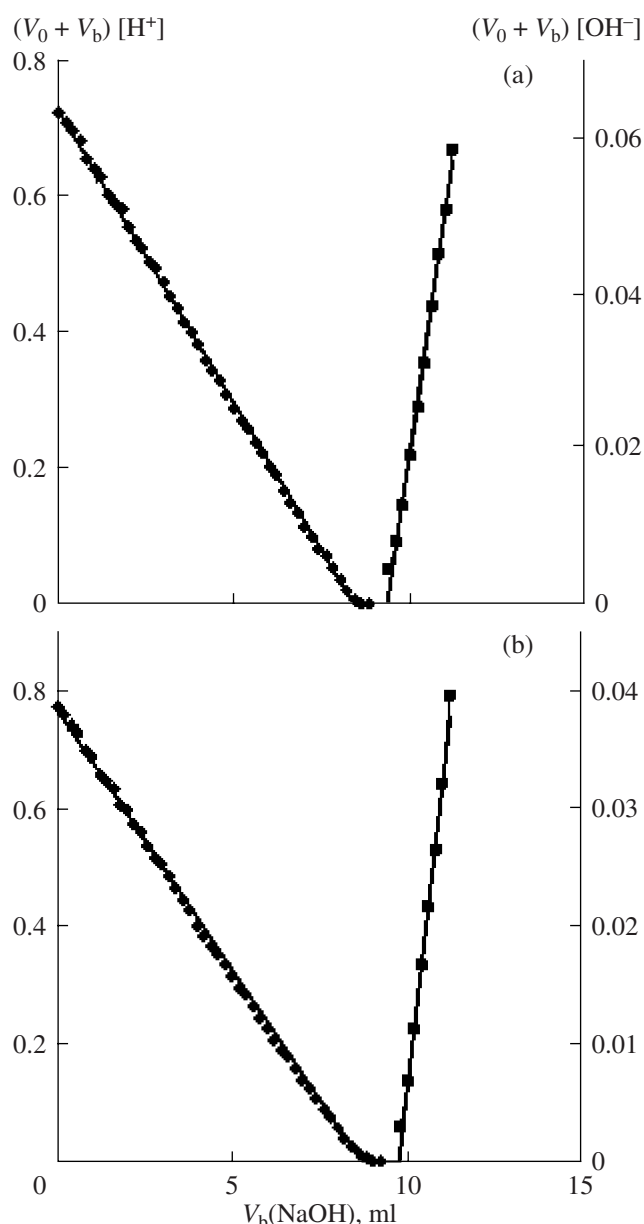


**Fig. 1.** Gran plot of the It (Mo) suspension in 0.1 M NaCl solutions; (a) blank system,  $Ve_1 = 8.416$ ,  $Ve_2 = 9.348$ ; (b) aqueous suspension,  $Ve_1 = 8.687$ ,  $Ve_2 = 9.748$ .

titrations, the illite suspensions were firstly acidified using  $HCl$   $10^{-2}$  M at a pH of approximately 2 and then titrated immediately with hydroxide solution ( $5 \times 10^{-2}$  M) to the alkaline pH range. For each titration, a certain amount of 0.1 g illite stock suspension was added to a 15 ml water flask and stirred for 24 hours in order to attain equilibrium criteria. An NaCl solution was used to stabilize the system at a given ionic strength. Distilled water was added to bring the total initial volume of the suspension to 50 ml. The temperature was held constant at  $25 \pm 0.5^\circ C$ . Afterwards,  $5 \times 10^{-2}$  M NaOH in 0.2 ml increments was used to titrate the suspension up to a pH of approximately 11. The equilibrium crite-

rium for each addition of the titrant was the stability of the pH value measured.

Concerning the blank system for each sample, we used the supernatant of the corresponding sample system as the titration blank. The procedure for obtaining the supernatant was as follows: an illite sample suspension with the same composition as the one used in the corresponding sample titration was prepared. The suspension was centrifuged at 3000 rpm for 10 min. The supernatant thus obtained was titrated according to the procedure described above. The controlling condition during the titration was the same as that for the sample titration.

The NaCl electrolyte concentration was adjusted to 0.1, 0.01, and 0.001 mol/l. For all the experiments, potentiometric titration curves, and before each titration, the aqueous suspensions and their corresponding supernatant blank systems were equilibrated for about 10 min in order to reach an equilibrium pH value.

#### Data Treatment

For the titration of the solid–water systems and their corresponding supernatant, we choose the Gran titration method as used by some researchers [11, 12, 23, 24] to accurately determine the equivalence points of the potentiometric titrations in aqueous solutions and the net number of reacted protons per surface site ( $Z_{net}$ ). Then, the point of zero charge is evaluated by determining the common intersection points of the illite suspensions. For each studied system, a Gran plot was made from the experimental data for the hydroxide titration. The  $Ve_1$  and  $Ve_2$  values determined by linear regression in the corresponding Gran plot are shown in Fig. 1.

#### Parameters of the Gran Method

Therefore, for each titration point, the concentration of the total protons added to the system was calculated by

$$TOTH = -(V_b - Ve_1)C_b / (V_0 + V_b), \text{ mol/l}, \quad (1)$$

where  $V_b$  is the volume of NaOH added in the hydroxide titration,  $V_0$  is the initial volume of the suspension, and  $C_b$  is the concentration of NaOH.

The determination of the total surface site concentration ( $H_s$ ) was calculated from the two equivalence points in the Gran plot of the hydroxide titration (see Fig. 1,  $Ve_1$  and  $Ve_2$ ) after subtracting the hydroxide consumed by the blank solution as shown in the equation below:

$$H_s = [(Ve_2 - Ve_1)C_b]_{\text{sample}} - [(Ve_2 - Ve_1)C_b]_{\text{blank}} / V_0, \text{ mol/l}. \quad (2)$$

The calculation of the average number of protons reacted per surface site ( $Z$ ) was determined at each titration point by

$$Z = [TOTH - 10^{-pH} + 10^{-(pK_w - pH)}] / (V_0 + V_b) / H_s V_0. \quad (3)$$



TOTH and  $H_s$  were calculated by Eqs. (1) and (2), respectively. For each illite system, the net number of surface reacted protons per surface site  $Z_{\text{net}}(\text{pH}, I)$  was obtained from the difference between the  $Z$  values of the sample titration and the corresponding blank titration at the same pH:

$$Z_{\text{net}}(\text{pH}, I) = Z_{\text{sample}} - Z_{\text{blank}}.$$

The surface site density ( $D_s$ ) was calculated at a given ionic strength from the  $H_s$  value using the equation

$$D_s = (H_s \cdot N_A) / (S \cdot C_s \times 10^{18}) \text{ sites/nm}^2, \quad (4)$$

where  $N_A$  is Avogadro's number ( $6.02 \times 10^{23} \text{ mol}^{-1}$ ),  $S$  the  $N_2/\text{BET}$  surface area, and  $C_s$  is the illite solid concentration (g/l).

#### Determination of the Surface Acidic Constants

The two most common methods for determining the surface equilibrium constants from the titration data are by using objective curve fitting routines or by graphical extrapolation methods on pure mineral oxides [15, 25, 26], on synthetic mixed oxides of iron and silicon [4], and on kaolinite [7] by computing the proton adsorption according to surface complexation models (the nonelectrostatic model and constant capacitance model) and on glauconite [14] and on illite [11–13] by using the nonlinear least-square optimization program FITEQL. In this study, graphical methods were mainly selected. From the derived parameters of the Gran plot data, the surface constants' ionizations were computed using the method based on the Hasselbach equation [24] for colloidal aqueous solutions of soils. In order to confirm these pKas values, surface complexation models (SCMs) were used to describe the titration data and thus to calculate these equilibrium constants. The non-electrostatic model (NEM), the constant capacitance model (CCM), and the triple layer model (TLM) were implemented without using the dissolution correction approach.

## ANALYSIS AND DISCUSSION

### Titration Curves

The proton adsorption or proton surface charge density  $\sigma_H$  ( $\text{mol/m}^2$ ) determined from the potentiometric titration was calculated as the difference between the total amounts of  $H^+$  or  $(OH^-)$  added to the dispersion and that required to bring a blank solution of the same NaCl concentration to the same pH [27]:

$$\sigma_H (\text{mol/m}^2) = \frac{V}{m} S \left\{ ([H^+]_b - [H^+]_s) - \left( \frac{K_w}{[H^+]_b} - \frac{K_w}{[H^+]_s} \right) \right\}, \quad (1)$$

where  $V$  is the volume of the electrolyte solution equilibrated with the illite sample (30 ml);  $[H^+]$  is the solution proton concentration (mol/l);  $K_w$  is the dissociation product of water ( $10^{-14}$ ); and the subscripts  $s$  and  $b$  refer to the sample and blank solutions, respectively.  $M$  is the mass of the sample used (0.05 g), and  $S$  is the specific surface area ( $\text{m}^2/\text{g}$ ).

Sensitivity estimations. Based on the calibration titration and on the readings of the electrode potentials, the uncertainty in the measured pH is estimated to be  $\pm 10\%$ .

Furthermore, in our titration experiments, because of the short equilibration time (15 min), the release of Si and Al caused by the illite dissolution (generally at pH 3–4) into the aqueous solution was not significant and was assumed to be negligible during the titration experiments. This observation is supported by some authors cited by Duc [28], who found that two major processes occur simultaneously during titration: surface site dissociation–complexation and dissolution. At ambient temperature, dissolution is kinetically slower than acid–base surface site reactions.

For all the illite samples, equilibrium data were used to plot the  $\sigma_H$  vs. pH curves. We have verified that the data obtained with HCl superimposed well with those obtained with NaOH, indicating good reversibility of the  $H^+$  adsorption process, which is in agreement with some authors for montmorillonites [29, 30].

Our experimental titration curves demonstrate that the studied illite samples do not present a net crossing point in the proton adsorption curves (see, for example, Fig. 2 for It (Mo)) in comparison with classical curves of pure simple oxides at different ionic strengths [25, 31]. The absence of an intersection point for montmorillonite was attributed to the combined effect of both variable charges and permanent negative charges [29].

In the absence of any specific adsorption, the PZNPC is equivalent to the pH of the zero point of the charge [27]. Their values for the illite samples are situated at pH  $\sim 7.5$ – $8.4$ ,  $\sim 8.2$ – $8.7$ , and  $\sim 9.1$ – $9.3$  for the It (Mo), It (Ha), and It (Ga), respectively. This reveals that the presence of chlorite has an effect on the shifting PZC value of It (Ha) toward higher pH values. In this case, no experimental studies dealing with  $H^+$  adsorption of chlorite were found in the literature. Hendershot and Lavkulich [32] found PZC values in the range of  $\sim 7.5$ – $8$  for  $\text{Na}^+$  illite in different NaCl solutions with  $I$  varying from 0.002 M to 0.1 M. In comparison with other published experimental data for illite, these values are higher; this is probably due to the basic character of our illite samples (the stability pH of the equilibrium suspensions in distilled water is in the range of 7.9–9.5).

On the other hand, our acid–base titration results determined from the Gran plot method ( $Z_{\text{net}}$  vs. the pH) are presented in Fig. 3 for It (Mo), It (Ga), and It (Ha), respectively. The curves do not show a crossing point corresponding to the PZC pH. They clearly dem-



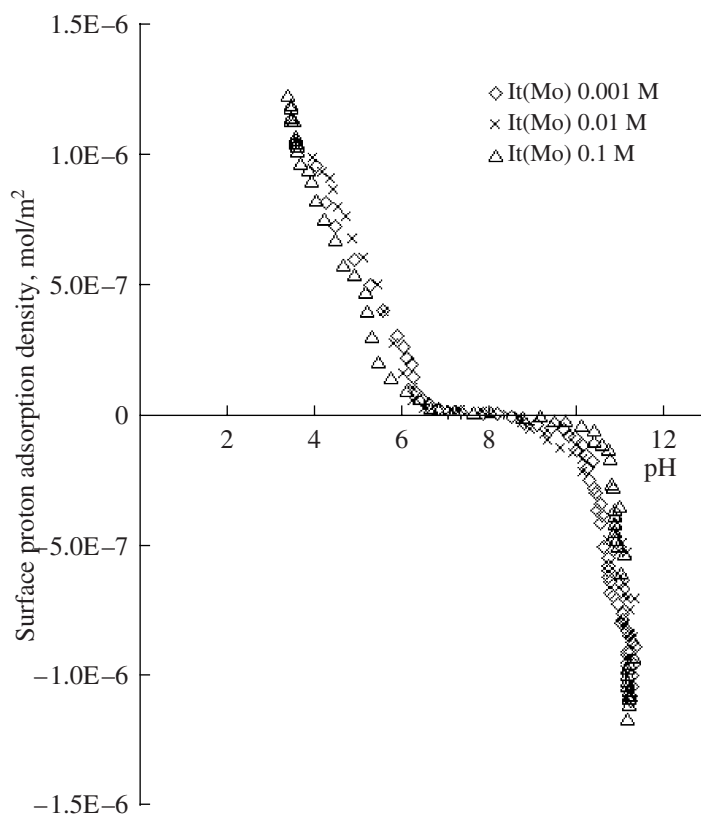


**Fig. 2.** Experimental acid–base of pure It (Mo) obtained at various ionic strengths in an aerated medium at 25°C.

onstrate that the PZCs' pH for the illitic samples are nearly similar to those determined by the fast titration technique (Table 4). One may deduce that there is very good agreement between the acid–base potentiometric curves and the fast titration technique.

#### Simple Model Approach

From the experimental data and the derived parameters of the Gran plot, we suggest that the determination of the surface acidic constants can be determined using the two sites two pKas model. One can notice that the one-site two pKas model can be chosen for the following reasons (see below).

**Table 4.** Point of zero charge determined by the Gran method and fast titration technique

Sample	PZC		pH in distilled water
	Gran Method	Fast titration technique	
It (Mo)	~8.2	~8.5	7.9
It (Ga)	~8.8	~9.2	9.5
It (Ha)	~8.3	~8.6	8.2

In the two sites two pKas model, we assume the existence of two kinds of sites as shown in the following equations—weak acidic sites that dissociate at a pH between 4–8 and have a concentration of [Wa] sites and weak basic sites that dissociate at pH ~8.5 and have a concentration of [Wb] sites [24]:



where  $\equiv\text{SOH}$  is the amphoteric surface hydroxyl group for the surface protonation model.

Moreover, when the interface of clay mineral–water has many different acidic sites, the successive dissociation can be defined by their dissociation coefficients  $\alpha_1$  and  $\alpha_2$  corresponding to  $\text{p}K_{a1}$  and  $\text{p}K_{a2}$ , respectively:

$$\alpha_1 = [\equiv\text{S}_\text{I}\text{OH}_2^+] / [\text{Wa}]$$

$$\text{and } \alpha_2 = [\equiv\text{S}_\text{II}\text{O}^-] - [\text{Wa}] / [\text{Wb}] + [\text{Wa}],$$

where  $[\text{Wa}] = (V_{\text{eq}} - V_{e1}) \times \text{Cb} / (V_0 + V_{e1})$  and  $[\text{Wb}] = (V_{e2} - V_{\text{eq}}) \times \text{Cb} / (V_0 + V_{e2})$ .

$V_{\text{eq}}$  is the equivalence point determined by the maximum of the differential curve  $d\text{pH}/dV$ . From (1),  $1/K_{a1} = [\equiv\text{S}_\text{I}\text{OH}_2^+] / [\equiv\text{S}_\text{I}\text{OH}] \times [\text{H}^+]$  or  $\text{pH} = \text{p}K_{a1} -$

$\log[\equiv\text{SiOH}_2^+]/[\equiv\text{SiOH}]$ . If  $\alpha_1 = [\equiv\text{SiOH}_2^+]/[\equiv\text{SiOH}_2^+ + \equiv\text{SiOH}]$ , then  $\text{pH} = \text{pK}_{a1} - \log \alpha_1 / 1 - \alpha_1$ . Using the Hasselbach equation, by extrapolating the linear regression curve for the  $\text{pH}$  vs.  $\log \alpha_1 / 1 - \alpha_1$  to zero, we can access the  $\text{pK}_{a1}$  value. For determining the  $[\equiv\text{SiOH}_2^+]$  concentration, we used the charge balance equation and the Gran plot data:

$$[\text{H}^+] + [\text{Na}^+] + [\equiv\text{SiOH}_2^+] = [\text{OH}^-] + [\text{Cl}^-],$$

with  $[\text{Na}^+] = C_b \times V_b / V_0 + V_b$  and  $[\text{Cl}^-] = C_b \times V_{e1} / V_0 + V_b$ :

$$[\equiv\text{SiOH}_2^+] = [\text{OH}^-] - [\text{H}^+] + C_b(V_{e1} - V_b)/V_0 + V_b$$

$$[\equiv\text{SiOH}_2^+] = \text{TOTH} + 10^{(\text{pH} - \text{pK}_w)} - 10^{-\text{pH}}.$$

From (2),  $\alpha_2 = [\equiv\text{SiO}^-] - [\text{Wa}]/[\text{Wb}] + [\text{Wa}]$ . Also, we determined the  $[\equiv\text{SiO}^-]$  concentration from charge balance equation:

$$[\equiv\text{SiO}^-] + [\text{OH}^-] + [\text{Cl}^-] = [\text{H}^+] + [\text{Na}^+] + [\equiv\text{SiOH}_2^+].$$

After the  $\text{pH} > 8.5$ , we can neglect the concentration of  $[\equiv\text{SiOH}_2^+]$ . Then,  $[\equiv\text{SiO}^-] = [\text{H}^+] - [\text{OH}^-] + C_b(V_b - V_{e1})/V_0 + V_b$

$$[\equiv\text{SiO}^-] = 10^{-\text{pH}} - 10^{(\text{pH} - \text{pK}_w)} + C_b(V_b - V_{e1})/V_0 + V_b$$

$$[\equiv\text{SiO}^-] = -\text{TOTH} + 10^{-\text{pH}} - 10^{(\text{pH} - \text{pK}_w)}.$$

For each illite sample and at a given ionic strength, the  $\text{pK}_{a1}$  and  $\text{pK}_{a2}$  values are determined by extrapolation of the  $\text{pH}$  vs.  $\log \alpha / 1 - \alpha$  to zero (Fig. 4) and are reported in Table 5.

The overall surface ionization constants for the protonation (AlOH groups) and deprotonation (SiOH groups) reactions of our illite edge sites are in the range  $4.5 < \text{pK}_{a1} < 5.52$  and  $9.78 < \text{pK}_{a2} < 10.42$ . It may be interesting to compare these values with those reported in the literature for other complex clay minerals. For example, Lu and Smith [14] listed  $\text{pK}_{a1}^{\text{int}} = 4.77\text{--}5.115$  and  $\text{pK}_{a2}^{\text{int}} = 7.63\text{--}7.56$  for glauconite without a disso-

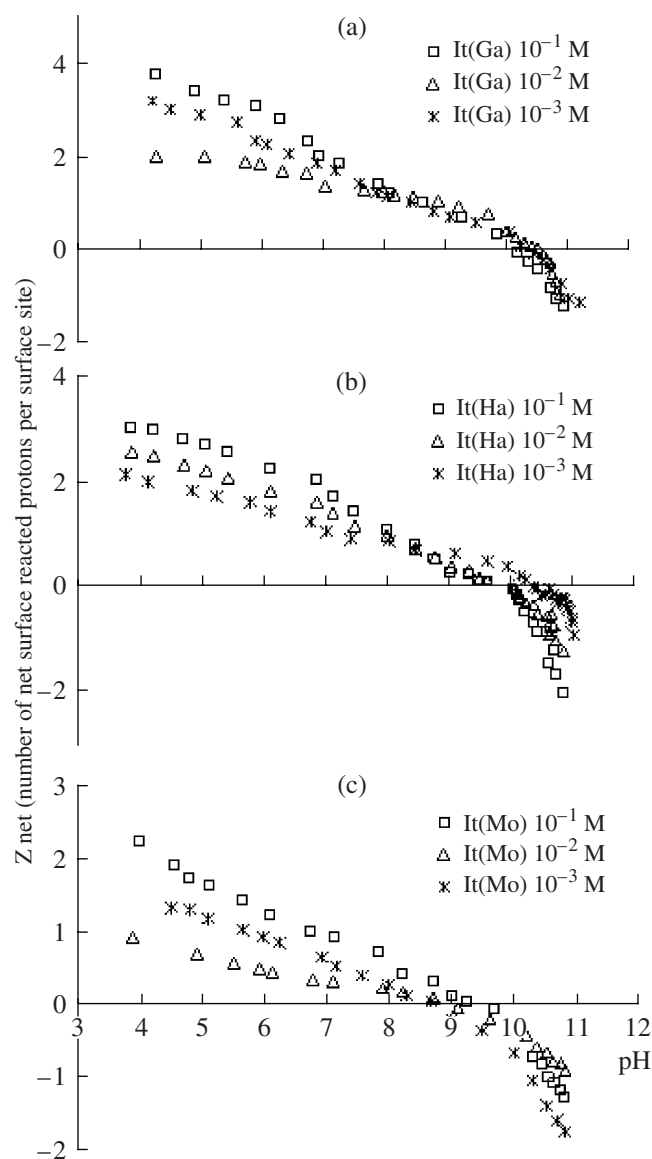


**Fig. 3.** pH-dependent net number of surface-reacted protons per surface site: (a) It (Ga), (b) It (Ha), (c) It (Mo).

**Table 5.**  $\text{pK}_{a1}$  and  $\text{pK}_{a2}$  values determined from the parameters of the Gran plot method

Sample	It (Mo)			It (Ga)			It (Ha)		
	$10^{-1}$	$10^{-2}$	$10^{-3}$	$10^{-1}$	$10^{-2}$	$10^{-3}$	$10^{-1}$	$10^{-2}$	$10^{-3}$
I, M									
$\text{pK}_{a1}$	4.72	4.87	4.5	4.78	5.27	4.56	5.15	5.52	5.44
$\text{pK}_{a2}$	9.78	9.95	10.17	10.29	9.82	10.03	10.42	10.34	10.24
$\text{D}_s$ , sites/ $\text{nm}^2$	0.864	0.98	2.46	0.984	1.39	1.22	0.242	1.39	1.22

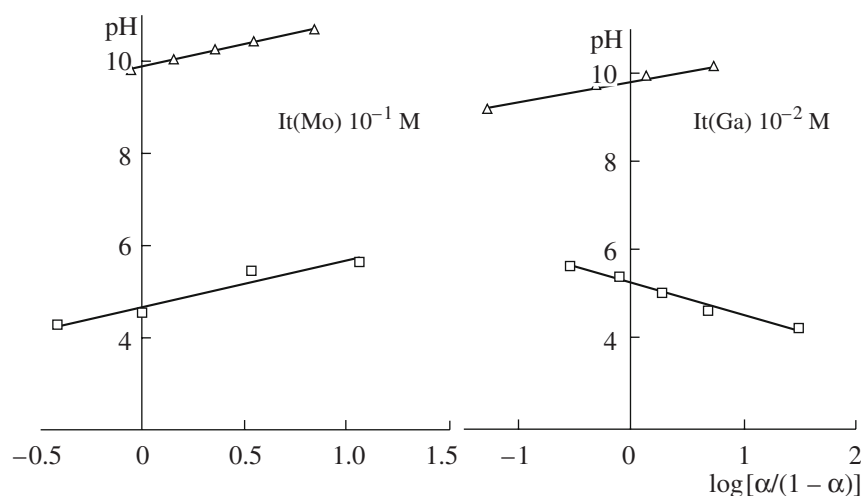
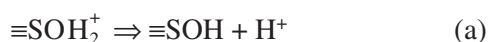


Fig. 4. Plots of the pH vs.  $\log \alpha / (1 - \alpha)$  for It (Mo) and It (Ga) at  $10^{-1}$  M and  $10^{-2}$  M NaCl solutions at ambient temperature.

lution correction; Du [12], by using the two sites two pKa model, for illite from China found  $\text{pKa}_1^{\text{int}} = 4.17$ – $4.44$  and  $\text{pKa}_2^{\text{int}} = 6.35$ – $7.74$ ; and Avena and De Pauli [29] listed for illite  $\text{pKa}_1^{\text{int}} = -3.90$  and  $\text{pKa}_2^{\text{int}} = -7.60$ . Our  $\text{pKa}_1$  values are not significantly different from that reported in [10], but our  $\text{pKa}_2$  values seem to be much higher. The basic character of our complex clay minerals is likely the origin of the shifting of the  $\text{pKa}_2$  values to a more basic region (see the stability pH values in distilled water, Table 4). This discrepancy might be due to the differences in the sources of the sample and/or in the experimental method in agreement with [12].

On the other hand, the one site two pKas model can also be used to describe our titration data since we assume that the illite surface is homogeneous and that two acidic reactions—one protonation and one deprotonation—analogueous to that used in the CCM model (see below) occur at the illite surface (as shown in Eqs. (a) and (b)). It should be pointed out that [13], using this surface protonation model for the illite complex mineral listed, there are two acid–base constants in the neutral and alkaline regions ( $\text{pKa}_1^{\text{int}} = 7.5$  and  $\text{pKa}_2^{\text{int}} = 11.7$ ):



#### Implementation of Surface Complexation Models (SCMs)

The surface complexation models (SCM) were used to describe and interpret the titration behavior of the illite samples.

#### NEM Model

The simplest SCM is the nonelectrostatic model (NEM), whose formulation is similar to the classical adsorption isotherms. It assumes an ideal behavior of the surface species. Thus, the electrical double layer is ignored and the electrostatic terms in the mass law expressions of the surface reactions are excluded [33]. We must emphasize that the NEM has been applied in some studies of surface speciation of kaolinite [7], montmorillonitic clays [34], and glauconite [14]. It assumes that adsorption is a reversible process that can be described by a simple mass action law where the activity coefficients of the surface species remain constant during the experiments. Our approach to describe the behavior of illitic aqueous suspensions is similar to that used by Huertas et al. [7] for kaolinitic samples. We assumed that one protonation–deprotonation reaction occurs at the illite surface, and then the surface site density was estimated by fitting the sections of the potentiometric titration curves using least-square nonlinear regression analysis.

The protonation reaction of a surface site  $>\text{MOH}$  is represented by the following reaction:



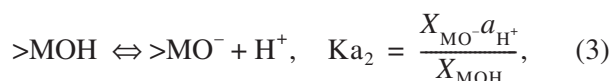
In addition, the equilibrium constant considered the first equilibrium constant of the acid

$$>\text{MOH}_2^+, \text{ is: } K_{a1} = \frac{X_{\text{MOH}} a_{\text{H}^+}}{X_{\text{MOH}_2^+}}, \quad (2)$$

where  $X_i$  denotes the molar fraction of the surface species and  $a_{\text{H}^+}$  is the aqueous proton activity. In the case of deprotonation of the  $>\text{MOH}$  sites, the reaction is given by the following equation:

**Table 6.** Surface site densities  $\theta$  ( $\mu\text{mol}/\text{m}^2$ ) and calculated equilibrium constants for protonation and deprotonation surface reactions for It (Mo), It (Ga), and It (Ha), respectively. Subscript 1 corresponds to protonation reactions and subscript 2 to deprotonation reactions; the equilibrium constants are expressed as the surface dissociation constant of the acid  $>\text{MOH}_2^+$  using the pK scale

I, M	$\theta_1$ ( $\mu\text{mol}/\text{m}^2$ )	pKa <sub>1</sub>	$\theta_2$ ( $\mu\text{mol}/\text{m}^2$ )	pKa2	$\theta$ total ( $\mu\text{mol}/\text{m}^2$ )	PZC = 1/2 (pKa <sub>1</sub> + pKa <sub>2</sub> )	PZC observed
It (Mo)							
0.1	0.89	6.73	0.64	10.32	1.53	8.5	8.5
0.01	0.93	6.82	0.75	9.99	1.67	8.4	
0.001	1.02	6.32	0.68	10.62	1.7	8.46	
It (Ga)							
0.1	6.6	6.43	5.7	10.01	12.3	8.22	9.3
0.01	4.3	5.88	7.08	9.98	11.35	7.93	
0.001	7.2	6.91	3.05	10.67	10.25	8.8	
It (Ha)							
0.1	2.34	6.20	3.46	9.66	5.8	7.93	8.6
0.01	2.81	6.24	2.65	9.71	5.46	7.97	
0.001	3.98	6.59	4.78	9.84	8.76	8.21	



where  $K_{a2\text{app}}$  is the second apparent equilibrium constant of  $>\text{MOH}_2^+$ .

The surface density of any complex  $\theta_i$  is defined as the number of complexes per unit of surface area ( $\mu\text{mol}/\text{m}^2$  or sites/ $\text{nm}^2$ ). If  $\theta_M$  is the total surface density of the  $>M$  site, the surface density of any species can be obtained by

$$\theta_i = \theta_M X_i \quad (\mu\text{mol}/\text{m}^2 \text{ or sites}/\text{nm}^2), \quad (4)$$

where  $\theta_i$  is the surface density of any site. The mass balance for each kind of surface sites will be given by the sum of the positive, neutral, and negative species:

$$\begin{aligned} \theta_M &= \theta_{\text{MOH}_2^+} + \theta_{\text{MOH}} + \theta_{\text{MO}^-} \\ &= \theta_M (X_{\text{MOH}_2^+} + X_{\text{MOH}} + X_{\text{MO}^-}). \end{aligned} \quad (5)$$

On the other hand, one may, as a first approximation, assume that the positive and negative complexes are the only charged species, respectively, below and above the  $\text{pH}_{\text{PZC}}$ . Equation (5) may be simplified as follows:

$$\begin{aligned} \theta_M &\approx \theta_{\text{MOH}_2^+} + \theta_{\text{MOH}} = \theta_M (X_{\text{MOH}_2^+} + X_{\text{MOH}}), \\ \text{pH} &< \text{pH}_{\text{PZC}}, \end{aligned} \quad (6)$$

$$\begin{aligned} \theta_M &\approx \theta_{\text{MOH}} + \theta_{\text{MO}^-} = \theta_M (X_{\text{MOH}} + X_{\text{MO}^-}), \\ \text{pH} &> \text{pH}_{\text{PZC}}. \end{aligned} \quad (7)$$

Rearranging expressions (2) and (3), the molar fractions of the charged sites can be obtained:

$$X_{\text{MOH}_2^+} = \frac{a_{\text{H}^+}}{(K_{a1} + a_{\text{H}^+})} \text{ and } X_{\text{MO}^-} = \frac{K_{a2}}{(K_{a2} + a_{\text{H}^+})}. \quad (8)$$

We have distinctively analyzed each potentiometric titration curve at a given ionic strength in order to determine the surface site density. Then, the apparent equilibrium constants ionization ( $K_{a1\text{app}}$  and  $K_{a2\text{app}}$ ) for each reaction described above were calculated. From these curves, one can assume that, going from acidic to basic conditions, i.e., from positive to negative surface charges, the clay mineral samples of our study undergo two successive reactions. The weak acidic sites ( $\theta_1$ ) release the adsorbed proton at approximately 4–8. At  $\text{pH}_{\text{PZC}}$ , the sites ( $\theta_2$ ) start to deprotonate forming negative complexes up to  $\text{pH} \sim 8.5$ . The main results

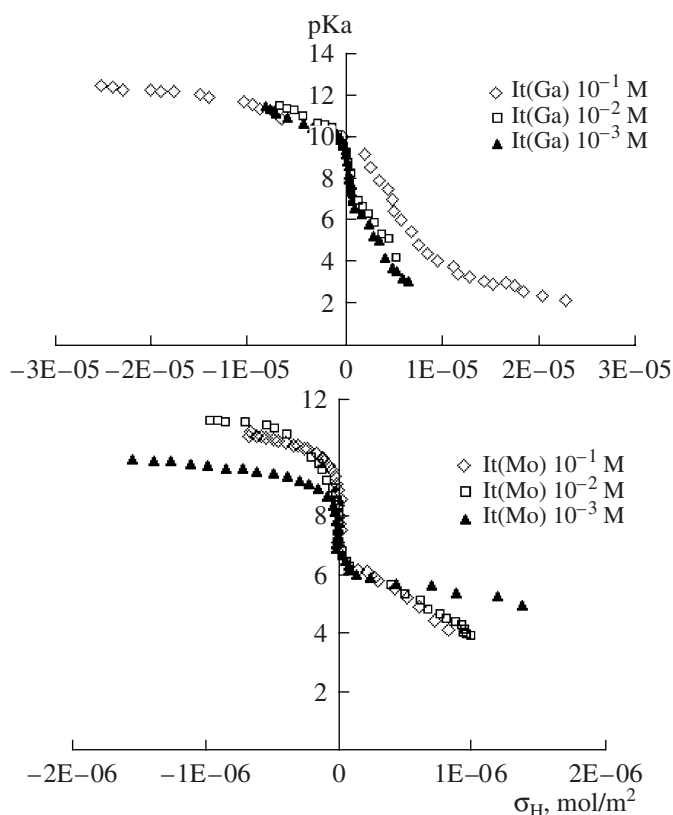


Fig. 5. Plots of pKa vs.  $\sigma_H$  for It (Ga) and It (Ha), respectively, at different ionic strengths and ambient temperature.

concerning the surface site densities and calculated apparent equilibrium constants for the three-illitic clay minerals are given in Table 6.

#### Constant Capacitance Model

The constant capacitance model was also used by some authors for complex clay minerals such as illite [12], kaolinite [7], and glauconite to model titration data and to compare NEM calculations with CCM simulations [14]. The model assumes that the EDL at the mineral–water interface behaves as a flat capacitor whose capacitance  $C$  is the proportionality constant ( $F/m^2$ ) between the charge  $\sigma_H$  (Coulombs/ $m^2$ ) and the surface potential  $\psi$  (volt):

$$\begin{aligned}\sigma_H &= C\psi, \\ K_{a1}^{int} &= K_{a1}e^{(-F\psi)/RT}, \\ K_{a2}^{int} &= K_{a2}e^{(-F\psi)/RT},\end{aligned}$$

where  $F$  is the Faraday constant (coulombs/mol), and  $R$  and  $T$  are the gas constant (cal/ $K^\circ$  mol) and temperature (K), respectively.

The intrinsic constants for the surface groups were calculated by extrapolating the linear regression curve pKa vs.  $\sigma_H$  to zero surface charge (Fig. 5). The total site

density was estimated by extrapolating the sections of the titration curves to low or high pH values. The intrinsic equilibrium constants of the illite samples were computed from the potentiometric titration data by employing a polynomial of the fourth degree equation (Table 7).

Concerning the determination of the capacity values, no methods exist for independently measuring the electrical double layer capacitance parameters for complex clay water systems. Some researchers have suggested that values for  $C$  can be obtained from titration data [1, 5]. Since no methods are currently available for measuring interfacial capacitance, we have also used the extrapolation method to determine the capacity values.

The  $pK_{a1}^{int}$  intrinsic values are in the range of 5.78–7.6, and the  $pK_{a2}^{int}$  are in the range of 9.25–10.43. Similarly to the surface equilibrium constants determined by NEM, we concluded that the inclusion of the electrostatic term does not improve the description of the adsorption reactions much, in agreement with [7, 14, 17].

#### Triple Layer Model (TLM)

The intrinsic acidity constants  $pK_{a1}^{int}$  and  $pK_{a2}^{int}$  of the illite samples were also computed from the potentiometric titration data by employing a polynomial of the fourth degree equation by using the triple layer model (TLM) described in [1, 35] in the forms

$$\begin{aligned}pK_{a1}^{int} &= pH + \log[\alpha^+/1 - \alpha^+] + [F\psi_0/2.3RT], \\ pK_{a2}^{int} &= pH - \log[\alpha^-/1 - \alpha^-] + [F\psi_0/2.3RT],\end{aligned}$$

where  $\alpha^+(\sigma_H^+/Ds)$  and  $\alpha^-(\sigma_H^-/Ds)$ , and  $\sigma_H^+$  and  $\sigma_H^-$  represent the surface charge densities ( $\mu\text{mol}/m^2$ ) below and above the PZC of the sample, respectively;  $Ds$  is the total density of sites determined by the extrapolation method;  $F$  is the Faraday constant ( $C \text{ mol}^{-1}$ );  $\psi_0$  is the potential mean in the plane of the surface; and  $T$  is the absolute temperature (K).

The plots of the  $pH + \log[\alpha^+/1 - \alpha^+]$  versus  $\alpha^+$  and the  $pH - \log[\alpha^-/1 - \alpha^-]$  versus  $\alpha^-$  were extrapolated to  $\alpha^\pm = 0$  using MS EXCEL 5 (Fig. 6). The values of the intrinsic acidity constants thus obtained are listed in Table 8 and are comparable to the values reported for other complex clay minerals [14].

The TLM model gives  $pK_{a1}^{int}$  values in the range of 4.56–6.67, whereas, for  $pK_{a2}^{int}$ , it gives values in the range 10.01–10.84. In general, as is seen, the NEM, CCM, and TLM models have given approximately the same surface ionization constants. Similarly to the pKas values determined using our model approach, we



**Table 7.** Surface site densities  $\theta$  ( $\mu\text{mol}/\text{m}^2$ ) and intrinsic equilibrium constants for protonation and deprotonation surface reactions calculated according to the CCM for It (Mo), It (Ga), and It (Ha), respectively. The capacitance ( $C$ ) is in  $\text{F}/\text{m}^2$ 

It (Mo)

I, M	$\theta_1$ ( $\mu\text{mol}/\text{m}^2$ )	$\text{pK}_{\text{a}_1}^{\text{int}}$	$C$ ( $\text{F}/\text{m}^2$ )	$\theta_2$ ( $\mu\text{mol}/\text{m}^2$ )	$\text{pK}_{\text{a}_2}^{\text{int}}$	$C$ ( $\text{F}/\text{m}^2$ )	$\theta_{\text{total}}$ ( $\mu\text{mol}/\text{m}^2$ )
0.1	1.23	6.69	0.54	1.21	9.96	1.3	2.44
0.01	1.2	6.56	0.53	1.14	9.71	2.71	2.34
0.001	1.56	6	2.086	1.63	9.25	3.76	3.19

It (Ga)

I, M	$\theta_1$ ( $\mu\text{mol}/\text{m}^2$ )	$\text{pK}_{\text{a}_1}^{\text{int}}$	$C$ ( $\text{F}/\text{m}^2$ )	$\theta_2$ ( $\mu\text{mol}/\text{m}^2$ )	$\text{pK}_{\text{a}_2}^{\text{int}}$	$C$ ( $\text{F}/\text{m}^2$ )	$\theta_{\text{total}}$ ( $\mu\text{mol}/\text{m}^2$ )
0.1	10.6	5.78	8.35	8.09	10.37	11.76	18.69
0.01	9.74	6.7	5.32	2.66	10.43	14.98	12.4
0.001	9.32	6.46	4.9	4.09	10.26	13.32	13.41

It (Ha)

I, M	$\theta_1$ ( $\mu\text{mol}/\text{m}^2$ )	$\text{pK}_{\text{a}_1}^{\text{int}}$	$C$ ( $\text{F}/\text{m}^2$ )	$\theta_2$ ( $\mu\text{mol}/\text{m}^2$ )	$\text{pK}_{\text{a}_2}^{\text{int}}$	$C$ ( $\text{F}/\text{m}^2$ )	$\theta_{\text{total}}$ ( $\mu\text{mol}/\text{m}^2$ )
0.1	3.67	6.11	3.15	4.53	9.33	3.59	8.2
0.01	3.31	7.6	2.53	3.45	10.04	7.32	6.76
0.001	5.08	7.06	2.33	7.2	9.95	8.97	12.28

**Table 8.** Surface ionization constants for the illite samples at different NaCl solutions

	It (Mo)			It (Ga)			It (Ha)		
I	$10^{-1}$ M	$10^{-2}$ M	$10^{-3}$ M	$10^{-1}$ M	$10^{-2}$ M	$10^{-3}$ M	$10^{-1}$ M	$10^{-2}$ M	$10^{-3}$ M
$\text{pK}_{\text{a}_1}^{\text{int}}$	4.57	4.74	4.63	5.8	6	5.82	6.15	5.57	6.67
$\text{pK}_{\text{a}_2}^{\text{int}}$	10.31	10.59	10.46	10.82	10.84	10.80	10.68	10.64	10.01

can observe that the SCMs described above give differences in the pKas values; i.e., depending on the methodology chosen, small differences in the values of the model parameters for a given SCM and given titration data are obtained. We think that the major reason for the differences in the observed surface ionization constants is mainly due to the manner in which the extrapolation method was created involving, in some cases, extrapo-

lation to large pKas values. This remark is supported by Hayes et al. [1], who reported that the extrapolation procedures cannot be conveniently used to produce a unique set of surface constants since there are no objective methods to determine which range of titration data should be used in the extrapolations. Furthermore, some authors reported that the accuracy of the determination of the surface ionization constants using potenti-

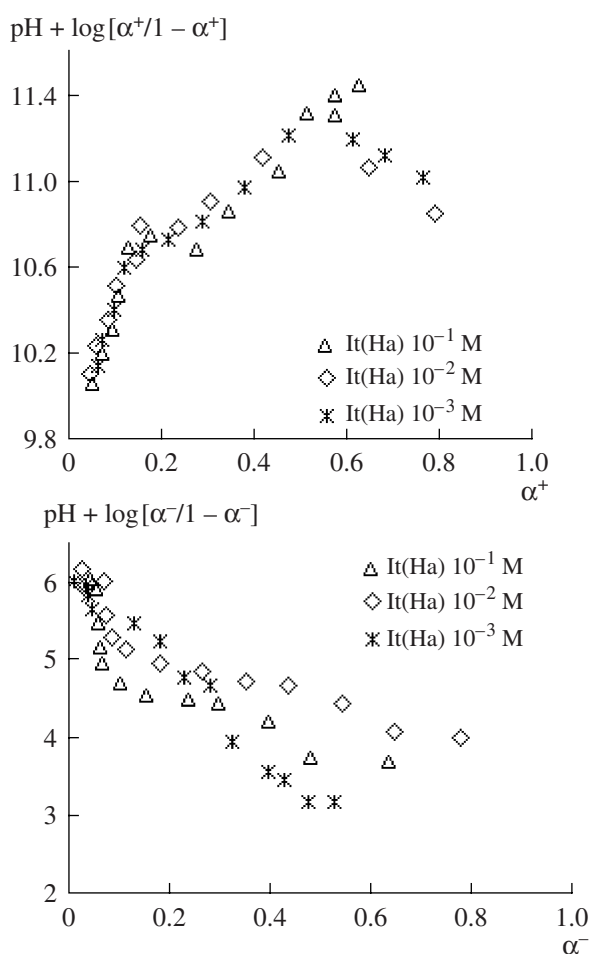


**Fig. 6.** Plots of the  $\text{pH} + \log[\alpha^+/1 - \alpha^+]$  versus  $\alpha^+$  and the  $\text{pH} - \log[\alpha^-/1 - \alpha^-]$  versus  $\alpha^-$  for It (Ha) in different NaCl solutions at ambient temperature.

ometric titration data is rather poor because the extrapolated smooth curves tend asymptotically to vertical lines (the  $\sigma\text{H}$  vs.  $\text{pH}$  curves) [5]. Thus, any inexactitude in tracing of the curves can give large differences in the surface ionization constant values. We also think that using the proton binding affinity distribution method [36] in order to detect new acidic centers that have not been identified by the regression method should complete this study. Although difficulties concerning the extrapolation technique exist, it remains one of the most practical methods to access  $\text{pK}_a$ s values.

## CONCLUSIONS

Our systematic study of the acid–base reactions at the illite water interface indicates that the surface charge of illite in inert electrolyte solutions involves two kinds of sites: weak acidic sites at  $\text{pH}$  4–8 groups and weak basic sites at  $\text{pH} \sim 8.5$  of the crystal edges. The protonation ( $\text{AlOH}$  groups) and deprotonation

( $\text{SiOH}$  groups) at these sites occur at different  $\text{pH}$  ranges; thus, each site is responsible for the surface charge under a given  $\text{pH}$  condition. The overall  $\text{pH}_{\text{ZPC}}$  ( $\sim 8.5$ – $9.2$ ) determined by the Gran method or fast titration technique is the result of the balance between positive and negative charges irrespective of the nature of the sites. From the parameters derived using the Gran plot method, surface ionization constants were determined according to an algorithm of the two sites two  $\text{pK}_a$ s model. For the illite samples, the  $\text{pK}_{a1}$  values are in the range of 4.5–5.52 and the  $\text{pK}_{a2}$  values are in the range of 9.78–10.42. SCMs (CCM, TLM) were implemented for our titration data in order to confirm these surface constants' ionization. This revealed that, according to the methodology chosen, some differences in the  $\text{pK}_a$ s values appear, which are very likely due to errors made in the extrapolation procedure. Whatever the inconvenience of this regression method, we can take it into consideration as a solution for determining the acid–base characteristics of complex illitic samples.

## REFERENCES

- Hayes, K.F., Redden, G., Ela, W., and Leckie, J.O., Surface Complexation Models: An Evaluation of Model Parameter Estimation Using FITEQL and Oxide Mineral Titration Data, *J. Colloid Interface Sci.*, 1991, p. 142.
- Davis, J.A. and Leckie, J.O., Surface Ionization and Complexation at the Oxide/Water Interface, *J. Colloid Interface Sci.*, 1978, vol. 67, nos. 1, 15.
- Sverjensky, D., Prediction of Surface Charge on Oxides in Salt Solutions: Revisions for 1:1 ( $\text{M} + \text{L}^-$ ) Electrolytes, *Geochim. Cosmochim. Acta*, 2005, vol. 69, p. 225.
- Mustapha, S., Dilara, B., Nargis, K., Naeem, A., and Shahida, P., Surface Properties of the Mixed Oxides of Iron and Silica, *Colloids Surf., A*, 2002, vol. 205, pp. 273–282.
- Sprycha, R., Electrical Double Layer at Alumina/Electrolyte Interface, *J. Colloid Interface Sci.*, 1989, vol. 127, p. 1.
- Schindler, P.W. and Stumm, W., *Aquatic Surface Chemistry*, Stumm, W., Ed., New York: Wiley, 1987.
- Huertas, J.F., Lei Chou, and Wollast, R., Mechanism of Kaolinite Dissolution at Room Temperature and Pressure, part 1: Surface speciation, *Geochim. Cosmochim. Acta*, 1998, vol. 62, pp. 417–434.
- Stadler, M. and Schindler, P.W., Modeling of  $\text{H}^+$  and  $\text{Cu}^{2+}$  Adsorption on Calcium-Montmorillonite, *Clays Clay Miner.*, 1993, vol. 41, pp. 288–296.
- Stadler, M. and Schindler, P.W., The Effect of Dissolved Ligands on the Sorption of  $\text{Cu(II)}$  by Ca-Montmorillonite, *Clays Clay Miner.*, 1994, vol. 42, pp. 148–160.
- Nagy, N.M. and Konya, J., Acid-Base Properties of Bentonite Rocks with Different Origins, *J. Colloid Interface Sci.*, 2006, vol. 295, pp. 173–180.
- Du, Q., Sun, Z., Forsling, W., and Tang, H., Adsorption of Copper at Aqueous Illite Surfaces, *J. Colloid Interface Sci.*, A, 1997, vol. 187, pp. 232–242.

12. Du, Q., Sun, Z., Forsling, W., and Tang, H., Acid-Base Properties of Aqueous Illite Surface, Ser. B, *J. Colloid Interface Sci.*, 1997, vol. 187, pp. 221–231.
13. Liu, W., Sun, Z., Forsling, W., Du, Q., and Tang, H., A Comparative Study of Surface Acid-Base Characteristics of Natural Illites from Different Origins, *J. Colloid Interface Sci.*, 1999, vol. 219, pp. 48–61.
14. Lu, W. and Smith, E.H., Modeling Potentiometric Behavior of Glauconite, *Geochim. Cosmochim. Acta*, 1996, vol. 60, pp. 3363–3373.
15. Motta, M.M. and Miranda, C.F., Molybdate Adsorption on Kaolinite, Montmorillonite, and Illite: Constant Capacitance Modeling, *Soil Sci. Soc. Am. J.*, 1989, vol. 53, pp. 380–385.
16. Wieland, E. and Stumm, W., Dissolution Kinetics of Kaolinite in Acidic Aqueous Solution at 25°C, *Geochim. Cosmochim. Acta*, 1992, vol. 56, pp. 3339–3355.
17. Majone, M., Papini, M.P., and Rolle, E., Modeling Lead Adsorption on Clays by Models with and without Electrostatic Term, *J. Colloid Interface Sci.*, 1996, vol. 183, pp. 412–425.
18. Katari, K. and Tauxe, L., Effect of pH and Salinity on the Intensity of Magnetisation in Redeposited Sediments, *Earth Planetary Sci. Lett.*, 2000, vol. 181, pp. 489–496.
19. Keren and Sparks, D.L., The Role of Edge Surfaces in Flocculation of 2:1 Clay Minerals R, *Soil. Sci. Soc. Am. J.*, 1995, vol. 59, pp. 430–435.
20. *Van Olphen and Introduction to Clay Colloid Chemistry*, New York: Interscience Publishers, 1963.
21. Boissay, S., Comparaison des Méthodes de Détermination des Points de Charge Nulle, *Thesis*, France: Département Minéralurgie du Bureau de Recherche Géologique et Minières à Orléans, 1984.
22. Kriaa, A., Hamdi, N., and Srasra, E., Determination of Point of Zero Charge of Tunisian Kaolinite by Potentiometric Titration and Mass Titration, *J. Chin. Chem. Soc.*, 2008, vol. 55, no. 1, pp. 35–62.
23. Chorover, J. and Sposito, G., Surface Charge Characteristics of Kaolinitic Tropical Soils, *Geochim. Cosmochim. Acta*, 1995, vol. 59, pp. 875–884.
24. Citeau, L., Etude des Colloïdes Naturels Présents Dans les Eaux Gravitaires de Sol Contaminées: Relation Entre Nature des Colloïdes et Reactivités vis à vis des Métaux (Zn, Cd, Pb, Cu), *Thesis*, Paris-Grignon: Institut National d'Agronomie, 2004.
25. James, R.O. and Parks, G.A., *Surface and Colloids Science*, Matijevic, E., Ed., New York: Plenum Press, 1982, vol. 12, p. 119.
26. James, R.O., Davis, J.A., and Leckie, J.O., Computer Simulation of the Conductometric and Potentiometric Titration of the Surface Groups on Ionizable Latexes, *J. Colloid Interface Sci.*, 1978, vol. 65, p. 331.
27. Schroth, B.L. and Sposito, G., Surface Charge Properties of Kaolinite, *Clays Clay Miner.*, 1997, vol. 45, p. 85.
28. Duc, M., Gaboriaud, F., and Thomas, F., Sensitivity of the Acid-Base Properties of Clays to the Methods of Preparation and Measurement 2: Evidence from Continuous Potentiometric Titration, *J. Colloid Interface Sci.*, 2005, vol. 289, pp. 148–156.
29. Avena, M.J. and de Pauli, C.P., Proton Adsorption and Electrokinetics of an Argentinean Montmorillonite, *J. Colloid Interface Sci.*, 1998, vol. 202, p. 195.
30. Tombacz, E. and Szekeres, M., Colloidal Behavior of Aqueous Montmorillonite Suspensions: the Specific Role of pH in the Presence of Indifferent Electrolytes, *Appl. Clay Sci.*, 2004, vol. 27, pp. 75–94.
31. Tombacz, E., Szekeres, M., and Klumpp, E., Interfacial Acid-Base Reactions of Aluminum Oxides Dispersed in Aqueous Electrolyte Solutions, vol. 2: Calorimetric Study on Ionization of Surface Sites, *Langmuir*, 2001, vol. 17, p. 1420–1425.
32. Hendershot, W.H. and Lavkulich, L.M., Effect of Sesquioxide Coatings on Surface Charge of Standard Mineral and Samples, *Soil Sci. Soc. Am. J.*, 1983, vol. 47, p. 1252.
33. Davis, J.A. and Kent, D.B., Surface Complexation Modeling in Aqueous Geochemistry. In *Mineral-Water Interface Geochemistry*, Hochella, M.F., Jr. and White, A.F., Ed., *Miner. Soc. Am.*, 1990, pp. 177–260.
34. Kriaa, A., Hamdi, N., and Srasra, E., Acid Base Characteristics of Montmorillonite and Montmorillonitic Clays, *Russ. J. Electrochem.*, 2007, vol. 43, no. 2, pp. 167–177.
35. Davis, J.A., James R.O., and Leckie, J.O., Surface Ionization and Complexation at the Oxide/Water Interface, vol. I: Computation of Electrical Double Layer Properties in Simple Electrolytes, *J. Colloid Interface Sci.*, 1977, vol. 63, p. 480.
36. Janek, M. and Lagaly, G., Proton Saturation and Rheological Properties of Smectite Dispersions, *Appl. Clay Sci.*, 2001, vol. 19, pp. 121–130.

---

ELECTRICAL PROCESSES  
IN ENGINEERING AND CHEMISTRY

---

## Electrothermopolarization Influence upon the Structure and Properties of a Composition on the Basis of Polyethylene and $\text{Co}(\text{AlO}_2)_2$

M. A. Ramazanov<sup>a</sup>, A. S. Guseinova<sup>b</sup>, and S. I. Mukhtieva<sup>b</sup>

*a* Baku State University, ul. Z. Khalilov 23, Baku, AZ-1148 Republic of Azerbaijan

*e-mail:* mamed-r43@rambler.ru

*b* Institute of Physics, National Academy of Sciences of Azerbaijan,  
av. G. Dzhevaid 33, Baku, AZ-1143 Republic of Azerbaijan

Received December 24, 2007

**Abstract**—The influence of electrothermopolarization on the structure and properties (electret, strength) of a composition on the basis of polyethylene and a low-molecular dye  $\text{Co}(\text{AlO}_2)_2$  was investigated. It was experimentally established that the additive  $\text{Co}(\text{AlO}_2)_2$  changes the polyethylene structure. As a result, the electret properties of the composition change. Correlation of the strength properties with the changes of the degree of the crystallinity of the polyethylene was observed.

**DOI:** 10.3103/S1068375508030101

Polymers and the composites on their basis, being used in space apparatuses, in nuclear reactors as dielectric materials, in detection devices, and in energy converters as electric active elements, undergo multiple affects. It is well known that the polymers and compositions on their basis have electret properties with a space-charge polarization caused by the applied external direct electric field at a relatively high temperature. Earlier, it was found out by us that the electrothermopolarization changes the polymers and composites charge states, which leads to the change of their strength properties [1–3]. It is also known that the polymer compositions acquire electret properties after electrothermal polarization. In the utilization process, the elements of polymer compositions, which have electret properties, are being exposed to a long-term external action. In this case, the compositions that are being used may affect their structures and the electret properties.

It is known that the electric charges in the process of electrothermal polarization are accumulated on the phases interface and in the heterogeneities. The charge accumulation on the phase interface changes the interphase interactions, which may lead to the change of the dielectric and strength properties of the composition. The relaxation of the accumulated charge in the composites can occur due to external and internal factors. It may occur spontaneously and without any control in the utilization or storage processes of the articles.

The lack of a common opinion regarding the influence of the charge being accumulated in the polarization process upon the properties (the dielectric strength, etc.) and structures has aroused high interest in the study of the polarization influence upon these proper-

ties, which, in turn, create the electret state of the composition.

In the present paper, there are presented the results of investigation of electric thermal polarization upon the structures and properties (the electret and strength) of composition on the basis of polyethylene and the low-molecular dye  $\text{Co}(\text{AlO}_2)_2$ . The concentration of  $\text{Co}(\text{AlO}_2)_2$  varied in the range of 0–2% (vol.). The introduction of the additives creates in polyethylene new traps for the electric charge, and this may provide for an increase of the charge surface density and the life time.

The composition of polyethylene (PE) +  $\text{Co}(\text{AlO}_2)_2$  was obtained from a solution of PE by means of mixing the PE solution and  $\text{Co}(\text{AlO}_2)_2$  with the subsequent solvent removal. The composite production was performed by the method of hot pressing at the polyethylene melting temperature and a pressure of 15 MPa for 10 min with subsequent cooling to room temperature under pressure.

The specimens were polarized by the method of polarization [1].

The polymer compositions were exposed to the electric thermal polarization in the temperature range of  $T_m = 353\text{--}373$  K with an electric field intensity of  $E = (3\text{--}10) \times 10^6$  V/m for 1 h with subsequent cooling to room temperature under the electric field action.

The surface density of the electret charges  $Q_{el}$  was studied by the induction method [4] with respect to the storage time.

The strength characteristics of the composition were determined at a temperature of 293 K according to [5].

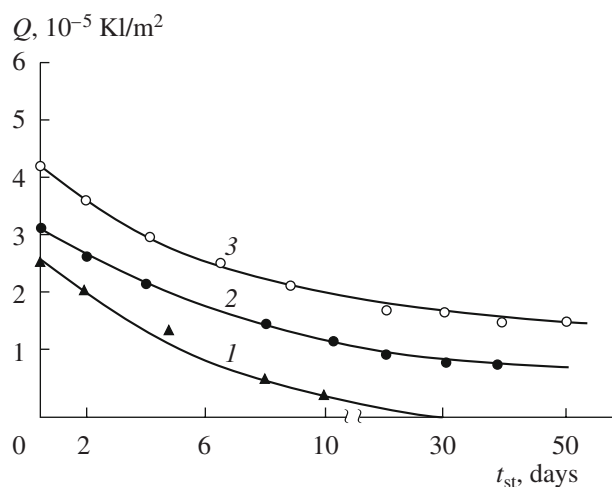


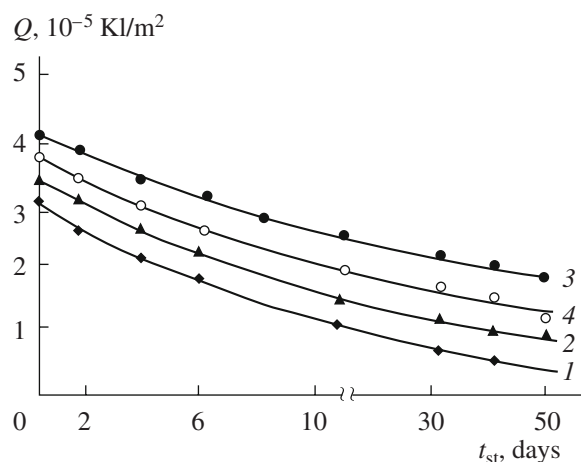
**Fig. 1.** The dependence of the surface density of the electret charges  $Q$  on the storage time of the composition PE +  $\text{Co}(\text{AlO}_2)_2$ . 1—PE; 2—PE + 0.5% vol.  $\text{Co}(\text{AlO}_2)_2$ ; 3—PE + 1% vol.  $\text{Co}(\text{AlO}_2)_2$ .

The dielectric permeability and the tangent angle of the dielectric wastes were measured by means of an automatic E8-4 bridge at a frequency of 1 kHz. IR spectroscopy was used in order to estimate the development of the oxidative-destructive processes in the polymers at  $\text{Co}(\text{AlO}_2)_2$  introduction. The investigations were carried out with a Specord M-8 infrared spectrophotometer in the frequency range of  $700\text{--}1700\text{ cm}^{-1}$ .

Figure 1 presents the dependences of the  $Q$  electret charges surface density upon the time of their storage  $t_{\text{st}}$  of PE +  $\text{Co}(\text{AlO}_2)_2$  at various dye  $\text{Co}(\text{AlO}_2)_2$  content in the PE. In the figure, one can see that, with the increase of the  $\text{Co}(\text{AlO}_2)_2$  content in the PE, the surface density of the electret charges and the storage time measured by the induction method attain the maximum value at the increase of the volume content of  $\text{Co}(\text{AlO}_2)_2$ .

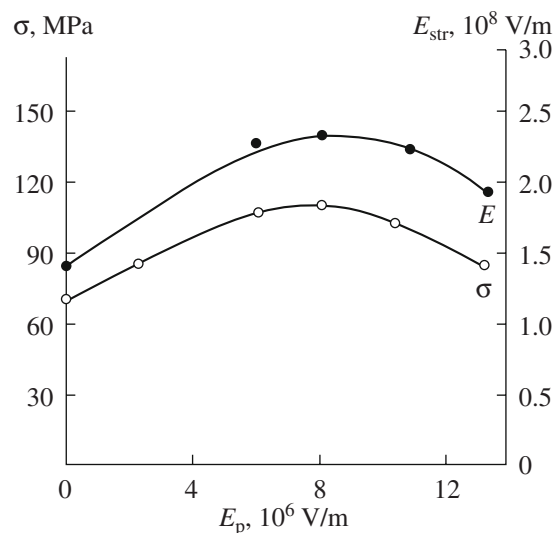
The dependence of the surface density of the electret charges  $Q$  upon the storage time of the polymer compositions PE + 1%  $\text{Co}(\text{AlO}_2)_2$ , being exposed to the electrothermopolarization at various  $E_p$  and  $T_p = 353\text{ K}$ , is presented in Fig. 2. It is shown that the surface density of electret charges and storage time depend on the polarization conditions, i.e.  $Q$  on  $t_{\text{st}}$  obtain their maximum values at  $E_p = 8 \times 10^6\text{ V/m}$ . It is evident from Fig. 2 that as the polarization field strength increases to  $E_p = 7 \times 10^6\text{ V/m}$ , the polarization processes in the composition improve, and after  $E_p > 8 \times 10^6\text{ V/m}$ , it seems likely that the concentrations of space charges increase, which leads to worsening the electret properties.

Figure 3 shows the dependence of the electric  $E_{\text{str}}$  and mechanical  $\sigma$  strength of the composition PE + 1% vol.  $\text{Co}(\text{AlO}_2)_2$  polarized at the temperature  $T = 353\text{ K}$  upon the polarization field intensity. It is seen from the figure that, with the increase of the intensity of the polarization electric field  $E_p$ , the electric and mechanic



**Fig. 2.** The dependence of the surface density of the electret charges  $Q$  on the storage time of the composition PE + 1%  $\text{Co}(\text{AlO}_2)_2$  electrothermopolarization at various  $E_p$  and the temperature  $T_p = 353\text{ K}$ .  $E_p, 10^6\text{ V/m}$ : 1—3; 2—5; 3—7; 4—10.

strengths of the studied specimens grow, attain their maximum at  $E_p = 7 \times 10^6\text{ V/m}$ , and then there occurs the reduction of the values of  $\sigma$  and  $E_{\text{str}}$ . In our opinion, the change of the strength properties of the above compositions with the increase of  $E_p$  of the electrothermopolarization up to  $E_p = 7 \times 10^6\text{ V/m}$  is connected with the interphase strength structure ordering under the action of the polarization charges accumulated in the polarization process. The further decrease of  $E_p$  and  $\sigma$  from  $E_p$ , in our opinion, is caused by the charge scattering in the volume of the composition, which leads to the electroconductivity increasing. At the electroconductivity



**Fig. 3.** The dependence of the electric and mechanic strength of the composition PE + 1% vol.  $\text{Co}(\text{AlO}_2)_2$  polarized at the temperature  $T_p = 353\text{ K}$  on the polarization field intensity.



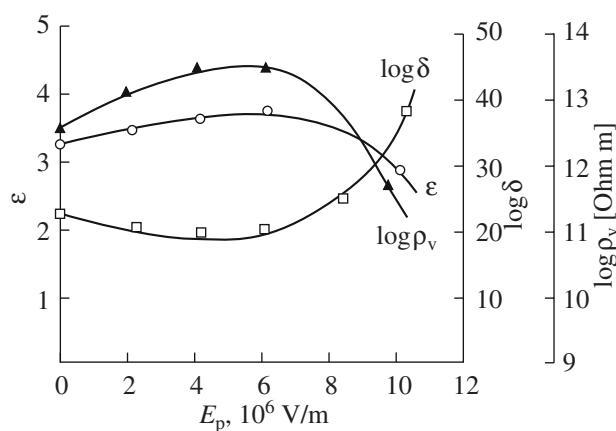


**Fig. 4.** The dependences of the dielectric permeability, the tangent of the angle of the dielectric waste, and the logarithm of the resistivity of the composition PE + 1% vol.  $\text{Co}(\text{AlO}_2)_2$  polarized at the temperature  $T_p = 353$  K on the polarization field intensity.

increase, the electric strength of the composition reduces.

Figure 4 depicts the dependences of the dielectric permeability  $\epsilon$ , the tangent of the angle of the dielectric wastes  $\tan \delta$ , and the logarithm of the resistivity  $\log \rho_v$

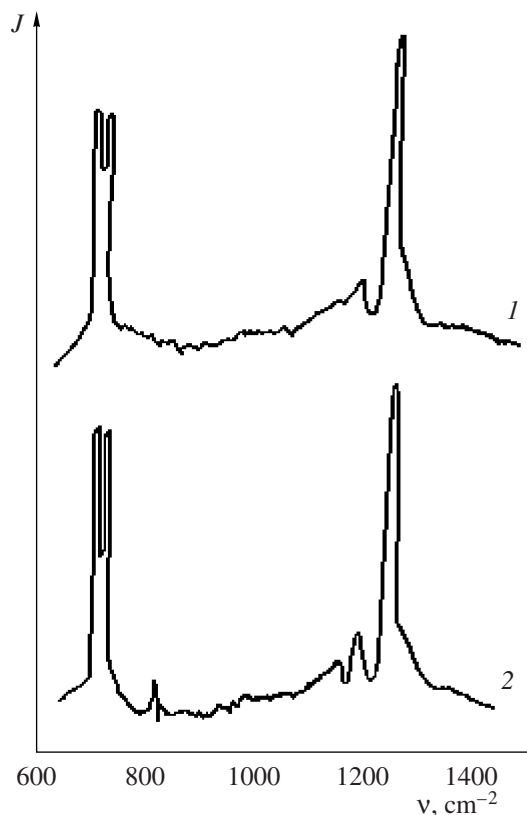


**Fig. 5.** IR spectra: 1—PE, 2—compositions PE + 1% vol.  $\text{Co}(\text{AlO}_2)_2$ .

of the composition PE + 1% vol.  $\text{Co}(\text{AlO}_2)_2$  upon the electric field intensity upon whose action the polarization was performed. It is evident from Fig. 3 and Fig. 4 that there is a correlation between the strengthening properties' mechanisms of  $\epsilon$ ,  $\tan \delta$ , and  $\log \rho_v$ . Such a dependence of  $E_{\text{str}}$ ,  $\epsilon$ ,  $\tan \delta$ , and  $\log \rho_v$  upon the electrothermopolarization intensity can be explained by the change of the molecular structure of the polymer matrix and the thickness of the interphase layer of the composition components.

Figure 5 presents the IR spectra of the specimens of PE + 1% vol.  $\text{Co}(\text{AlO}_2)_2$  composition (not polarized and polarized) at  $E_p = 7 \times 10^6$  V/m,  $T_p = 353$  K for 1 hour. The IR spectra show that there occur changes in the absorption spectrum, particularly, in the region of the wave length of 850 and 720  $\text{cm}^{-1}$ . There was observed an increase of the bands with respect to the polarization field intensity at 720 and 731  $\text{cm}^{-1}$ ; i.e., there occurred an activation of the fluctuation of  $\gamma_2$  ( $\text{CH}_2$ ), especially at 720  $\text{cm}^{-1}$ .

In paper [6], for the determination of the crystalline degree, there was used a doublet of the bands in the range of 720–731  $\text{cm}^{-1}$ . The absorption at 720  $\text{cm}^{-1}$  refers to both the amorphous and crystalline region. The value of the ratio of the integral absorption of both components of the doublet characterizes the degree of the polymer crystallinity.

Figure 6 displays the dependences of the crystallinity degree on the field intensity and polarization for PE and PE + 1% vol.  $\text{Co}(\text{AlO}_2)_2$ . It is clear from the figure that the degree of crystallinity increases with respect to the field intensity up to  $5 \times 10^6$  V/m, and then a decrease is registered. For the composition PE + 1% vol.  $\text{Co}(\text{AlO}_2)_2$ , the crystallinity degree increases with respect to the polarization field intensity up to  $7 \times 10^6$  V/m, and then the absorption is detected. The distinction of the influence of the polarization field inten-

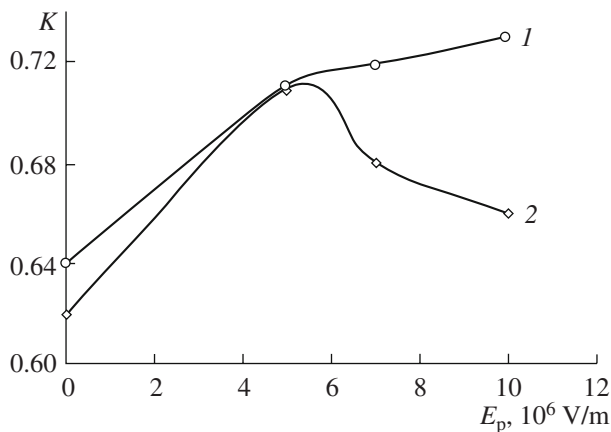


**Fig. 6.** The dependences of the crystallinity degree of the composition PE + 1% vol.  $\text{Co}(\text{AlO}_2)_2$  polarized at the temperature  $T_p = 353$  K on the field intensity and the polarization for the following: 1—PE + 1% vol.  $\text{Co}(\text{AlO}_2)_2$ ; 2—PE.

sity upon the IR spectra and the degrees of crystallinity for the pure PE and PE + 1% vol.  $\text{Co}(\text{AlO}_2)_2$  shows that the low-molecular additive  $\text{Co}(\text{AlO}_2)_2$  causes the polymer matrix structure to change, which changes the electret properties of the composition on the basis of PE + 1% vol.  $\text{Co}(\text{AlO}_2)_2$ .

Thus, it follows from the above experimental results that the additive  $\text{Co}(\text{AlO}_2)_2$  changes the polyethylene structure, which leads to the change of the electret properties and the correlation of the strength properties with the change of the degree of the polyethylene crystallinity.

#### REFERENCES

1. Ramazanov, M.A., Abasov, S.A., and Mustafaev, Z.E., The Influence of Electrothermopolarization on the Strength Properties of the Composition on the Basis of Polymer-Piezoelectric, *Novye Tekhnol. 21-yi Vek*, 2001, no. 6, pp. 26–29.
2. Ramazanov, M.A., Abasov, S.A., Bedirkhanova, S.Sh., and Mustafaev, Z.E., Influence of Charge State on Strength Properties of Composition on the Basis of Polypropylene and Polyethylene, *Plast. Massy*, 2004, no. 2, pp. 22–24.
3. Ramazanov, M.A., Ibragimov, Kh.S., Abasov, S.A., and Gasanov, A.N., Influence of Preliminary Electroprocessing on Charge State and Strength Properties of Composition on the Basis of Polyethylene and Piezo-Ceramics, *Elektron. Obrab. Mater.*, 2005, no. 4, pp. 57–61.
4. Lusheikin, G.A., *Polimernye elektrety* (Polymer Electrets), Moscow: 1984.
5. Magerramov, A.M., *Srukturnoe i radiatsionnoe modifitsirovanie elektretnykh, p'ezoelektricheskikh svoistv polimernykh kompozitov* (Structural and Radiational Modification of Eletret, Piezoelectric Properties of Polymer Composites), Baku: 2001.
6. Dekhany, I., Dants, P., Kimmer, V., and Shmol'ke, P., *Infrakrasnaya spektroskopiya polimerov* (Infrared Spectrometry of Polymers), Moscow: 1976.

## ELECTRICAL PROCESSES IN ENGINEERING AND CHEMISTRY

# Activation of Soldered Connections in the Process of Formation Using the Energy of Ultrasonic and Electric Fields

V. L. Lanin

*State University of Informatics and Radioelectronics of Belarus,  
ul. P. Brovki 6, Minsk, 220013 Republic of Belarus  
e-mail: Vlanin@bsuir.unibel.by  
Received December 28, 2007*

**Abstract**—Modeling and experimental research of diffusion processes during formation of soldered connections under the influence of energy of ultrasonic and electric fields were performed. It was found that the concentration of diffusion elements increased in the interface depth by 30–45%; owing to this, the durability of the connections with difficult-to-solder metals increased by a factor of 1.25–1.5.

**DOI:** 10.3103/S1068375508030113

The kinetics of processes that occur during formation of soldered connections, such as energy consumption, diffusion, the physical and chemical interaction of components, etc., become more complicated under the combined action of the energy of ultrasonic (US) and electric fields. Activation using the energy of an ultrasonic field is an effective process, because mechanical elastic vibrations with frequencies of 18–70 kHz and intensity of 0.1–1.0 MW/m<sup>2</sup> intensify the majority of physicochemical processes: wetting, spreading, capillary flow solder, and solder diffusion into soldered materials [1]. The action of the electric field energy increases the thermal energy of the system. This allows reaching the soldering temperature at a greater rate; facilitates the solder spreading; and as a result, improves the quality of the connections [2].

However, the physical nature of the combined action of the energy of ultrasonic and electric fields on the processes of wetting and diffusion is not completely understood. According to the Frenkel hypothesis, the surface energy of melts was treated as the electrostatic energy of a double electric layer that appears on the metal surface. Because the energy of the electrons of the atoms in the outer metal layer differs from the energy of the electrons of the bulk atoms, a kind of a capacitor forms at the melt–solid body interface, which defines the value of the surface energy and the surface tension at the interface. From this point of view, the surface tension of the melted metal can be estimated as the electric energy of the capacitor referring to the unit of area. For a metal with valency  $z$ , the electric field between the plates separated by the space  $l$  amounts to  $E = 4\pi ze/R^2$ , where  $e$  is the electron charge. Multiplying  $E$  by the

capacitor thickness equal to  $R$ , we obtain the potential difference

$$U = 4\pi ze/R, \quad (1)$$

where  $R$  is the distance between positive ions.

Assuming that  $R$  equals  $(1-2) \times 10^{-10}$  m,  $z = 2$ , and  $e = 1.6 \times 10^{19}$  KJ, we obtain that the potential difference amounts to 360–720 V. While activating the liquid media using the energy of the US field, an electrokinetic effect appears, which means that, owing to the action of the US wave, the double electric layer shifts and a potential difference is generated at the interface. The role of the energy of the US field reduces to the capacitor discharge at the interface, and, owing to this fact, the surface tension lowers and the wetting improves. The energy in the flat capacitor amounts to

$$W = \epsilon_0 \epsilon U^2 S / 2d, \quad (2)$$

where  $\epsilon_0$  is the dielectric constant ( $8.85 \times 10^{-12}$  C/(V m)),  $\epsilon$  is the relative dielectric permittivity,  $U$  is the potential difference,  $S$  is the area of the wetted surface, and  $d$  is the oxide layer thickness.

Then, the surface tension of the electrostatic forces, which is defined as the ratio of the energy to the area for  $\epsilon \leq 6-7$ , approximately amounts to  $(1.5-3.0) \times 10^{-3}$  N/m, and this is significantly less than the solder surface tension (0.5 N/m). For effective wetting, a greater potential difference is necessary; however, this cannot be obtained, because the US field damages the thin oxide layer.

There are other hypothesis that theoretically and experimentally prove that, in a US field, the tangential component  $\sigma_T$  of the vibration motion, which is proportional to the ultrasound power, is comparable with the

surface tension value  $\sigma_0$  in a nondisturbed medium. In this case, the surface tension can be presented in the form  $\sigma = \sigma_0 - \sigma_T$ . Therefore, the physical properties of the phase interface change in such a way that the energy of the surface tension diminishes, the limiting wetting angle decreases, and the solder spreading improves [2]. Therefore, metals with a lower  $\sigma_0$  value should possess a better wettability under ultrasonic action at the same introduced power.

The solder spreading over the surface of a soldered material depends on the relation of the adhesion forces of the solder relative to the material surface and the cohesion forces that define the bond strength between the solder particles. The greater the difference between the work of the adhesion forces with the soldered material and the work of the cohesion forces of the solder particles, which is defined by the formula

$$A_{\text{adg}} - A_{\text{cog}} = \sigma_{1,2}(\cos \Theta - 1), \quad (3)$$

the better the solder spreading over the soldered surface is. The solder spreading stops when the equilibrium is reached between the surface tension values of the interacting media:  $\sigma_{1,3} = \sigma_{1,2}\cos \Theta + \sigma_{2,3}$ , where  $\sigma_{1,2}$ ,  $\sigma_{1,3}$  and  $\sigma_{2,3}$  are the surface tension values in the interfaces solder–gas, gas–solid, and solder–solid, respectively, and  $\Theta$  is the wetting angle. Thus, for the solder spreading, the following condition should be fulfilled:  $\sigma_{1,3} > \sigma_{1,2}\cos \Theta + \sigma_{2,3}$ . This can be reached by decreasing the surface tension values  $\sigma_{1,3}$  and  $\sigma_{2,3}$ .

For the melted solder in its usual state on the surface of the soldered material, the work of the cohesion forces significantly exceeds the work of the adhesion forces. The melted solder, owing to the action of the forces of surface tension and gravitation, acquires the shape of a sessile drop, and the surface wettability is absent. In the solder–soldered material system, application of a solder flux allows improving the wettability of the metal surface by removing its oxide films. However, for difficult-to-solder metals, such as aluminum and titanium alloys, it is not effective to use fluxes because of the durable oxide film formed on the surface.

Introduction of US vibrations in the melt intensifies the wetting process of the nonmetal material. The changes in the values of the coefficients of the surface tension, which occur in this case, to a lesser degree effect the  $\sigma_{1,3}$  and  $\sigma_{1,2}$  values, since the solid body and the gas phase are the least susceptible to the perturbations at the given introduced ultrasound power. Evidently, the greatest changes occur on the melted solder–soldered material interface, and this effects the value of the coefficient  $\sigma_{2,3}$ .

The analysis of the experimental data presented in Fig. 1 shows that, for the aluminum alloy, the wetting force of the surface by the melt referred to the unit

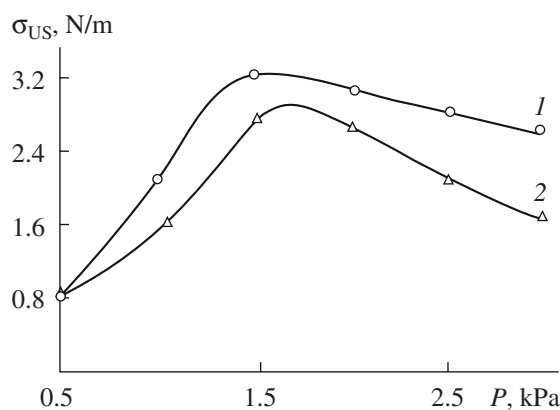


Fig. 1. Dependences of the surface tension at the melt–material interface vs. the cavitation pressure in the melt: (1) Sn–Pb–Zn–In, (2) Sn–Zn.

length of the wetted perimeter for Sn–Zn and Sn–Pb–Zn–In solders increases approximately by a factor of 5 at the cavitation pressure value in the solder of 1.5–2.0 kPa. This more than 6 times exceeds the surface tension value for these solders at similar temperatures (0.5 N/m). The energy of the interaction of the solders with glass ceramics at the wetting angle of  $25^\circ$  calculated using the Young–Dupre equation  $W = \sigma_{1,2}(1 + \cos \Theta)$  amounts to 0.95 N/m. This by approximately three orders of magnitude exceeds the energy of the dispersion interaction for the case of wetting by liquids with a low surface tension.

The dependence of the wettability degree on the process temperature confirms the presence of chemical interaction at the wetting of materials by solders in the US field. The investigation of the wetting process of AMG-6 alloy by low-melting solders with the melting point lower than  $100^\circ\text{C}$  performed on the basis of the Wood alloy with the addition of the metals Li, Zn, Ga, Ge, In, Pb, Bi, Cd demonstrated that the temperature threshold of the wetting was in the region of  $240\text{--}280^\circ\text{C}$ . The threshold lowers to the solder melting temperature when the ultrasonic power increases [1].

The mass transfer in the liquid at the US activation occurs owing to both convective motions in the form of macro- and microflows and diffusion [3]. The action of the US field energy on the melt increases the diffusion coefficient and activates the nucleation process

$$D' = D_0 e^{\frac{E - \Delta E}{RT}}, \quad (4)$$

where  $D_0$  is the preexponential factor,  $E$  is the energy of the diffusion activation,  $\Delta E$  is the change in the energy of the diffusion activation in the US field, and  $R$  is the gas constant.

The mass transfer is defined by the equation of convective diffusion, which, for the homogeneous case, has the form

$$\frac{\partial C}{\partial t} = -U \frac{\partial C}{\partial x} + \frac{\partial}{\partial x} \left( D \frac{\partial C}{\partial x} \right). \quad (5)$$

Usually the concentration dependence of the diffusion coefficient in a liquid solution can be neglected; then, the equation can be written as

$$\frac{\partial C}{\partial t} = -U \frac{\partial C}{\partial x} + D \frac{\partial^2 C}{\partial x^2}, \quad (6)$$

where  $U$  is the component of the velocity of the convective motion along the  $x$  axis.

In the US field, the force  $F$  acts on the diffusing particles, and, under its action, the substance particles move with the average velocity

$$U = \nu F, \quad (7)$$

where  $\nu$  is the particle mobility.

At the activation in the US field, a flux of particles, which move under the action of the force of US vibrations  $F$ , is added to the diffusion flux; then, the entire flux amounts to

$$J = -D \frac{\partial C}{\partial x} + UC_1 \cos \beta, \quad (8)$$

where  $C_1$  is the concentration of mobile particles, and  $\beta$  is the angle between the vector of the force of the US field and the diffusion flux vector.

The force of the US field that acts on the particle flux depends on the frequency  $\omega$  and the amplitude of the vibrations  $A$ :

$$F = \rho c \omega A S. \quad (9)$$

Substituting Eqs. (7) and (9) into Eq. (8), we obtain

$$J = -D \frac{\partial C}{\partial x} + \nu \rho c \omega A S C_1 \cos \beta. \quad (10)$$

The action of the electric field in the form of electric pulses passing through the melt with an amplitude that exceeds by 3–5 times the amplitude of the electric current corresponding to the start of the electric transport of ions stimulates the diffusion of the reactive components in the activation zone [4]. The simultaneous action of macrofluxes in the solder and powerful current pulses facilitates the electric transport generation and enhances the directed diffusion of the components in the soldered connection. The sum of the flux of ions

of the reactive components caused by the electric transfer has the form [5]

$$J_{ET} = B_i \rho \frac{I_a}{\tau} C_i \cos \alpha, \quad (11)$$

where  $I_a$  is the amplitude of the current pulses,  $\rho$  is the resistivity of the component,  $B_i$  is the ion mobility,  $\tau$  is the current pulse ratio,  $C_i$  is the concentration of ions of the reactive component in the melt, and  $\alpha$  is the angle between the vector of the electric field and the vector of the diffusion flux.

The sum flux of particles at the simultaneous activation by the energy of the US and the electric fields amounts to

$$J = -D \frac{\partial C}{\partial x} + B_i \rho \frac{I_a}{\tau} C_i \cos \alpha + \nu \rho c \omega A S C_1 \cos \beta. \quad (12)$$

Taking into account the heat effect in the US and the electric fields, the sum flux of the particles amounts to

$$J = -D_0 e^{\frac{E - \Delta E}{RT}} C^{T_0} \left[ 1 - \operatorname{erf} \left( \frac{x - (h/2)}{2 \sqrt{D_0 e^{\frac{E - \Delta E}{RT}} t}} \right) \right] + B_i \rho \frac{I_a}{\tau} C_i \cos \alpha + \nu \rho c \omega A S C_1 \cos \beta. \quad (13)$$

It follows from Eq. (13) that activation by the US field energy leads to an increase in the diffusion coefficient, and activation by the electric field energy leads to an increase in the sum flux of ions of the reactive components in the interaction zone and, hence, increases the velocity and the depth of diffusion. The stimulation of the diffusion processes of the reactive components in the soldered connection should lead to an increase of the interface on the solder–soldered materials boundary and to formation of chemical compounds between the solder components and the soldered materials; this increases the mechanical durability of the connections and improves their quality and service reliability.

A computer program in C++ (version 2.01, Borland International) was developed to model the diffusion processes according to Eq. (13). The initial data were as follows: the diffusion parameters (the diffusion coefficient, initial concentration, interface diffusion depth, and diffusion time), the parameters of the US activation (the amplitude of the vibrations, the mobility of the substance particles under the action of the US field, the frequency of the vibrations, the sound velocity in the material, and the contact area), and the electric field parameters (the mobility of the ions, the resistivity of



the reactive component, the concentration of ions, and the amplitude and frequency of the current pulses).

The process of interdiffusion of the components of the solder and the soldered material was modeled during the formation of the connection using POTs 10 solder and aluminum AMts alloy at the following boundary conditions: the contact area of 10–50 mm<sup>2</sup>; the amplitude of the US vibrations of 10–20  $\mu$ m; the sound velocity and the density of the aluminum alloy of 6200 m/s and  $2.7 \times 10^3$  kg/m<sup>3</sup>, respectively; the amplitude of the current pulses of 1–10 A; the frequency of the pulses of 1–10 Hz; the boundary diffusion depth of 0–20  $\mu$ m; the time of diffusion of 5–15 s; the resistivity of the alloy  $0.028 \times 10^{-6}$   $\Omega$ /m; and the frequency of the US vibrations of 22 and 44 kHz.

The results of the modeling showed that the US activation increased the concentration of the diffusing elements of Zn and Al in the interface depth by 15–20% on average, and the combined activation by the US and electric fields increased it by 30–45% (Fig. 2). With the increase in the amplitude and the frequency of the US vibrations, the concentration growth was observed, since the energy quantity adsorbed by the melt increased. The combined activation of the melt–soldered material system by the energy of the US vibrations and the powerful current pulses additionally increased the heat energy [6]. This allows reaching the soldering temperature at a greater rate, increasing the wettability of the surface by the solder, and increasing the process yield.

The structure of the soldered connections and the local elementary composition (using X-ray spectral analysis) were studied using a Stereoscan-360 electron microscope (Cambridge Instruments, Great Britain) with an AN-10000 energy spectrometer (Link, Great Britain) at an acceleration voltage of 30 kV and magnification of 10000 $\times$  in the regime of reflected and secondary electrons with photoregistration of the results and obtaining of a pseudocolor image. The X-ray spectral analysis of the elementary composition performed locally at points with a diameter of 1  $\mu$ m with sensitivity of 0.5% showed an increase in the intensity of the Al peaks at the current activation of the diffusion process (Fig. 3).

The width of the diffusion zone measured using the scanning electron microscope, in this case, amounted to 4–5  $\mu$ m for the POTs 10 and POS 61 solders (Fig. 4). For the POTs 10 solder, the diffusion zone was slightly wider because of the electromobile zink presence in the melt, which migrated to the interface and then deeper in the aluminum alloy thus increasing the width of the diffusion zone. The width of the interface increased to 6–8  $\mu$ m owing to the enhancement of the diffusion interaction and aluminum electromigration into the solder

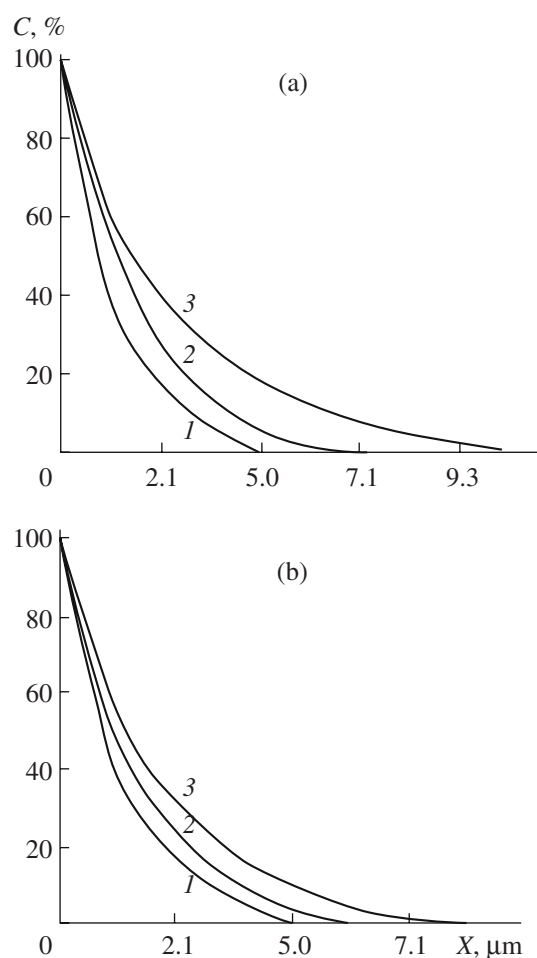


**Fig. 2.** Concentration diffusion profiles in US and electric fields. (1) heating; (2) US; (3) US + current 10 A. A,  $\mu$ m: (a) 20, (b) 10.

(Fig. 5a) if compared with it's size of 1.5  $\mu$ m at the US activation (Fig. 5b).

When the gas was passed in the reverse direction, the connection durability virtually did not increase, because tin and lead, which formed the solder, do not possess such mobility as aluminum. In this case, the width of the diffusion zone amounted to about 2  $\mu$ m.

The electrodiffusion mechanism assumes the action of an “electron wind” force on a thermally excited ion, which increases with the increase in the current density; the aluminum ions move to the positive pole increasing the depth of the diffusion layer, and the vacancies move to the negative pole.

The current activation leads to a decrease in the interface resistance for low-resistive metals prone to electromigration, such as aluminum, for example. The interface resistance of the soldered connections lowers by 60–70% and then begins to weakly increase. The lowering of the interface resistance can be elucidated

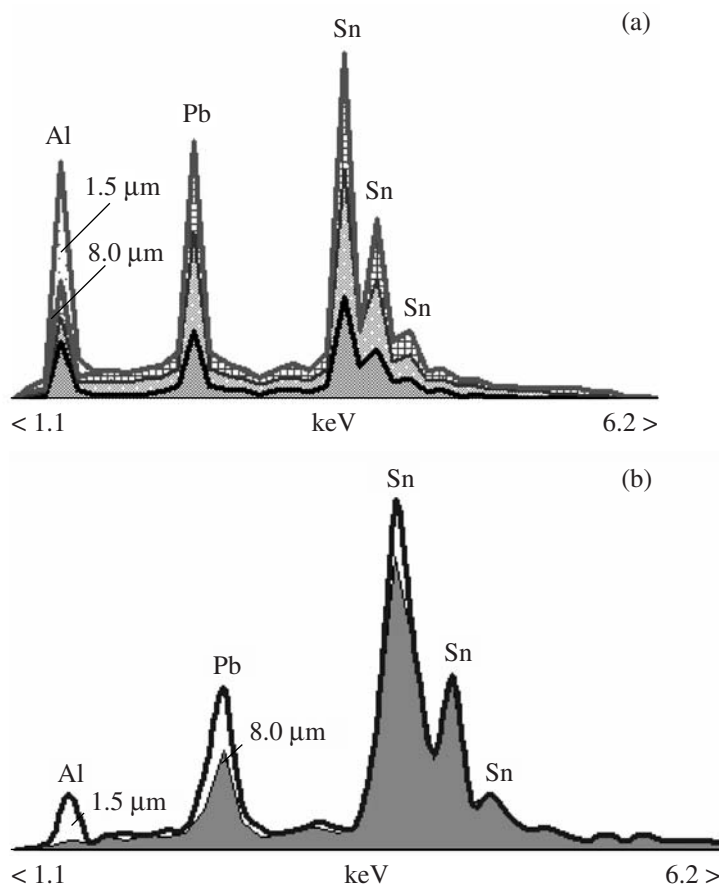


**Fig. 3.** Results of the local X-ray analysis of soldered connections: (a) activation in the US and electric fields; (b) US activation.

by the diffusion processes between the solder components and the part and by the improving of the wetting

process. The subsequent growth of the interface resistance occurs owing to the intensive oxidation of the solder components and the main material, as well as to formation of intermetallic compounds [7].

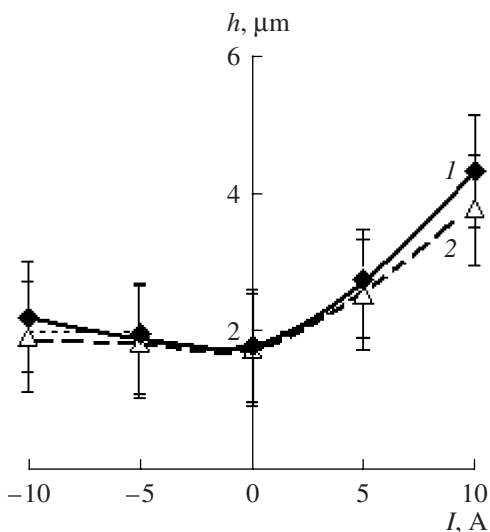


**Fig. 4.** Dependence of the interface width vs. the direction and magnitude of the current pulses: (1) POTs 10, (2) POS 61.

The results of modeling of the combined action of the energy of the US and electromagnetic fields were tested in practice during the formation of connections of AMTs alloy using the POS 61 and POTs 10 solders. The investigation of the durability of the connections vs. the duration of the US field action at different directions of the US vibrations (Fig. 6) showed that it reached 10 MPa in the case of longitudinal vibrations and 20 MPa in the case of parallel vibrations for 15–20 s [8]. The lesser time period was not enough for the development of destruction processes in the oxide layers and for wetting of the connector surface. For greater time periods, the durability lowers owing to the erosion of the soldered material and the solder oxidation. Passing the current pulses through the zone of formation of the connections in the direction from the solder to the soldered material increases the durability of the connections by a factor of 1.25–1.5 owing to the

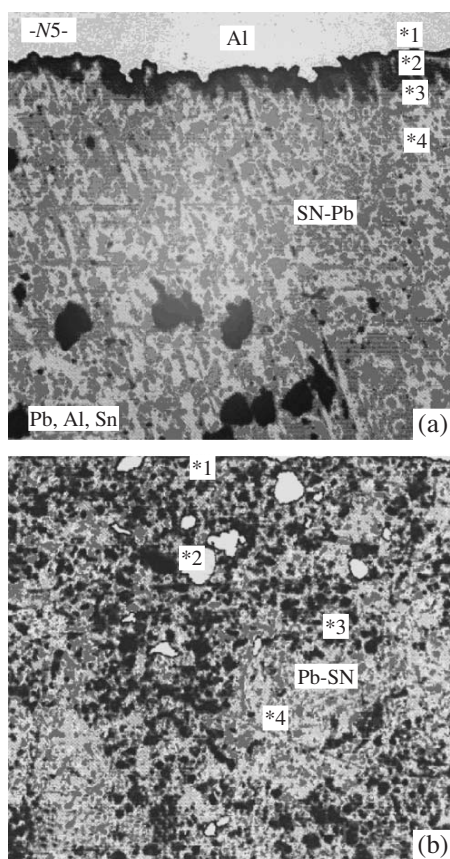


**Fig. 5.** Microstructure of soldered connections Al-(Sn-Pb): (a) in an ultrasonic field, (b) in ultrasonic and electric fields.

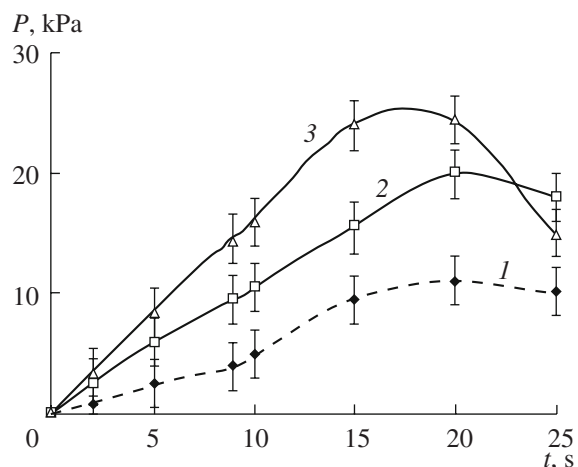


**Fig. 6.** Dependence of the durability of the connections vs. the time of action and the type of vibrations: (1) longitudinal, (2) parallel, (3) electric field action.

increase in the width of the diffusion zone and aluminum electromigration into the solder.

The modeling of the diffusion processes and their verification allowed defining the ways to increase the

rate and the depth of the diffusion of the reactive components at the combined activation using the energy of the US and electric field and to improve, in this way, the mechanical and electrophysical properties of the connections. The combined activation increases the concentration of the diffusing elements in the interface depth by 30–45% on average and increases the frequency of the US vibrations by 5–7%. In this way, the combined US and current activation of the processes of formation of the connections with difficult-to-solder metals increases the diffusion of the components in the interaction zone, which facilitates an increase in the durability of the soldered connections.

## REFERENCES

1. Kundas, S.P., Lanin, V.L., Tyavlovskii, M.D., and Dostanko, A.P., *Ul'trazvukovyye protsessy v proizvodstve izdelii elektronnoi tekhniki* (Ultrasonic processes for fabrication products of electronics), Dostanko, A.P., Ed., vol. 1, Minsk, 2002, pp. 267–285.
2. Rumak, N.V., Bondarik, V.M., and Lanin, V.L., Electrical Effects in Liquids and Melts under the Action of Ultrasonic Vibrations, *Dokl. AN Belarusi*, 1994, vol. 38, no. 2, pp. 115–118.
3. Lanin, V.L., Electrical Phenomena's in Liquids and Melts by Ultrasound processing, *3rd. Kinds Conf. on Applications of Power Ultrasound in Physical and Chemical Processing*, Paris, 2001, pp. 143–146.
4. Bondarik, V.M. and Lanin, V.L., Strength Properties of Connections Prepared Using Ultrasonic Soldering, *Tekhnol. Konstruir. Elektron. Appar.*, 1998, no. 3–4, pp. 33–37.
5. Bondarik V.M. and Lanin V.L., Physical Model of Combined Ultrasonic Soldering, *Ul'trazvukovaya tekhnika i tekhnologiya. Materialy II Mezhd. nauch.-tekhn. konf.* (Ultrasonic Engineering and Methods: Proc. II Int. Sci. and Techn. Conf.), Minsk: BATU, 1999, pp. 115–119.
6. Lanin V.L., Efficiency of Heating by Concentrated Energy Fluxes at Soldering in Electronics, *Elektron. Obrab. Mater.*, 2002, no. 2, pp. 17–20.
7. Lanin V.L. and Bondarik V.M., Electrical Resistance of Soldering Joints at Effect of Ultrasonic Oscillations, *Proc. 20th Int. Conf. on Electrical Contacts*, Stockholm, 2000, pp. 205–208.
8. Lanin V.L., Modeling of Diffusion Processes at Combined Action of Ultrasonic and Electromagnetic Fields, *Dokl. NAN Belarusi*, 2005, vol. 59, no. 1, pp. 49–52.

## OPERATING EXPERIENCE

# Seismically Safe Distances for Bottom Ground Loosening by High-Voltage Electrochemical Explosion

A. R. Rizun, Yu. V. Goleni, and T. D. Denisyuk

*Institute of Pulse Processes and Technologies, National Academy of Sciences of Ukraine,  
pr. Oktyabr'skii 43-a, Nikolaev, 54018 Ukraine*

*e-mail: iipt@iipr.com.ua*

Received December 14, 2007

**Abstract**—Distances are found to be seismically safe for buildings at loosening of the ground soils by a high-voltage electrochemical explosion during conducting of reconstruction of operating marine and river ports.

**DOI:** 10.3103/S1068375508030125

## INTRODUCTION

High-voltage electrochemical explosion (HVECE) is a complex of physicochemical phenomena proceeding in the presence of the discharge channel zone of substances or compounds capable of exothermal chemical transformations in conditions of high temperatures and voltages developing in the channel. The energy released due to these transformations is summarized with the electric energy supplied from the capacitive storage of the surge-current generator (SCG); as a result, the total quantity of the energy significantly grows save for increasing of the mass and overall dimensions of the equipment.

Specially developed water-filled exothermal composites (WEC) are applied as substances capable of significantly increasing the electric discharge power; in the composites, aluminum in powder form (PAP-1, PAP-2) reaches 40% total volume. The powder particles are coated with stearic acid in order to significantly decrease the sensitivity to mechanical effects and the ability to detonate. The oxidizing constituent in WEC is a gelled solution of ammonium nitrate [1]. For blasting of bottom grounds, small portions of WEC are applied: from 0.01 to 0.05 kg.

In the course of the reconstruction of operating sea or river ports with application of HVECE for loosening of bottom ground, safe distances must be determined.

Seismically safe distances for buildings and constructions for blasting powder explosions are calculated by the formula

$$R_b = K_b a^3 \sqrt{Q}, \quad (1)$$

where  $R_b$  is the distance from the explosion place to the point of safe vibration of the ground, m;  $K_b$  is the coefficient depending on the ground properties (it has the values given in Table 2);  $a$  is the coefficient depending on

the blasting factor  $n$  (it has the values given in Table 1); and  $Q$  is the charge weight, kg.

Seismically safe distances for instantaneous explosions are calculated by formula (1). For delayed explosions, to which HVECE is attributed, these distances are specified by the experiment, since a complex dependence between the blasting factor, the ground categories, and the seismic safety distance exists. Thus, for example, on the one hand, for instantaneous explosions characterized by moderate release, the factor  $n$  is greater than 1 and the coefficient  $a$  is less than 1. For delayed explosions, on the contrary,  $n < 1$ ,  $a > 1$ ; that is, in similar grounds at identical equivalents of blasting powder (BP), the seismic safety distance must be greater. On the other hand, at greater time of the explosion, the dissipation of the acoustic component of its energy is greater, and the safe distance radius decreases [2].

Experimental measurement of the radius  $R_b$  was carried out in the water area of Kamyshinskaya bay of the Sevastopol sea port. For execution of the work, an engineering design was made. It contained a plan and cross sectional view of the dredging site with specification of the blasting arrangement network (Fig. 1), the required depth of loosening, the volume of the final removal, and the place of its dumping.

Blast-hole drilling in the bottom ground was carried out at a depth of 0.6 m according to the network (Fig. 1).

**Table 1.** Dependence of the coefficient  $a$  on the blasting factor

$n$	$\leq 0.5$	1	2	$\geq 3$
$a$	1.2	1	0.8	0.7



The twofold calculated radius  $2R_b$  of the safe distance for instantaneous explosions was taken as the initial point of the blasting arrangement from the construction site

$$R_b = K_b a^3 \sqrt{W + Q}, \quad (2)$$

where  $W$  is the SCG stored energy,  $W = 70$  kJ is equivalent to 0.01 kg WEC,  $Q = 0.03$  kg WEC is equivalent to 210 kJ,  $K_b = 20.0$  for water-saturated grounds,  $a = 1.2$  (at  $n < 1$ ), and

$$2R_b = 8.4 \times 2 = 16.8 \text{ m.}$$

For the determination of the impact force of the waves generated by HVECE on objects and waterborne vehicles, barium titanate based piezoelectric transducers converting pressure into electric signals were applied. The transducers with a diameter of 18 mm were placed in blast holes with a diameter of 36 mm on construction footings in the aqueous medium. The signal from the transducers was supplied through an armored cable to the input of a strain-gage amplifier (TU-4M). The recording gage was a bifilar oscillograph (H-105). The measurements were carried out at the distances presented in Table 3.

Figure 2 shows the dependence of the maximum pressure at the front of the waves generated by HVECE on the distance from the point of the installation of the transducers for water-saturated grounds. The level at the mark of four standard units of pressure is considered to be the maximum allowable for seismic loads on buildings.

Thus, seismically safe distances to buildings and constructions for HVECE with a stored energy of 70 kJ and EL weight of 0.03 kg have been experimentally specified. It follows from the obtained dependence that the error of the calculated data (8.4 m) and of the experimental ones (4.0 m) for bottom grounds in an aqueous medium was more than 50%.

The obtained experimental values of the safe distance for work with HVECE are significantly less than

**Table 2.** Dependence of the coefficient  $K_b$  on the ground categories

Grounds	Category	Coefficient $K_b$
Porphyrite, quartz	XV	3
Compact rock	XIII	3
Compact limestone	X	5
Dolomite, limestone	XII	7
Sand	V	8
Clay	IV	9
Soil	III	15
Water-saturated	from III to XV	20

**Table 3.** Results of measurements of the radii of safe distances for HVECE

$P$ , s. u.	$R_b$ , m
0.8	16.8
1.5	12.0
2.0	8.4
2.5	6.0
3.0	4.0

the calculated values; this allows stating that the time of the delayed explosions influences the safe distance radius stronger than the blasting factor.

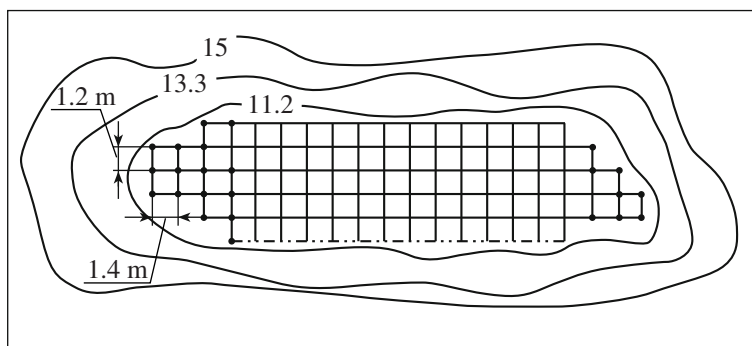


**Fig. 1.** Site plan and network of blast-hole drilling.



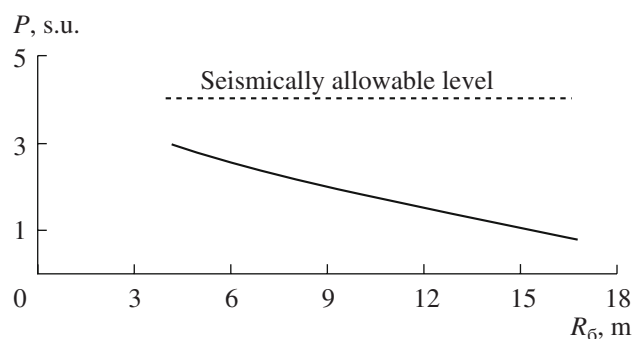


**Fig. 2.** Dependence of the maximum pressure of the compression waves on the distance to the measurement point.

For HVECE, the coefficient  $a$  depending on the blasting factor may be reduced twofold. Then, the calculation of the safe distances for HCECE may be approximated into the following equation:

$$R_b = K_b \frac{a}{2} \sqrt[3]{W + Q}. \quad (3)$$

The results of the experimental studies have been verified in the course of the bottom dredging in the water area of Sevastopol seaport. Technology and special equipment have been developed on the basis of these results. The introduction of the technology will allow solving the problem of safe realization of bottom dredging or destruction of foreshore massifs near buildings and communication assembles.

## REFERENCES

1. Vovchenko, A.I. and Posokhov, A.A., *Upravlyaemye elektrovzryvnye protsessy preobrazovaniya energii v kondensirovannykh sredakh* (Controlled Electric-Explosion Processes of Energy Conversion in Condensed Media), Kiev: Naukova Dumka, 1992.
2. Kushnarev, D.M. and Belikov, M.P., *Vzryvnye raboty v gidromeliorativnom i sel'skom stroitel'stve* (Explosive Works in Irrigation-and-Drainage and Agricultural Construction), Moscow: Izdatel'stvo Literatury po Stroitel'stvu, 1972.

---

---

## OPERATING EXPERIENCE

---

---

# Electric-Discharge Intensification of the Wool Scouring Process

A. A. Zubenko

*Institute of Pulse Processes and Technologies, National Academy of Sciences of Ukraine,  
pr. Oktyabr'skii 43-a, Nikolaev, 54018 Ukraine*

*e-mail: iipt@iipt.com.ua*

Received December 5, 2007

**Abstract**—The results of experiments on wool washing by high-voltage electric discharge in a liquid are presented. The efficiency of this method of washing is shown. The process of washing is considerably accelerated at the reduction of the expense for chemical reagents and a more than 3-fold diminishment of the energy expense is noted.

**DOI:** 10.3103/S1068375508030137

## INTRODUCTION

Despite the high price of virgin wool on the world market, inexpensive wool made both in Ukraine and other countries of the CIS is not in demand by consumers.

The main cause of this is the poor quality of its primary treatment. The determining operation of primary treatment of wool is its scouring. In this process, the wool fiber is freed of contaminating impurities and wool grease. At the same time, wool grease is of great practical importance for the maintenance of wool quality; its amount after scouring must be from 0.5 to 1.0% for homogeneous wool and up to 2.0% for mixed wool [1].

The process of wool scouring by the traditional method consists of the following: a scouring solution, penetrating between the surface of the wool and the contaminating impurities, moistens them; decreases the contamination adhesion to the fibers; and causes the separation of the former from the surface of the latter. The scouring lasts for several hours; it requires heating of the scouring solutions up to temperatures from 45 to 50°C and consumption of 25 to 40 liters of water, 100 to 160 grams of alkali, and 30 grams of liquid soap per 1 kg of starting material. In addition, the chemicals in the scouring solutions render a harmful effect on the wool fibers leading to a decrease of their breaking force.

The listed disadvantages of the traditional method of wool scouring motivated us to search for new, more efficient methods.

The present paper describes the results of studies of the efficiency of wool scouring with application of an electric discharge in liquid.

Electric discharge is the best high-power generator of nonlinear volume cavitation in aqueous solutions. Electric-discharge cavitation renders a destructive (mechanical, acoustic, and photolytic) influence on contaminations. In addition, due to the influence of the

cavitation factors, in the solution, there appear active radicals and radical groups—activators of chemical reactions [2]. That is, the active removal of contaminants takes place at significantly less concentrations of scouring agents and at lower temperatures (from 20 to 25°C). We have succeeded in selecting a mode of wool treatment in which the wool fibers remain undamaged and the contaminants are practically completely removed. It is also characteristic of the electric-discharge treatment of wool that the amount of wool grease remaining on the fiber is within 2%, this being satisfactory for subsequent treatment of the raw material. The basic advantage of the electric-discharge wool treatment is the reduction of the scouring time by several orders and of the reagent consumption by several times, as well as the reduction of the energy consumption for heating of the scouring solution.

## EXPERIMENTAL

The studies were carried out by virtue of a high-voltage installation that consisted of a surge-current generator containing a charging unit, three capacitive storage devices (IK100-0.25 condensers), an air sparking ball, and an ignition unit; a circuit for the measurement of the electric characteristics consisting of a coaxial shunt (2.5 mOhm resistance) and an oscillograph (C8-13); and an electric discharge chamber.

The electric discharge chamber is a right-angled reservoir of the dimensions 500 × 200 × 300 mm made of stainless steel of the thickness  $\delta = 5$  mm. Three pairs of electrodes spaced by 175 mm were mounted into the long walls of the chamber at a distance of 50 mm from its bottom, a dielectric grid with a mesh width of 10 × 10 mm was situated at a distance of 50 mm above the electrodes, and a wool layer of thickness from 30 to 40 mm was placed on the grid (the dry weight of the load was 1 kg).

**Table 1.** Scouring modes

Treatment step	Reagent content in the solution, g/l		$T, ^\circ\text{C}$	Electric parameters					Amount of heat for the solution heating, kJ
	Sodium carbonate	Soap		$f, \text{Hz}$	$C, \mu\text{F}$	$U, \text{kV}$	$n, \text{pulse}$	$E_{\text{obr}}, \text{kJ}$	
1	Pure water		15	2	0.25	25	500	36	500
2	1.5	0.4	25	2	0.5	25	500	72	
3	Pure water		15	2	0.25	25	300	18	
4	1.0	0.3	25	2	0.5	25	300	18	500
5	Pure water		15	2	0.25	25	300	18	

**Table 2.** Decontamination results

Wool state	Amount of wool grease, %	
	Homogeneous wool	Mixed wool
Initial	12.5	6.71
After the third step	1.77	0.97
After the fifth step	0.94	0.65

The chamber was filled with scouring solution up to 50 mm above the grid (the solution volume was 12 l).

The wool scouring was carried out in five steps; the modes of the treatment are given in Table 1.

After the treatment, the wool was taken out of the discharge chamber and dried.

## RESULTS AND CONCLUSIONS

The dried wool was of white color and it had standard strength properties. One can see from the results presented in Table 2 that, for decontamination of 1 kg of homogeneous wool with application of high-voltage electric discharges for its scouring, in order to satisfy the requirements of the GOST, five steps of treatment are necessary. The energy consumption is 1162 kJ, 1000 kJ of them being the energy consumption for heating of the scouring solutions. Three steps of treatment

and 626 kJ of energy are sufficient for decontamination of 1 kg of mixed wool.

In the process of wool treatment by the traditional method, the energy consumption only for heating of the scouring solutions exceeds 3000 kJ.

The experiment results have shown the efficiency of wool scouring with application of an electric discharge in liquid. In this case, the scouring process is faster by several orders, the reagent consumption is reduced by a factor of 2–3, and the energy consumption is decreased by more than a factor of three.

## NOMENCLATURE

$T$  is the liquid temperature in the discharge chamber,  $^\circ\text{C}$ ;  $f$  is the frequency of repetition of high-voltage electric discharges, Hz;  $C$  is the storage capacity,  $\mu\text{F}$ ;  $U$  is the initial voltage of the capacitive storage, kV;  $n$  is the number of pulses in a step of wool treatment;  $E_{\text{obr}}$  is the total electric energy of the electric-discharge treatment in a step, kJ; and  $E_n$  is the amount of heat for the solution heating, kJ.

## REFERENCES

1. Sheifer, O.Ya., *Proizvodstvo i otsenka kachestva shersti* (Wool Production and Estimation of its Quality), Moscow, 1988.
2. Malyushevskii, P.P. and Yushchishina, A.N., Electric Explosion in Chemicotechnological Processes. Part 1., *Elektron. Obrab. Mater.*, 2001, no. 4, pp. 58–72.

---

---

OPERATING EXPERIENCE

---

---

## Solid-State Welding of Tubular Joints of Titanium and Copper with Application of Electrohydropulse Loading

L. Yu. Demidenko and N. A. Onatskaya

*Institute of Pulse Processes and Technologies, National Academy of Sciences of Ukraine,  
pr. Oktyabr'skii 43-a, Nikolaev, 54018 Ukraine*

*e-mail: iipt@iipr.com.ua*

Received December 14, 2007

**Abstract**—The possibility of welding in the hard state of tubular connections from titanium and copper with application of electrohydraulic pulse beading and postheating in the narrow temperature–temporal range of the parameters of the process was showed experimentally. The index of the compactness of the obtained joint weld takes on values of  $79.3 \pm 12.4\%$  here, and the fastness on the cut is at the level of the copper fastness. Formation of metallic connections on the larger part of the contact surface supports the receipt of reliable electric contact on all the surfaces of the joint.

DOI: 10.3103/S1068375508030149

### INTRODUCTION

Welding is one of the leading technological processes of modern industry. The level of its development and improvement influences in many instances the state of the art in mechanical engineering, construction engineering, and some other branches. Enlargement of the list of materials used for obtaining of welded assemblies determines the application of various welding techniques, including fusion welding and pressure welding (without fusion).

The majority of combinations of dissimilar metals and alloys are characterized by significant differences in their physicochemical properties; this impedes obtaining welded joints by fusion of jointed metals. Therefore, obtaining of qualitative welded joints of dissimilar metals is one of the urgent problems in modern welding engineering. For realization of these joints, diffusion welding is most widely applied. For prevention of brittle phase formation in the joint zone, intermediate layers are usually used [1].

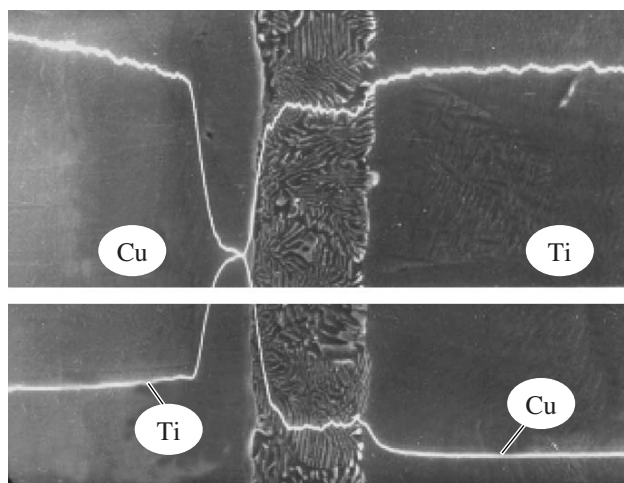
In view of the above, the development of new techniques of pressure welding for direct joining of dissimilar metals, for example, titanium and copper, which are characterized by low mutual solubility, is a problem of high priority.

The aim of the present work is to study the possibility of obtaining tubular joints of “titanium–copper” on the major part of the contact surface area by electrohydropulse loading of solid-state welding. These joints may be applied, for example, in cathodes of electrolyzers for copper production [2]. The following requirements are specified for them: the burst strength being

on the order of the parent metal (copper), stable low-transition electric resistance, and the ability of long-term operation at high temperatures and impact mechanical loads.

The experiments were carried out for full-scale tubular shells of the titanium alloy BT1 and copper M1 with an inside diameter of 24 mm with the copper shell wall thickness of 2 mm supplied by AO “Uralelektromed” (Verkhnyaya Pyshma, Sverdlovsk Region).

For removal of fatty films, directly before welding, the sample contact surfaces were degreased with alcohol. Samples were welded with application of electrohydropulse press fitting [3] and subsequent heat treatment of the joints in a chamber furnace by heating up to the temperature  $T = 850^\circ\text{C}$  with a time lag action of  $t = 20$  min. This welding is a variant of pressure welding with heating; however, it differs from the known techniques by the fact that the welded pieces in the heated state are not affected by external pressure. Its role is played in part by the residual contact pressure being formed as a result of the copper tube press fitting into the titanium bush sleeve. The EH press fitting of the copper tube into the titanium bush sleeve eliminates the initial gap between the shells and contributes to common plastic deformation of the contacting surfaces due to their pulse compression; as a result, a physical contact of the surfaces is formed. Formation of the interference between the tubular shells across the width of the contact surface of 75 mm prevents air from penetrating between them at heating; that is, conditions are created that prevent oxidation of the welded surfaces, which are analogous to those taking place at automatic vacuum welding [4]. In the process of heating, due to the differ-



Structure of the welded joint (x1000) of the titanium alloy BT1 and the copper M1 and the character of the element distribution in the transition zone.

ence of the coefficients of the thermal expansion of the welded metals, a significant gain of the contact pressure is obtained. Accordingly, the process of development of the physical contact between the surfaces of the joined elements is facilitated, and intense activation of diffusion processes is provided; that is, a process similar to the diffusion welding process is realized.

Thus, the approaching of the welded surfaces is obtained both due to their pulse compression before heating at the active deformation stage and due to thermal activation of the processes of microplastic metal deformation in the contact zone proceeding under the action of residual micro- and macrostresses created in the course of the press fitting. The first process, due to its pulse character, renders the activating influence on the second one [5]. Oxide films are removed from the welded surfaces most often by dissolving in the parent metal at heating.

The quality of the obtained joints was estimated by the results of metallographic strength tests.

The criterion for the determination of the temperature–time range of the welding was the strength balance of the welded joint and the less strong metal (copper) in the course of shear tests at 20°C. Cylindrical templates with a height of 5 mm cut out of the middle part of the samples were applied for the tests. A quality criterion was also the density index  $Y$  characterizing, in percentage terms, the relative total length of the boundary in the cross section of the thickness less than 0.5  $\mu\text{m}$ . Measurements of the latter were carried out at 100 points equally spaced along the perimeter of the joint by virtue of a JCSA-733 X-ray microanalyzer at 1000-fold magnification with the application of a micron straight scale with a scale interval of 0.5  $\mu\text{m}$ . According to the obtained results, the density index at the selected temperature–time range of the welding is  $Y = 79.3 \pm 12.4\%$ ; lack of penetration was not observed throughout the

cross section in the joint zone. Formation of the welded joint over the developed surface contributes to obtaining of a reliable electric contact over the whole joint surface.

The distribution (diffusion) of the elements in the joint zone was studied by virtue of an electron probe in a line perpendicular to the contact surface. The figure shows the transition zone of the welded joint of the copper M-1 and the titanium alloy BT1 and the element distribution in it.

It was found that, in the welded “copper–titanium” joint, in the zone of their contacting, a transition zone with a complex layered structure with a maximum width up to 20  $\mu\text{m}$  is formed.

Studies of the transition zone of the copper–titanium joints by micro-X-ray-spectrum analysis have shown that the concentration of the elements in the contact zone varies smoothly. One can see from the figure that, in the near-contact zones, a smooth variation of the chemical composition from 100% Ti (or Cu) to 100% Cu (or Ti) is observed; in addition, on the part of copper, the element concentration gradient is shown more sharply than on the part of titanium. It should be noted that copper penetrates titanium at a greater depth ( $\sim 17 \mu\text{m}$ ) than titanium penetrates copper ( $\sim 12 \mu\text{m}$ ); this is in good agreement with the ratio of their atom diameters ( $1.28 \times 10^{-10}$  and  $1.46 \times 10^{-10}$  m, respectively).

The carried out identification of phase formations in the transition zone has shown that, on the part of the titanium alloy BT1, their composition corresponds to a stoichiometric ratio of the type  $\text{Ti}_3\text{Cu}_2$  and  $\text{Ti}_2\text{Cu}$ , and, in the near-contact zone, on the part of copper, compounds of the type  $\text{Cu}_2\text{Ti}$  and  $\text{CuTi}$  take place. The phase formations are the result of directed motion in the field of effective stresses of mass flow of one of the joined metals into the internal volumes of the other metal.

Mechanical shear tests have shown that the destruction of the joint occurs in the near-contact zone on the part of the copper; the shearing strength of the joints fluctuated in the narrow range of  $180 \pm 5$  MPa, this being on the order of the strength of the parent metal. This counts in favor of the fact that the forming transition zone of the welded titanium–copper joints is not a microconcentrator of destruction in the welded joint.

Thus, welded full-scale models of tubular titanium–copper joints equal in strength with copper may be obtained by their direct jointing with application of electrohydropulse press fitting in a narrow temperature–time range of the process parameters only. In this case, the selected temperature of the welding is slightly below the temperature of the liquid eutectics formation (875°C) [1].

The results of the studies may be indicative of the efficiency of the electrohydropulse loading application for obtaining of welded tubular joints of titanium–cop-



per by the type of diffusion for cathode current leads of electrolyzers, since the formation of the welded joint practically over the whole contact surface contributes to the appearance of a reliable electric contact with low transition electrical resistance remaining invariant in the process of operation.

#### REFERENCES

1. *Diffuzionnaya svarka materialov. Spravochnik* (Diffusion Welding of Materials. Handbook), Kazakov, N.F., Ed., Moscow, 1981.
2. Sabokar', V.K., Kireev, L.S., and Lyu, V., Welded Titanium-Copper Cathode, *Avtom. Svar.*, 1980, no. 5, p. 76.
3. Mazurovskii, B.Ya., *Elektrohidroimpul'snaya zapressovka trub v trubnykh reshetkakh teploobvennykh apparatov* (Electrohydropulse Press-Fitting of Tubes in Tube Sheets of Heat Exchangers), Kiev, 1980.
4. Finkel'shtein, M.L., *Diffuzionnaya svarka v zhidkikh sredakh* (Diffusion Welding in Liquid Media), Moscow, 1987.
5. Opara, V.S., Demidenko, L.Yu., and Onatskaya, N.A., Influence of Pulse Compression on the Process of Press-Thermal Electrohydropulse Welding of Tubes with Tube Sheets, *Avtom. Svar.*, 1995, no. 6, pp. 32-34.

## OPERATING EXPERIENCE

# Experimental Measurement of Residual Stresses in Microwires

S. A. Baranov<sup>a,b</sup> and S. S. Stoyanov<sup>b</sup>

<sup>a</sup> Institute of Applied Physics, Academy of Sciences of Moldova, ul. Academiei 5, Chisinau, MD-2028 Republic of Moldova  
e-mail: dikusar@phys.asm.md

<sup>b</sup> Shevchenko Pridnestrov'e State University, ul. 25 Oktyabrya 128, Tiraspol, Republic of Moldova

Received November 21, 2007; in final form, February 4, 2008

**Abstract**—Methods of measurement of residual stresses in cast amorphous microwires are submitted. The obtained experimental results confirm the earlier given theoretical conclusions.

**DOI:** 10.3103/S1068375508030150

## INTRODUCTION

There exist a number of methods for experimental measurement of residual stresses appearing in a microwire in the process of its obtaining. Below, we will give the result of residual stress measurement by the polarimetric method, which was earlier applied by researchers for other objects (see, for example, [1]). Earlier, we developed a method of direct measurement of the core deformation [2] (the so-called method of horizontal lines); we have compared the results of these measurements with results obtained by the methods of ferromagnetic resonance (FMR) and natural ferromagnetic resonance (NFMR) that, by the value of the shift or the broadening of the ferromagnetic resonance, allow calculation of the residual stresses (these results are given in [3–7]).

## POLARIMETRIC METHODS OF STRESS MEASUREMENT IN MICROWIRES

These methods are based on the laws of photoelasticity, precisely, on the fact that the double refraction appearing in the stressed glass coating of the microwire is proportional to the stresses  $\sigma_i$  effective in this object. For our purposes, the law of photoelasticity may be mathematically written in the form

$$\delta = c l \sigma, \quad (1)$$

where  $\delta$  is the optic linear rate of travel of mutually perpendicular beams propagating in the stressed object,  $c$  is the photoelastic constant having values of  $(2-3) \times 10^{-10} \text{ m}^2/\text{H}$ ,  $l$  is the glass thickness  $((1-20) \times 10^{-6} \text{ m})$ , and  $\sigma$  is the stresses in the glass.

The angular difference of the travel is determined as follows:

$$\varphi = 360^\circ \frac{\delta l}{\lambda}. \quad (2)$$

In actual practice, the compensator method is the simplest. The principle of the method is that polarized

light, having passed through the stressed sample, is “compensated” for by the glass plate, to which stresses are applied on the opposite side. A more precise method for stress measurement may be carried out according to the following improved optical schematic. In this method, elliptically polarized light is transformed into linearly polarized light by virtue of a plate with an additional difference of travel of  $\lambda/4$ .

In a standard PKS-56 polarimeter, for measurement with a compensator according to the above-proposed optical schematic, light with the wavelength  $\lambda = 340 \text{ nm}$  is applied (the optical schematic includes a green filter). It follows from the experiments that the stresses in the glass are compression stresses (in contrast to the stresses in the core, which are tensile stresses). The method allows obtaining longitudinal stresses averaged by the instrument resolution. (In the considered case, an amorphous wire with a thick core (with its diameter being determined to be  $10-15 \mu\text{m}$ ) was taken for the measurements). The experimentally found residual stresses can be compared with the theoretical results [3, 6] only qualitatively. The table below gives the dependences of the residual stresses in the microwire glass isolation on the parameter  $x$ , which is determined as the ratio of the cross sectional area of the glass coating to the cross sectional area of the core (this parameter is applied in the theory of residual stresses [3, 6]).

The negative sign in the tabular results shows that the residual stresses have the character of compression stresses. Let us note that, as can be seen from the table, the residual stresses decrease in absolute magnitude at

Dependences of the residual stresses in glass isolation (at variation of the parameter  $x$ ) measured by the polarimetric method

$x$	1.5	2	3 and greater
$\sigma$ , GPa	−0.4	−0.3	−0.2
error, %	40	20	30

the parameter  $x$  increase; this corresponds to the theoretical calculations presented in [3, 6].

### CONCLUSIONS

Residual stresses in glass isolation in a cast amorphous microwire have been experimentally studied. The residual stresses in the glass have been found to be of compression character, whereas the deformations in the core are of tensile character (see [2–7]).

Let us note that the earlier considered methods of residual stress measurement and the method proposed here are in agreement with the theoretical calculation (presented, for example, in [3, 6]) and, therefore, they confirm the microwire model adopted in [3, 6].

### REFERENCES

1. Reti, P., *Nerazrushayushchie metody kontrolya metallov* (Nondestructive Methods of Metal Control), Moscow: Mashinostroenie, 1972.
2. Baranov, S.A., Residual Deformation in Amorphous Microwire, *Elektron. Obrab. Mater.*, 2006, no. 6, pp. 69–71.
3. Baranov, S.A., Zotov, S.K., Larin, V.S., and Torkunov, A.V., Peculiarities of Natural Ferromagnetic Resonance in Amorphous Microwire, *Fiz. Met. Metalloved.*, 1991, vol. 69, issue 12, pp. 172–173.
4. Baranov, S.A., Berzhanskii, V.N., Zotov, S.K., et al., Ferromagnetic Resonance in Amorphous Magnetic Wires, *FMM*, 1989, vol. 67, issue 1, pp. 73–78.
5. Baranov, S.A., Estimation of Residual Stress Distribution in Amorphous Microwire Core, *Metalloved. Term. Obrab. Mater.*, 2001, no. 4, pp. 34–35.
6. Baranov, S.A., Residual Stresses in Amorphous Microwire Core, *Metalloved. Term. Obrab. Mater.*, 2003, no. 7, pp. 38–40.
7. Baranov, S.A. and Stoyanov, S.S., Study of Microwire by Ferromagnetic Resonance Method, *Elektron. Obrab. Mater.*, 2006, no. 3, pp. 191–195.

## OPERATING EXPERIENCE

# Nonmonotonous Capacitance–Voltage Characteristics in Metal–Glass–Semiconductor Structures

S. I. Vlasov, A. A. Nasirov, O. O. Mamatkarimov, M. A. Ergasheva

National University of Uzbekistan, Vuzgorodok, Tashkent, 100174 Republic of Uzbekistan

e-mail: vlasov@uzsci.net

Received January 14, 2008

**Abstract**—The nature of nonmonotonous behavior of high-frequency capacitance–voltage characteristics of metal–glass–semiconductor structures is investigated. It is shown that the nonmonotonous variation in capacitance of metal–glass–semiconductor structures at inverse voltages can be caused by the presence of structure defects of acceptor nature in the glass in the layer adjacent to the glass–semiconductor interface.

DOI: 10.3103/S1068375508030162

Researchers often observed a nonmonotonous behavior in high-frequency capacitance–voltage characteristics in the range of inversion voltages while investigating the electrophysical properties of metal–insulator–semiconductor (MIS) structures [1], which cannot be described in the framework of the capacitance of an ideal structure. This nonmonotonous behavior is most distinctly observed when we measure the capacitance of the structure at sufficiently low temperatures [2]. To explain the observed capacitance behavior, models were applied that took into account the following phenomena: the nonuniform distribution of surface states within the semiconductor forbidden gap owing to the surface potential fluctuations [3], the tunnel recharge of microcrystalline inclusions localized in the insulator at a short distance from the semiconductor–insulator interface [1], and the presence of a distribution profile of deep impurity centers in the semiconductor substrate [4]. We noted a similar nonmonotonous behavior of the capacitance–voltage characteristics in the metal–glass–semiconductor (MIS) structures prepared on the basis of crystalline silicon covered by a layer of a lead-borosilicate glass [5]. To find the nature of the observed capacitance behavior in structures made using lead-borosilicate glasses, we used silicon wafers (KEF-2.5, KEF-5, and KEF-10 with the crystallographic orientation  $\langle 111 \rangle$ ) and a lead-borosilicate glass of the type  $\text{PbO-SiO}_2\text{-B}_2\text{O}_3\text{-Al}_2\text{O}_3\text{-Ta}_2\text{O}_5$  with the mass percentage content of the components 49 : 32 : 15 : 3 : 1 in group 1 and 49 : 30 : 17 : 3 : 1 in group 2. The structures in both groups were made using a technology similar to that described in [6]. The methods of high-frequency capacitance–voltage characteristics [7] and of isothermal relaxation of capacitance in Schottky diodes [8] were used in the research.

The capacitance–voltage characteristics of one of the studied structures, which were measured in the dark at room temperature at a frequency of 150 kHz, are

shown in Fig. 1. The dependence demonstrates that, for voltages of 5–9 V, the measured structure capacitance reaches a plateau; however, with the subsequent increase in the voltage to 10–14 V, the measured capacitance lowers. None of the structures of group 2 exhibited the nonmonotonous capacitance–voltage characteristics. To determine the influence of impurity centers localized in the semiconductor substrate on the capacitance–voltage characteristics, the glass layer was removed from the MIS structure using a chemical method, and a Schottky barrier was formed by Au vacuum evaporation. Then, using the method of [7], we determined the concentration and the energy spectrum of the deep centers present in the semiconductor substrate. The analysis of the results showed that, in all the prepared Schottky barriers, the recharge occurred of the deep center with ionization energy of  $E_C = 0.4$  eV and a concentration of  $N_D = 1\text{--}3 \times 10^{12} \text{ cm}^{-3}$ . The tempera-

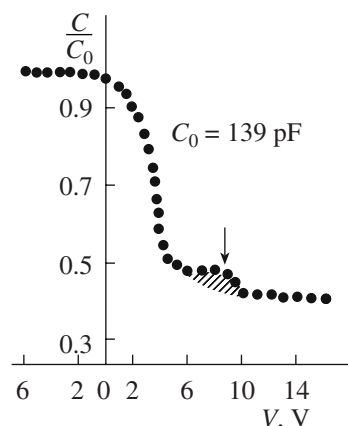


**Fig. 1.** Capacitance–voltage characteristic of the metal–glass–semiconductor structure of group 1 (normalized to the capacitance of the glass layer).

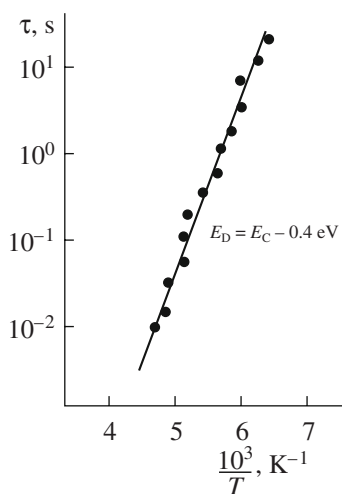


Fig. 2. Temperature dependence of the time constant of filling relaxation.

ture dependence of the time constant of the filling relaxation for the found center is shown in Fig. 2. The value of the charge created by the found center (at the condition of its uniform distribution within the entire space charge region of the semiconductor with the thickness  $d$ ) can be defined as  $Q = qN_D Sd = 3 \times 10^{-11}$  K (where  $S$  is the metal contact area of the Schottky diode). The charge value generated owing to the local nonuniformity in the capacitance-voltage characteristics of the MIS structure (defined using the shaded region in the C-V dependence, Fig. 1) amounts to  $Q_1 = 5 \times 10^{-8}$  K. The comparison of these two values shows that a deep center with the specified concentration cannot lead to the observed nonuniformity in the capacitance-voltage characteristics. Hence, the glass layer, but not the semiconductor substrate, defines the nonmonotonous behavior of the capacitance-voltage characteristics.

In our opinion, the nonmonotonous capacitance variation in the metal-insulator-semiconductor structure at inversion voltages is stipulated by the presence of a structure defect in the glass layer adjacent to the glass-semiconductor interface. The specified defect is an acceptor center by its nature. For sufficiently high inversion voltages, this center captures the holes from the formed inversion layer. The inversion layer charge lowers. This leads to the broadening of the semiconductor space charge layer and its capacitance; hence, the total capacitance of the structure decreases. The capture of holes by the acceptor center changes its charge state; this facilitates its ability to capture electrons at accumulation voltages.

The proposed model was confirmed by the temperature dependences of the tangent of the dielectric loss angle measured in the temperature range from  $-50$  to  $+10^\circ\text{C}$  (when an accumulation voltage of  $+5$  V was applied) for the structures that exhibited the nonmonotonous behavior in the C-V dependences and for the structures made using the same technology but without nonuniform behavior of the C-V dependences.

The comparison of the temperature dependences of the tangent of the dielectric loss angle showed that the dielectric losses had a pronounced relaxation maximum in all the structures. However, the relaxation maximum shifts in the direction of higher temperatures ( $-20^\circ\text{C}$  and  $+5^\circ\text{C}$  for both groups, respectively) and broadens in the structures with nonmonotonous C-V characteristics. This suggests an increase in the leakage losses in the glass owing to the recharge of the observed defect.

## REFERENCES

1. Litovchenko, V.G. and Gorban', A.P., *Osnovy fiziki mikroelektronnykh sistem metall-poluprovodnik* (Fundamentals of Physics of Microelectronic Systems Metal-Semiconductor), Kiev, 1978.
2. Winokur, P.S. and Boesch, Jr. Interface-State Generation in Radiation-Gard Oxides, *IEEE Trans. Nucl. Sci.*, 1980, vol. NS-27, no. 5, pp. 1647-1650.
3. Gergel', V.A. and Suris, R.A., Theory of Surface States and Conductance in Metal-Dielectric-Semiconductor Structures, *Zh. Eksp. Teor. Fiz.*, 1983, vol. 84, no. 2, pp. 719-736.
4. Nicollian, E.H. and Brews J.R., *MOS physics and technology*, New York: Wiley, 1982.
5. Vlasov, S.I., Ergasheva, M.A., Rakhimov, N., and Turgunov, Sh.T., Non-Monotonous Voltage-Capacitance Characteristics of Metal-Glass-Semiconductor Structures, in *Fundamental'nye i prikladnye voprosy fiziki. Trudy mezhdunarodnoi konferentsii* (Fundamental and Applied Problems of Physics, Proc. Int. Conf.), Tashkent, 2004, p. 379.
6. Parchinskii, P.B., Vlasov, S.I., and Turgunov, U.T., Properties of Passivating Coatings on the Basis of Lead-Borosilicate Glasses, *Neorg. Mater.*, 2002, vol. 38, no. 6, pp. 750-754.
7. Berman, L.S., Vlasov, S.I., and Morozov, V.F., Identification of Residual Deep Impurities in Semiconductor Devices by the Method of Capacitance Spectroscopy, *Izv. AN SSSR. Ser. Fiz.*, 1978, vol. 42, no. 6, pp. 1175-1178.
8. Berman, L.S. and Lebedev, A.A., *Emkostnaya spektroskopiya glubokikh tsentrov v poluprovodnikakh* (Capacitance Spectroscopy of Deep Centers in Semiconductors), Leningrad, 1981.